Effects of Oxide Incorporation in Proton Conducting Organic Electrolytes

Von der Fakultät Chemie der Universität Stuttgart
zur Erlangung der Würde eines Doktors der Naturwissenschaften (Dr. rer. nat.)
genehmigte Abhandlung

Vorgelegt von

Şeniz Sörgel (geb. Beyazyıldırım)

aus Izmir, Türkei

Hauptberichter:	Prof. Dr. J. Maier
Mitberichter:	Prof. Dr. E. Roduner
Tag der Einreichung:	20.05.2009
Tag der mündlichen Prüfung:	23.07.2009

Max-Planck-Institut für Festkörperforschung
Stuttgart
2009

CONTENTS

Zusammenfassung

In dieser Arbeit wurden die mit der Einlagerung von diversen oxidischen Partikeln (z. B. ZrO_2, TiO_2, Al_2O_3) in protonenleitfähige, organische Elektrolyte verbundenen Effekte untersucht. Einerseits wurde Imidazol als Modell für einen schwachen flüssigen Elektrolyten ausgewählt. Andererseits wurde eine für die Praxis sehr bedeutende, hoch protonenleitfähige Gruppe von perfluorierten aliphatischen Sulfonaten betrachtet, zu denen auch das bekannte Nafion zählt.

Im ersten Teil konnte erstmals gezeigt werden, das sich das Konzept des heterogenen Dopings auch auf einen schwach protonenleitfähigen Flüssigelektrolyten übertragen lässt. Imidazol ist ein protisches, amphoteres Lösemittel welches ähnlich wie Wasser ein Wasserstoffbrücken-Netzwerk ausbildet. Neben seinen zu Wasser ähnlichen Transportkoeffizienten zeigt Imidazol einen deutlich höheren Siedepunkt von 257 °C, wodurch es sich als flüssiger Protonenleiter vor allem bei hohen Temperaturen empfiehlt. Reines Imidazol weist aufgrund seiner niedrigen intrinsischen Ladungsträgerkonzentration nur eine moderate Protonenleitfähigkeit auf. Tatsächlich konnte eine signifikante Erhöhung der Protonenleitfähigkeit des Gesamtsystems durch die Beimischung von oxidischen Nanopartikeln erzielt werden. Die Charakterisierung der verschiedenen Composit-Materialien erfolgte mittels Impedanzspektroskopie, gepulster Feldgradienten-NMR-Spektroskopie (PFG-NMR) und Zetapotential-Messungen.

Die Impedanz-Spektrokopie wurde an Dispersionen verschiedener oxidischer Nanopartikel in Imidazol als Funktion der Temperatur und Partikelkonzentration durchgeführt. Die Ionenleitfähigkeit der Composite war dabei im Vergleich zu reinem Imidazol signifikant erhöht. Die höchste Ionenleitfähigkeit wurde für das Composit mit eingelagertem, erhitztem $sZrO_2$ erzielt, nämlich $1.66 \times 10^{-2}\ \Omega^{-1}\ cm^{-1}$ bei $\varphi = 0.25$ und T = 90 °C, was einer Erhöhung um einen Faktor von ~10 verglichen mit reinem ImiH bei der gleichen Temperatur entspricht. Zum Vergleich ist die Leitfähigkeit des ImiH-TiO_2-Composits um den Faktor 4.2 (bei $\varphi = 0.07$) und die Leitfähigkeit des ImiH-Al_2O_3-Composits um den Faktor 3.0 ($\varphi = 0.03$) verglichen mit reinem ImiH erhöht. Die erzielbaren Leitfähigkeiten zeigen dabei sowohl eine Abhängigkeit vom Volumenanteil des jeweiligen Oxids als auch von der Aktivität und der Dichte der sauren Gruppen auf der Partikeloberfläche. Als

typische Perkolationscharakteristik zeigen diese Systeme zunächst eine Leitfähigkeitserhöhung mit zunehmendem Volumenanteil des Oxids (φ), welche bei weiterer Erhöhung des Oxidanteils durch ein Maximum läuft (dies entspricht dem als Perkolationsgrenze bezeichneten Oxidanteil, bei dem sich ein attraktives, vollständiges Netzwerk ausgebildet hat, welches sich über das gesamte Compositmaterial erstreckt) und danach wieder abnimmt. Die Compositmaterialien mit Oxidpartikeln, deren Oberflächen die höchste Aktivität und Dichte von Säuregruppen aufweisen, zeigen auch die ausgeprägteste Leitfähigkeitserhöhung. Die Ergebnisse der PFG-NMR-Spektroskopie sind mit den Leitfähigkeitsmessungen konsistent. Die Ergebnisse wurden quantitativ im Rahmen des Konzepts des heterogenen Dopings verarbeitet, welches bereits erfolgreich genutzt wurde, um den Leitungsmechanismus in schwachen Festelektrolyten, salzhaltigen Polymerelektrolyten und salzhaltigen nichtwässrigen Flüssigkeiten zu beschreiben. Die Protonenleitfähigkeiten, welche durch Anwendung des Konzepts des heterogenen Dopings berechnet wurden, sind im Einklang mit den gemessenen Leitfähigkeiten. Das Konzept geht davon aus, dass die im Elektrolyten dispergierten, feinen Oxidpartikel zu einer Wechselwirkung führen, bei der eine Ionenspezies des autoprotolysierten Lösemittels auf der Oxidoberfläche spezifisch adsorbiert wird. Daraus resultiert eine erhöhte Konzentration an entsprechenden Gegenionen in der Raumladungsschicht an der Grenzfläche zwischen Oxid und Ionenleiter. Die Ergebnisse aus den Zeta-Potential-Messungen zeigen, dass die Oberflächenladungen der Oxidpartikel durch die Zugabe von Imidazol sehr stark zunehmen. Dies geht mit der Ausbildung einer Raumladungsschicht auf der Oxidpartikeloberfläche konform, welche aus der beschriebenen Ionenadsorption resultiert. In den beschriebenen Imidazolsystemen ist dies die spezifische Adsorption von Imidazolat-Anionen (Imi^-) auf der Oxidoberfläche, was zu einer erhöhten Konzentration an Imidazolium-Kationen ($ImiH_2^+$) in der Raumladungsschicht der Grenzfläche zwischen Oxid und Ionenleiter führt.

Der zweite Teil dieser Arbeit beschäftigt sich mit der Untersuchung der Auswirkungen auf die Protonenleitfähigkeit, die Mikrostruktur und die mechanischen Eigenschaften, die eine Beimischung von nanopartikulären Oxiden zu starken Polymerelektrolyten wie Nafion bewirkt. Nafion trägt stark saure Sulfonsäuregruppen und weist im voll hydratisierten Zustand eine hohe Protonenleitfähigkeit auf. Daher ist es bis heute weit verbreitet und wird

unter anderem als Membranmaterial in Polymerelektrolytmembran- und Direkt-Methanol-Brennstoffzellen (PEMFCs bzw. DMFCs) eingesetzt. Bei hohen Temperaturen verliert Nafion jedoch aufgrund der Dehydratation der Membran sehr schnell seine vorteilhafte Ionenleitfähigkeit, was die Arbeitstemperatur der entsprechenden Brennstoffzelle auf maximal T = 90 °C begrenzt. Ein neuer Weg zur Verbesserung der Membraneigenschaften führt über die Verwendung von Compositmembranen aus klassisch verwendetem Polymer, in das definierte Mengen an oxidischen Nanopartikeln homogen eindispergiert sind. Kürzlich wurden Nafion/Oxid-Composite entsprechend untersucht und es wurden einige Mutmaßungen über die Gründe der beobachteten, verbesserten Membraneigenschaften angestellt. Allerdings werden diese Annahmen nicht widerspruchsfrei von den bislang durchgeführten Experimenten unterstützt. Daher ist die Zielsetzung des zweiten Teils dieser Arbeit, die Gründe für die verbesserten Eigenschaften der Compositmembranen im Vergleich zu herkömmlichen, einphasigen Membranen bei hohen Arbeitstemperaturen und geringer Membranbefeuchtung umfassend aufzuklären. Es wurden daher verschiedene zweiphasige Compositmaterialien mit den verschiedenen zugrunde liegenden, einphasigen Polymermaterialien verglichen, wobei solche Systeme ausgewählt wurden, für die in der Literatur bereits verbesserte Eigenschaften durch Eindispergierung von Oxidpartikeln beschrieben sind. Zu Vergleichszwecken wurde auch kommerzielles, extrudiertes Nafion 117 entsprechend charakterisiert. Die Membranen wurden verschiedenen thermischen und hydrothermischen Behandlungen unterzogen, um deren Eigenschaften unter gewünschten bzw. nicht vermeidbaren, realen Arbeitsbedingungen von Brennstoffzellen zu untersuchen (i. d. R. hohe Temperaturen und geringe Feuchtigkeit). Als Untersuchungsmethoden kamen die Impedanzspektroskopie, die Dynamisch-Mechanische-Analyse (DMA), die Kleinwinkelröntgendiffraktometrie (SAXS), die Festkörper-NMR-Spektroskopie und die Abgeschwächte Totalreflexion (ATR) Infrarot-Spektroskopie zum Einsatz.

Die ATR-IR Ergebnisse zeigen, dass eine hydrothermale Behandlung der Membran bei einer hohen Temperatur und einer geringen Feuchtigkeit (z. B. T = 120 °C, 10% LF, t = 7 d) zu einer Kondensationsreaktion führt, wobei hier postuliert wird, dass sich dabei ein Sulfonsäureanhydrid der Form R-O_2S-O-SO_2-R bildet. Die gleichen Effekte sind nach einer thermischen Behandlung bei T > T_g (140 °C, 4h im Vakuum-Oven) zu beobachten. Außerdem deuten die Ergebnisse aus der Pulverdiffraktometrie und der energiedispersiven

Mikroanalyse darauf hin, dass es hierbei auch zur Bildung von elementarem Schwefel kommt. Die Kondensationsreaktion und Schwefelbildung führen zu einem erhöhten Äquivalentgewicht (Verringerung der Ladungsträgerkonzentration) und einer lokalen Ausordnung von Polymerkristalliten, was durch Säure-Base-Titration bzw. SAXS-Messungen belegt wurde. Die Leitfähigkeit der Membranen verringert sich durch die Temperatur- bzw. hydrothermale Behandlung. Bei hohen Wassergehalten lässt sich die Verringerung der Leitfähigkeit durch das zunehmende Äquivalentgewicht erklären. Durch die sich mit dem Wassergehalt ändernde Aktivierungsenergie ist jedoch die Leitfähigkeit bei geringem Wassergehalt und niedrigen Temperaturen deutlicher verringert, was sich nicht alleine durch eine verringerte Ladungsträgerkonzentration erklären lässt. Als weitere Ursache wurde eine ebenfalls verringerte Ladungsträgermobilität gefunden. Die geringere Mobilität bei geringem Wassergehalt kann auf die unter diesen Bedingungen für die Protonenleitfähigkeit weniger günstige Mikrostruktur der Membran zurückgeführt werden. Die vorgeschlagene Kondensationsreaktion und Schwefelbildung führt zu einer verringerten Hydrophilie der Polymerseitenketten. Dies hat eine negative Auswirkung auf die Morphologie des entsprechenden Composits (Phasenseparation), da die Hydratation der ionischen Cluster abnimmt. Dadurch verringert sich auch der Wassergehalt der Membran. Die DMA-Messungen belegen, dass ein verringerter Wassergehalt der Membran deren mechanischen Eigenschaften bei hohen Temperaturen verschlechtert, da Wasser unter diesen Bedingungen die Steifigkeit der Membran verbessert.

Die oben aufgeführten Effekte von thermischen und hydrothermalen Behandlungen auf Membraneigenschaften (Äquivalentgewicht, Wassergehalt und -volumenanteil) wie die Protonenleitfähigkeit, die Aktivierungsenthalpie, die Mobilität und die Mikrostruktur sind ohne die Anwesenheit von Oxidpartikeln schwerwiegender als bei den Compositmembranen. Die Ergebnisse der Impedanzspektroskopie, der Säure-Base-Titration und der SAXS-Messungen legen nahe, dass eine Kondensationsreaktion und/oder Alterungsprozesse und die damit verbundenen Änderungen der Transporteigenschaften durch die Anwesenheit von Oxidpartikeln unterdrückt werden. Aus DMA-Messungen folgt, dass die Compositmembranen einen höheren Wassergehalt unter verschärften Bedingungen behalten und dass sie mechanisch leicht stabiler sind als die entsprechenden einphasigen Membranen. Die Eindispergierung von Oxidpartikeln erhöht auch die

Glasübergangstemperatur um ca. 10 °C, was auf eine leicht erhöhte, thermische Stabilität der Composite hindeutet. Diese Ergebnisse belegen dass die Dispergierung von Oxidpartikeln in Nafion-Membranen deren Stabilität erhöht, was die damit verbundene, bessere Brennstoffzellenperformance bei hohen Temperaturen und niedrigen Wassergehalten erklärt.

Zusammengefasst wurde in dieser Arbeit gezeigt, dass die Einlagerung von Oxidpartikeln sowohl in schwachen als auch starken protonenleitfähigen Elektrolyten zu positiven Effekten führt: in Ersteren wird die Protonenleitfähigkeit durch eine Erhöhung der Ladungsträgerkonzentration in der Raumladungsschicht verbessert, in Letzteren wird die strukturelle, thermische und mechanische Stabilität des Materials auch unter verschärften Bedingungen gewährleistet. Diese Untersuchungsergebnisse können als Anregungen für mögliche Weiterentwicklungen von Elektrolytmaterialien in alternativen Energieumwandlern dienen.

1 Introduction

Due to the industrialization and growing population in the last centuries, fossil fuels which have been used as the major source of energy, have been consumed to a greater extent than ever. The high energy consumption has given rise to greenhouse effect resulting in global warming which has started threatening life on Earth. For these reasons, alternative sources of energy and energy conversion devices have become a key issue for technology development during the last decades. Nowadays one tries to avoid the step of converting chemical energy into heat energy (the process of heat engines) by directly converting chemical energy into electrical energy. This allows one to overcome the fundamental efficiency limitations of heat engines, set by thermodynamics. Devices such as batteries and fuel cells, which directly convert chemical energy to electrical energy, are considered to be possible solutions of a future problem of energy conversion. One of the critical parts of such devices is the separator material, the electrolyte, that conducts ions but is electronically insulating. To minimize dissipation of electrical energy into heat energy by the so called IR drop inside the electrolyte, its conductivity must be maximized and kept on a stable level.

There are two main ways of improving ionic conductivity: (i) search for new structures and compounds or (ii) enhance the conductivity of a given material by homogeneous or heterogeneous doping. Homogeneous doping involves incorporation of small amounts of an appropriate dopant into a host material in order to increase the charge carrier concentration therein. Whereas in the case of heterogeneous doping, addition of a second phase plays a decisive role for the conductivity of the system. While in the case of homogeneous doping, the local electrical neutrality is preserved, for heterogeneous doping deviations from local electroneutrality are essential[1].

Heterogeneous doping has been first used to improve the ionic conductivity of weak solid electrolytes. The history of the solids exhibiting ionic conductivity, namely of solid electrolytes, begins with the reported experiments on Ag_2S by Michael Faraday in 1833[2]. Until the late 1960s, very few devices based on ion-conducting materials were available, mainly due to the fact that these solids (e.g., alkali halides, silver halides) were poor conductors (10^{-7}-10^{-12} S cm^{-1}). Although it has been discovered by Jander in 1929[3] that

the conductivity of a two phase mixture can exceed the conductivities of the pure constituents, it took over 50 years for this phenomenon to receive the adequate attention. The pioneering work of Liang et al. in 1973[4] can be counted as the starting point of a new research area in the field of electrolytes for rechargeable lithium ion batteries, namely heterogeneous (or composite) electrolytes. Two-phase composite electrolyte systems were prepared by dispersing submicrometre-sized particles of insulating and chemically inert materials (called second phase dispersoids) into a moderate-ionic conducting solid (called first phase host-matrix). In Liang's work, it is reported that LiI doped with Al_2O_3 exhibits a conductivity about three orders of magnitude higher than that of the undoped LiI[4]. After this remarkable result, conductivity enhancements for other heterogeneous systems (two phase mixtures of weak solid electrolytes, mainly Li-, Cu- and Ag- halides with insulating oxides, such as Al_2O_3, SiO_2 or TiO_2) were also reported [1, 5-8].

In 1972 C. Wagner used the space charge concept to explain conductivity effects in two phase mixtures[9]. After Jow and J. B. Wagner's[5] attempts to explain the conductivity enhancement in ionic conductor systems by a semiquantitative space charge model, Maier developed the *heterogeneous doping concept* which explains the effect completely and quantitatively[1, 10-18]. According to the concept, internal adsorption of an ion type (e.g., Ag^+ in $AgCl:Al_2O_3$ or F^- in $PbF_2:SiO_2$) on the insulator surfaces, leads to high concentrations of compensating defects (here silver or fluoride ion vacancies) in the space-charge region formed at the insulator/conductor interface.

Later, similar ionic conductivity enhancement effects have been observed for solid polymer electrolytes (SPEs)[19-24]. An example of a solid polymer electrolyte is a solution of a lithium salt in a polyethylene oxide (PEO) matrix. PEO-LiX (X= ClO_4^-, BF_4^-, PF_6^- etc.) based solid polymer electrolytes (SPEs) have received great attention due to their potential capability to replace traditional liquid electrolytes of rechargeable lithium ion batteries[25]. Easy preparation, favorable mechanical properties, sufficient electrochemical stability and safety (as compared to liquid electrolytes) are the promising advantages of SPEs. General concepts of Li^+ transport in PEO based polymer electrolytes are coupled with the local relaxation and segmental motion of PEO chains, of which the conditions can only be obtained when PEO is in its amorphous state[19]. Since PEO tends to crystallize below 60 °C, its room-temperature ionic conductivity is quite low ($<10^{-7}$ S cm^{-1}). Much

work has been done to produce SPEs with a higher degree of amorphicity and accordingly higher overall ionic conductivity. Weston and Steele[26], in their pioneering research, for the first time demonstrated the idea of incorporating electrochemically inert ceramic filler particles of α-alumina into PEO. After this work, there have been many studies which show enhancements in the room temperature conductivity of conventional solid polymeric electrolytes (SPEs) as a result of dispersion of ceramic filler particles. Addition of micro/nanoscale (e.g., TiO_2, SiO_2) particles to polymer electrolytes to form hybrid nanocomposites was observed to result in an increased conductivity[19, 23], a slight increase in Li transference number, improved electrode-electrolyte interfacial stability and an increase in mechanical strength. It is observed that the size and the surface groups of the filler particles play a crucial role in the conductivity increase[21, 23, 27, 28]. There have been many proposals intended to explain the increase of conductivity in these systems such as: decreased crystallization temperature of the polymers thereby favoring the amorphous structure[20, 29], mobility changes owing to segmental motion of the polymers[30] and Lewis acid-base type interactions at the interface between polymer and particles. Some recent papers invoke ion adsorption as a possible mechanism as it leads to a breaking up of the ion pairs[31-34].

In order to investigate for a salt containing electrolyte the adsorption effect on the oxide surface in a detailed manner, the polymer has been replaced with a non-aqueous liquid solvent such as methanol (MeOH), tetrahydrofuran (THF) or dimethyl sulfoxide (DMSO)[35, 36]. Composites consisting of liquid non-aqueous salt solutions and solid insulating phases (e.g., $LiClO_4$ in MeOH:oxide) were observed to show enhanced ionic conductivities compared to the non-aqueous salt solutions. This new class of electrolytes was named “soggy sand” electrolytes[35-37]. Unlike classic solid-liquid[38, 39] composites, here the conductivity enhancement is synergistic in nature. That is, the overall conductivity is higher than in both of the constituent phases. Conductivity enhancement in these systems can be explained in a similar way as it is done for the weak electrolyte systems. The low ion-pair dissociation of such electrolytes is improved by anion adsorption at the oxide surface, which in turn leads to an enhancement of the Li^+ concentration in the space charge region near the oxide surface.

Oxides have also been incorporated into polymer electrolytes with intrinsic ionic properties, namely ionomers[40-57]. Ionomers are polymers which have a small mole fraction of ionic groups covalently bonded to the polymer backbone as pendant moieties. Perfluorosulfonated ionomer (PFSI) membranes (e.g., Nafion®) have been commonly used as electrolytes in polymer electrolyte membrane fuel cells (PEMFCs) and direct methanol fuel cells (DMFCs) because of their excellent proton conductivity (0.1 S cm^{-1}at 25 °C) under fully hydrated conditions[58-60]. However, at elevated temperatures PFSI membranes quickly loose their desirable ionic conductivity[61-63], thus limiting the fuel cell application to approximately T = 90 °C. Operating the PEMFCs and DMFCs at higher temperatures (T > 100 °C) and reduced humidities avoids most of the shortcomings associated with the low temperature fuel cell operation like CO poisoning of the electrode catalysts, slow electrode kinetics of the oxygen reduction reaction and expensive water/thermal management. It has been reported that oxide incorporation can extend the operation temperature of PEMFCs and DMFCs[40-42, 44-48, 52, 53, 56, 57, 64]. Even though a significant effect of oxides on the fuel cell performance at elevated temperatures has been observed, limited attention has been paid to an in-depth analysis of the reasons of this performance improvement. A better understanding of the effects of oxides is essential since it could suggest new routes for enhancing the fuel cell performance.

This thesis is divided into two parts. The aim of the first part is to investigate the effect of inorganic oxide admixture on the ionic conductivity of pure weak liquid electrolytes, specifically of moderately proton conducting liquid imidazole ($C_3H_4N_2$; abbreviated as ImiH). Imidazole exhibits moderate proton conductivity due to low intrinsic charge carrier concentration (low degree of self-dissociation: $ImiH + ImiH \rightleftharpoons ImiH_2^+ + Imi^-$)[65, 66]. Therefore, a perceptible conductivity increase by heterogeneously doping imidazole is expected. For this purpose, the proton conductivity of composites comprising dispersions of various types of nanometer sized oxide particles in pure imidazole is investigated, and the results are quantitatively analyzed according to the concept of heterogeneous doping. Contrary to the above mentioned example of non-aqueous liquid systems where solvent and salt exist as distinct entity, and in contrast to the effect on the defect formation in coulombic systems, in this work the focus is on the application of heterogeneous doping to a weak liquid electrolyte which shows intrinsic dissociation.

The motivation of the second part of this work is to investigate the effects of inorganic oxide admixture on proton conductivity, microstructure and mechanical properties of strong polymer electrolytes, especially of the Nafion® membrane. Nafion® is strongly acidic with its values of Hammett acidity function (H_0) ranging from -11 to -13. The ionic sulfonic acid groups are covalently bonded to the polymer backbone. It has excellent proton conductivity under fully hydrated conditions. Therefore, contrary to the imidazole system in the previous part, a conductivity increase due to the charge carrier concentration increase in the space charge layer is not expected. On the other hand, microstructure and accordingly mobility changes are anticipated with oxide incorporation. In addition, mechanical properties of the composites are expected to be improved, compared to the respective bare materials. Thermal and hydrothermal treatments are applied to the membranes in order to have an insight into the properties of the materials at high temperature and low humidity conditions. In this way, it is intended to understand the reasons for the better fuel cell performance of the composite membranes at high temperature/low humidity fuel cell operation conditions.

2 Imidazole/Oxide Composites

2.1 Introduction

Imidazole (ImiH) is a planar, five-membered heterocycle with nitrogen atoms in the positions one (N1) and three (N3) (Figure 2.1a). The N1 nitrogen is saturated and referred to as the pyrrole nitrogen, whereas the N3 nitrogen is unsaturated and referred to as the pyridine nitrogen. Imidazole behaves as a base in aqueous solutions and forms protonated imidazolium cations $(ImiH_2)^+$ ($pK_a = 7.0$) (see Figure 2.1b), with N3 being protonated. The acidity of the hydrogen atom bonded to the N1 nitrogen is weak ($pK_a = 14.4$). Deprotonation occurs only in strongly basic solutions, with the imidazolate anion $(Imi)^-$ being formed (Figure 2.1c)[67-69].

Due to its amphoteric character (potential proton donor and acceptor function), the formation of intermolecular hydrogen bonds, and the ability of undergoing self dissociation (approximately 0.1 %) liquid imidazole can be counted as a proton solvent[65]. Imidazole forms hydrogen-bond networks similar to water and the transport coefficients (i.e., mobility of protonic charge carriers and molecular diffusion coefficients) of liquid imidazole are similar to those of water[70, 71].

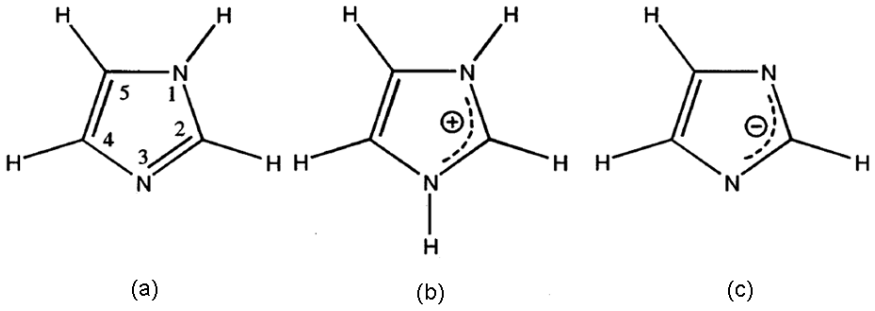

Figure 2.1: Structures of (a) neutral, (b) protonated and (c) deprotonated forms of imidazole.

The comparison of proton conductivity and diffusion data has already been shown to provide insight into the proton transport mechanism of neat liquid imidazole[65]. With a degree of self-dissociation of $\alpha = 0.1$ %, the diffusion coefficient D_σ as obtained from the measured conductivity σ turned out to be about four times higher than the molecular

diffusion $D(H_{CH})$ obtained by ^{1}H PFG-NMR spectroscopy. In other words, the mobility of protonic defects (imidazolium $ImiH_2^+$ and imidazolate Imi^-) is higher than the molecular mobility, which is a clear indication for a fast inter-molecular proton transfer. The overall picture involves proton transfer between protonic defects and neutral imidazole molecules connected with hydrogen bond breaking and forming reactions (structure diffusion)[71]. This process is comparable to the Grotthuss mechanism known for water [72, 73] and much more complex than a simple jump of an excess proton from one imidazole to another[74]. It also comprises reorientation of adjacent heterocycles and reorganization of the hydrogen bond coordination sphere of the migrating proton. Such a mechanism has been confirmed experimentally[66, 75, 76] and theoretically (Figure 2.2)[71].

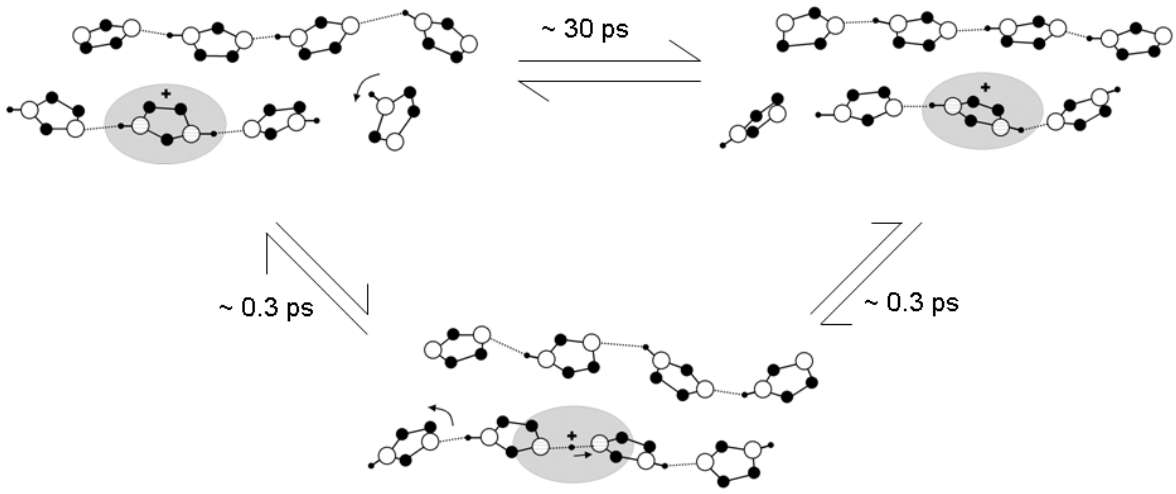

Figure 2.2: Proton conduction mechanism in liquid imidazole, as revealed by a Car-Parrinello molecular dynamics (CPMD) simulation[71].

Imidazole and polymers derived from imidazole or similar heterocycles have attracted attention recently as proton-conducting materials with potential applications as membrane materials in PEMFCs[66, 77, 78]. Its high boiling point (257 °C) makes it a good candidate to replace water as proton carrier in intermediate temperature PEMFCs[75, 79]. It has already been shown by Kreuer et al. that the liquid water phase can be replaced by imidazole or pyrazole in sulfonated polyetherketone membranes, which results in high protonic conductivity at high temperatures (T >100 °C)[65, 79]. The conductivity of a recast Nafion

membrane with ~10 wt % imidazole at 160-180 °C was found to be ~0.1 S/cm, as high as that of Nafion at 80 °C and 100% humidity[80]. Notwithstanding the excellent proton conductivity of the recast Nafion-imidazole membrane, it was discarded for fuel cell applications because imidazole poisons the Pt electrode[81].

The low intrinsic charge carrier concentration due to low self-dissociation, leads to moderate conductivities (about 10^{-3} S cm^{-1} at 90 °C). The conductivity of imidazole increases by doping with small amounts of acid[65]. In this way, mobile excess protons are introduced into the system ("extrinsic charge carriers"). The acid serves as a proton source for the hydrogen bond network formed by the imidazole molecules in such systems.

However, up to now, the effects of heterogeneous doping on the conductivity of imidazole and the applicability of the heterogeneous doping concept for a pure weak liquid electrolyte has not been investigated. Closing this gap is the aim of this work.

According to the heterogeneous doping concept, dispersion of fine oxide particles in an electrolyte leads to an interaction which results in trapping of one ion species on the oxide surface resulting in an increased concentration of the compensating ions in the space charge region at the interface of oxide and conductor. In such cases ion pairs are efficiently broken. The reason is not the variation of the dissociation constant within the electrolyte but the deviation from electroneutrality. The driving force for trapping can be the presence of a second phase with chemical affinity to the mobile ion. The ionic conductivity of the composite gradually increases with increasing amount of insulating phase, reaches a maximum where a steady-state percolation occurs and subsequently decreases at higher volume fractions. The percolation threshold depends on the matrix and dopant chemistry, particle size and processing parameters.

2.2 General Part

2.2.1 Heterogeneous Doping Concept

Here the heterogeneous doping concept will be discussed on the basis of the ionic conductor/insulator interface. The respective model has been represented in detail in literature[10, 14]. Frenkel disorder is one of the basic disorder types which involves cations leaving their regular positions and occupying interstitial sites, on account of the favorable

configurational entropy, and thus leaving behind vacancies. Assuming an ionic solid (M^+X^-) with Frenkel disorder, the bulk defect equilibrium can be written as following:

$$M_M + V_i \leftrightarrow M_i^{\cdot} + V_M' \tag{2.1}$$

where M_M represents a cation in a regular position, V_i a regular interstitial site, $M_i^{\cdot}$ an occupied interstitial cation and V_M' a cation vacancy. $M_i^{\cdot}$ and V_M' are typical mobile ionic centers. In the case of the number of electronic defects (electrons e' and holes $h^{\cdot}$) and of impurity ions is negligible, the bulk concentrations of ionic defects must be equal and fixed by mass action constant (K_F, F indicates Frenkel reaction) on account of the necessity for local electrical neutrality. If $[M_i^{\cdot}]$ and $[V_M']$ be the concentrations of the building elements interstitial ion ($M_i^{\cdot}$-V_i) and ion vacancy ($M_i^{\cdot}$-M_M), respectively, the mass action law takes the following form:

$$[M_i^{\cdot}] = [V_M'] = K_F^{1/2} = \exp -\frac{\Delta_F G^{\circ}}{2RT} = \exp \frac{\Delta_F S_m^{\circ}}{2R} \exp -\frac{\Delta_F H_m^{\circ}}{2RT} \tag{2.2}$$

where $\Delta_F G^{\circ}$ is the standard free enthalpy, $\Delta_F S_m^{\circ}$ the standard formation entropy and $\Delta_F H_m^{\circ}$ the standard formation enthalpy of the reaction 2.1.

In order to have a qualitative insight into what happens to boundary layers, a “free surface” is considered and the Frenkel reaction (2.1) is split:

$$M_M + V_S \leftrightarrow M_S^{\cdot} + V_M' \tag{2.3a}$$

$$M_S^{\cdot} + V_i \leftrightarrow M_i^{\cdot} + V_S \tag{2.3b}$$

First, a regular cation (M_M) is transported to the “free” surface (or interface) (V_S), trapped at an interface site ($M_S^{\cdot}$) whereby a vacancy is formed (V_M'). In the second step, the surface cation is transported into the interstitial position ($M_i^{\cdot}$).

Due to the local electroneutrality, the concentrations of the defects are identical in bulk ($x \to \infty$), but near the surface, the profile diverges (Figure 2.3a). However, this free surface

effect is far too weak to explain high conductivity effects observed experimentally. If a second phase is present which is able to influence the chemical potential of the cation directly at the interface, then the effect can be large. The second phase (A) can exert a stabilizing effect (I, Figure 2.3b) which results in drawing cations out of the space charge regions and creating vacancies in space charge regions. The other possibility is a destabilizing effect (II, Figure 2.3b) of the second phase, whereby cations are driven into interstitial positions. In the case of a contacted surface reaction Equations 2.3a and 2.3b can be replaced by:

$$M_M + V_A \leftrightarrow M_A^{\cdot} + V_M' \tag{2.4a}$$

$$M_A^{\cdot} + V_i \leftrightarrow M_i^{\cdot} + V_A \tag{2.4b}$$

It is sufficient to consider 2.4a since the Equation 2.4b is redundant on account of the validity of the reaction 2.1.

An analogue can be constructed for the anions. In the case of a local equilibrium, it is sufficient to formulate just one interaction reaction with the neighbor phase with keeping in mind the validity of the equilibrium 2.1.

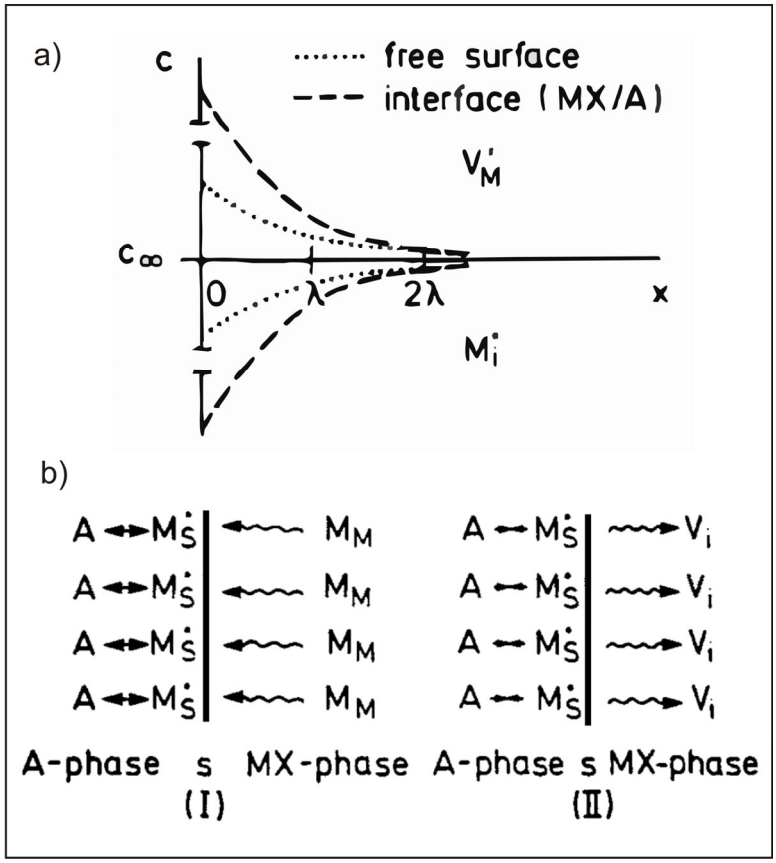

Figure 2.3: (a) Defect density profile of an ionic compound MX near an interface with gas phase (free surface or an insulating oxide (A) with high cation affinity; (b) Disorder effects of a cation stabilizing (I) and of a destabilizing (II) contact.[15, 17]

Considering an electrochemical reaction of the form $A(x) \rightleftharpoons A'(x')$ of a charged (z_j) particle j transferred from x to x′, if A≡A′ there is pure transport and for the case of x = x′ there is chemical reaction. At equilibrium, the electrochemical potential of the defects ($\tilde{\mu}$) is constant across an interface, but the chemical potential (μ) changes. The local electrochemical potential $\tilde{\mu}(x)$ can be broken into chemical and electrochemical terms as follows:

$$\tilde{\mu}(x) = \mu_j(x) + z_j F\phi(x) \tag{2.5}$$

where $\phi(x)$ is the local electrical potential, z_j the charge of defect type *j* and *F* Faraday's constant. The variable x represents the distance from the interface (x = 0 designated that

first layer adjacent to the interface). The local chemical potential is related to the molar concentration of defect j by the following equation:

$$\mu_j(x) = \mu_j^{\circ} + RT \ln c_j(x) \tag{2.6}$$

The concentration term stems from the configurational entropy, while the standard chemical potential (μ_j°) term contains all of the concentration-independent energy and entropy parameters such as partial enthalpies of formation, partial vibrational entropy of the defects etc. μ_j° is independent of x as long as the structure does not change. The equilibrium condition is:

$$d\tilde{\mu}(x) = 0 = d(z_j F\phi(x) + RT \ln c_j(x)) \tag{2.7}$$

So that the defect concentration profile in space charge region can be expressed as:

$$\zeta_j^{1/z_j}(x) = \exp\left[-\frac{F}{RT}\left(\phi(x) - \phi_{\infty}\right)\right] \tag{2.8}$$

ζ_j is short for $c_j / c_{j\infty}$ ($c_{j\infty}$ represents bulk concentration) which does not depend on the type of defect (z_j has been brought to the left hand side, in order to show that the expression is independent of j).

The local concentration in the space charge region (c_j) depends on the difference between the bulk and the local electrical potential ϕ_{∞} and $\phi(x)$. For $\phi(x) > \phi_{\infty}$, the concentrations of all negative (singly charged) defects are raised by the exponential factor $\exp\left[-\frac{F}{RT}\Delta\phi\right]$, while those of the positive (singly charged) defects are reduced by the same factor and vice versa for $\phi(x) < \phi_{\infty}$. The typical $\Delta\phi$ values are of the order of a few 100 mV.

In order to calculate the concentration distribution, a relation between concentration and electric field is necessary. For this, Poisson's equation ($\nabla^2\phi = -\rho / \varepsilon\varepsilon_0$, ρ denotes the charge density ($\sum_j z_j F c_j$) and $\varepsilon\varepsilon_0$ the absolute dielectric permeability) which is valid in

the absence of time-dependent magnetic fields should be combined with Equation 2.8. As a result Poisson-Boltzmann differential equation is obtained:

$$\frac{d^2(\phi-\phi_\infty)}{dx^2} = -\frac{F}{\varepsilon\varepsilon_0}\sum_j c_{j\infty} z_j \exp\left[-\frac{z_j F}{RT}(\phi-\phi_\infty)\right] \tag{2.9}$$

Considering two mobile, equivalently but oppositely charged defects ($z_+ = |z_-| = z$), in the case of electrochemical equilibrium, differential equation for the concentration enhancement is obtained as follows:

Since $\zeta_+ = \zeta_-^{-1}$ $$\frac{d^2 \ln \zeta_\pm}{d\xi^2} = \frac{1}{2}(\zeta_\pm - \zeta_\mp) = \frac{1}{2}\left(\zeta_\pm - \zeta_\pm^{-1}\right) \tag{2.10}$$

where ξ is the local variable normalized to the Debye length ($\xi = x/\lambda$).

$$\lambda = \sqrt{\frac{\varepsilon\varepsilon_0 RT}{2z^2F^2c_\infty}} \tag{2.11}$$

The above differential equation can be integrated using boundary conditions $\zeta_\pm(x=0) = \zeta_{\pm 0}$ and $\zeta_\pm(x\to\infty) \equiv \zeta_{\pm\infty} = 1$ meaning that a bulk profile forms in the ionic conductor far away from the interface. If the concentration of the depleted charge carrier is ignored in the charge density, this results in an error in the total charge density less than 6%[14] and the Equation 2.10 simplifies to:

$$\frac{d^2 \ln \zeta_1}{d\xi^2} = \frac{\zeta_1}{2} \tag{2.12}$$

The solution for ζ_1 (the subscript 1 applies to the enriched positive or negative defect) follows as:

$$\zeta_1 = \frac{\zeta_{10}}{\left(1+\sqrt{\zeta_{10}}\,\xi/2\right)^2} \tag{2.13}$$

where $\zeta_{10} \equiv \zeta_1(x=0)$.

When $\xi = 2$, i.e. x = 2λ, the parameter ζ_1 falls to the bulk value 1 if $\sqrt{\zeta_{10}} \gg 1$ is assumed. Therefore, the double Debye length (2λ) is a convenient measure of the extent of space charge zone.

If we do not ignore the depleted effect as we did above, the Equation 2.10 can be integrated to get

$$\zeta_{\pm} = \left(\frac{1 + \vartheta_{\pm} \exp - \xi}{1 - \vartheta_{\pm} \exp - \xi} \right)^2 = \zeta_{\mp}^{-1} \tag{2.14}$$

$$\text{for } \vartheta_{\pm} = \frac{\zeta_{\pm 0}^{1/2} - 1}{\zeta_{\pm 0}^{1/2} + 1} = -\vartheta_{\mp} \tag{2.15}$$

The parameter ϑ defined by the degree of influence[10] depends on ζ_0 and hence on c_0. ϑ = 0 if the boundary layer defect chemistry does not differ from the bulk defect chemistry, i.e. zero charge, $\zeta_0 = 1$. It varies between 0 and +1 for an enrichment effect and between 0 and -1 for a depletion effect.

2.2.1.1 Conductivity Contribution of a Single Interface

If both defects are in spatial equilibrium, that is the Gouy-Chapman case with $|z_1| = |z_2| \equiv z$. The conductivity contribution of the defect under consideration parallel to the interface can be calculated analytically by integrating the conductivity profile from the interface (x = 0) to the bulk $x_{\max} = d \gg \lambda$ (a single interface (bicrystal) experiment as shown in Figure 2.4).

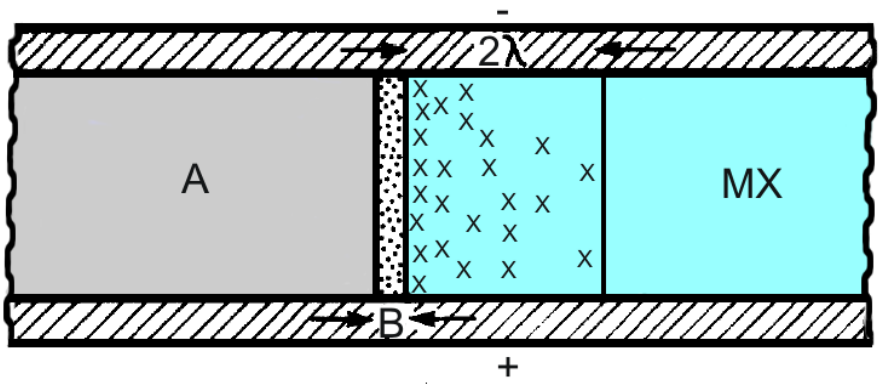

Figure 2.4: An experiment on a MX/A bicrystal. B is the thickness of the interaction layer, the geometry is infinite in one direction in MX.

$$Y_{1.2}^{\parallel} \equiv \int_0^d \sigma_{1,2}(x)dx = Y_{1,2\infty}^{\parallel} + \Delta Y_{1,2}^{\parallel} \tag{2.16}$$

With the bulk contribution $Y_{1,2\infty} = dzFu_{1,2}c_\infty$ and the space charge contribution

$$\Delta Y_{1,2}^{\parallel} \equiv \int_0^\infty \Delta\sigma_{1,2}(x)dx = (2\lambda)zFu_{1,2}\left[2c_\infty \frac{\vartheta_{1,2}}{1-\vartheta_{1,2}}\right] \tag{2.17}$$

The total excess parallel conductance $\Delta Y^{\parallel}$ is obtained as the sum $\Delta Y_1^{\parallel} + \Delta Y_2^{\parallel}$, not taking into account the cell dimensions perpendicular to the x direction. In the case of large effects and the example of an enrichment of defects 1 ($\vartheta \to 1$), $1-\vartheta_1$ approaches $2\zeta_{10}^{-1/2}$ and the Equation 2.17 becomes

$$\Delta Y_1^{\parallel} = (2\lambda)z_1Fu_1\sqrt{c_{10}c_\infty} = u_1\sqrt{2\varepsilon\varepsilon_0RTc_0} \tag{2.18}$$

The effective concentration is simply the geometric mean of bulk and interfacial concentrations. The influence of c_∞ cancels out ($\lambda \propto c_\infty^{-1/2}$), so that the conductivity increase is independent of the bulk concentration. Therefore, if the concentration at x = 0 is raised by four orders of magnitude with respect to the bulk value, the effective space charge conductivity increases by two orders of magnitude.

2.2.1.2 Conductivity of Two Phase Mixtures

The calculation of the conductivity of a two-phase mixture, for example an ionic conductor/insulator composite, requires simplifications of the distribution topology, since a complex superposition of various transport paths by bulk and interfaces exists. Maier assumed a three-dimensional network of percolating paths with simple cubic symmetry[1, 10, 14]. All components perpendicular to the current direction cancel out, while the remaining components with mean specific conductivity are connected in parallel and can be combined to an effective volume fraction $\varphi_\alpha \beta_\alpha$ (α indicates various zones), which contributes to the quasi-parallel circuit. The conductivity of the composite (σ_m) can be written as follows:

$$\sigma_m = \sum \sigma_\alpha \beta_\alpha \varphi_\alpha \tag{2.19}$$

Small oxide particles (A) can form continuous paths even at low volume fractions (φ_A). The volume fraction at which the first continuous path forms is called percolation threshold. The formation of continuous conduction paths is mainly due to the nature of the interfacial interactions. At high φ_A values agglomeration of particles and therefore blocking effects occur.

Neglecting the conductivity of the insulator phase and interface core, the following equation is obtained:

$$\sigma_m = (1-\varphi_A)\beta_\infty \sigma_\infty + \varphi_A \beta_L \sigma_L \tag{2.20}$$

The first term describes the conductivity attributed to the bulk (denoted by ∞) and the second term describes the conductivity contribution from the space charge zone (denoted by *L*). β_∞ and β_L measure the number of continuous paths and for many solid-solid composites they have been found not to depend on φ and temperature in the interesting φ range. Considering a primitive cubic morphology, a semiquantitive insight is obtained as $\beta_\infty = 1$ and $\beta_L = 1/3 ... 2/3$ [10]. In solid-liquid composites, one expects the percolation behavior to be complex and β_L to be a strong function of φ and *T*.

If we combine Equations 2.18 and 2.20, we obtain the equilibrium conductivity (neglecting blockage effects as high-conductivity paths are parallel to the bulk) as follows:

$$\sigma_m = (1-\varphi_A)\sigma_\infty + \varphi_A \beta_L \Omega_A (2\varepsilon\varepsilon_0 RT)^{1/2} u\,(c_0)^{1/2} \tag{2.21}$$

where φ_A is the volume fraction of oxide particles, σ_∞ is the conductivity in bulk, β_L accounts for the degree of percolation, Ω_A is the ratio of the surface to the volume of the insulating A phase ($\Omega_A = 3/r_A$ when the particles are spherical in shape with the radius r_A), ε is the permittivity of ionic conductor, R is the gas constant, T is the temperature, u is the mobility of charge carriers in the bulk and c_0 is the concentration of charge carriers in the first layer of the space charge zone adjacent to the adsorption layer. For the case of overlapping space charges, c_0 is to be diminished by the concentration in the middle of two adjacent interfaces[6].

With this formula it is possible to explain the increase in conductivity of two-phase mixtures in a quantitative manner. Equation 2.21 is in good agreement with the experiments in literature[6, 8, 10-17, 35-37, 82-85].

In the case of the integrated charge density (i.e. the surface charge (Σ) on the oxide) is experimentally available, Equation 2.21 can be simplified to:

$$\sigma_m = (1-\varphi_A)\sigma_\infty + \varphi_A \beta_L \Omega_A \Sigma\, u F \tag{2.22}$$

where F is Faraday's constant. This formulation does not depend on details of the charge distributions. The ion exchange capacity can be expressed by $\Sigma\Omega_A/\rho$ (ρ: density of oxide).

In order to elucidate the conduction mechanism, the temperature dependence of conductivity should be investigated. At high temperatures the conductivity is independent of doping since it is of interstitial type (intrinsic). Hence,

$$-R\frac{\partial \ln \sigma_m}{\partial 1/T} \cong \frac{\Delta_F H_m^\circ}{2} + \Delta_m H^{\neq} \cong \frac{\Delta_F H_m^\circ}{2} \tag{2.23}$$

where $\Delta H^{\neq}$ is the migration enthalpy of the enriched defect type and $\Delta_F H_m^{\circ}$ is the formation enthalpy that is necessary to create defects by charge transfer from the bulk to the interface. At low temperatures the total conductivity is dominated by vacancies (extrinsic).

$$-R\frac{\partial \ln \sigma_m}{\partial 1/T} \cong \Delta_m H^{\neq} \tag{2.24}$$

If the surface charge is adequately stabilized by the influence of the neighboring phase, $\Delta_F H_m^{\circ}$ can be neglected.

If the solid ground structure is replaced by a liquid one-as done in this work-, several points are similar but also deviations occur:

(1) The interstitial particle corresponds to the imidazolium cation and the vacancy to the imidazolate anion. The local behavior might be quite similar.

(2) The percolation is definitely more complex and the above equations for σ_m are expected to represent the situation less precisely. In particular β will be a strong function of φ and *T*.

(3) The networks are expected to be less durable and prone to coarsening and sedimentation.

2.2.2 Experimental Techniques

2.2.2.1 AC-Impedance Spectroscopy

Impedance spectroscopy is a very powerful electrochemical tool to characterize intrinsic electrical properties of materials and interfaces. The basis of impedance spectroscopy is the analysis of the impedance (resistance of alternating current) of the observed system in subject to the applied frequency ω, and exciting signal. If the system under investigation is linear, the current response to a sinusoidal potential will as well be a sinusoid at the same frequency but shifted in phase.

For ionically conducting solids, the impedance spectroscopy technique was first applied by Bauerle in 1969 to analyze doped ZrO_2[86]. The technique was successful to differentiate between bulk, grain boundary and electrode resistances. Since then the technique has been widely used to investigate a wide range of ionic conductors. Electrode reactions at the electrode/electrolyte interface (diffusion, adsorption/dissociation, charge transfer) and processes related with mass transport within the solid electrolyte grains and across grain boundaries have different relaxation times and can be separated by varying the frequency over several orders of magnitude. Microstructural fluctuations, compositional variations, segregation of impurities or secondary phases at the grain boundaries have influence on the transport of the charge carrying species through grains and across grain boundaries and thus on the response of the process in the frequency domain. The expression for impedance Z (ω) is composed of a real and an imaginary part:

$$Z(\omega) = Z' + iZ'' \tag{2.25}$$

$$Z' = \mathrm{Re}(Z) = |Z| \cos(\phi) \tag{2.26}$$

$$Z'' = \mathrm{Im}(Z) = |Z| \sin(\phi) \tag{2.27}$$

$$\phi = \tan^{-1}(Z''/Z') \tag{2.28}$$

If the real part is plotted on the x-axis and the negative imaginary part on the y-axis of a chart, a "Nyquist plot" is obtained. On the Nyquist plot the impedance can be represented as a vector of length, $|Z| = [(Z')^2 + (Z'')^2]^{1/2}$. The angle between this vector and the x-axis is called phase shift ϕ (phase difference between voltage and current). Nyquist plots have the shortcoming that the frequency is only an implicit parameter. Another popular presentation method is the "Bode plot". The impedance is plotted with log frequency on the x-axis and both the absolute value of the impedance (|Z|) and phase-shift on the y-axis. Unlike Nyquist plot, Bode plot explicitly gives frequency information.

2.2.2.2 Zeta Potential

If one of the three states of matter is finely dispersed in another then a colloidal system (aerosols, emulsions, gels, etc.) is formed. Particles in dispersion may adhere and form aggregates of increasing size which may settle down due to gravity. An initially formed

aggregate is called a floc and the whole process flocculation. If the aggregate changes to a much denser form, the process is called coagulation. Unlike coagulation flocculation can be reversed (by the process of deflocculation). In the 1940s the DLVO theory (named after Derjaguin, Landau, Verway, and Overbeek) was developed which deals with colloidal stability. According to the theory, the stability of colloids in suspension is determined by the sum of the electrostatic repulsive and van der Waals attractive forces which the particles experience as they approach one another. The total interaction energy as a function of particle separation displays a maximum, called energy barrier. The height of the barrier indicates how stable the system is. For agglomeration to occur, two colliding particles must have sufficient kinetic energy due to their velocity and mass to overcome this barrier.

Most particles in an aqueous colloidal dispersion carry an electric charge. There are many origins of this surface charge depending upon the nature of the particle and its surrounding medium. When a particle is immersed in a strongly polar solvent such as water, the interface will acquire a charge, by either adsorbing or desorbing ions according to the chemical equilibrium with the surrounding solution. Ions of opposite charge, the counter ions, are attracted and bound to the surface of the particle and form so called Stern layer. Additional counter ions are still attracted by the particle but now they are repelled by the Stern layer as well as the other counter-ions that are trying to approach the colloid particle. This dynamic equilibrium results in the formation of a diffuse layer of charge adjacent to the particle. The Stern layer plus the diffuse layer constitute the electrical double layer. The thickness of the double layer depends on the type and concentration of ions in solution. The range of the double layer repulsion can be modified by changing the ionic strength of the solution.

When an electric field is applied across an electrolyte, charged particles suspended in the electrolyte are attracted towards the electrode of opposite charge (electrophoresis). The particles move with a characteristic velocity which can be measured by using Laser Doppler Velocimetry (LDV, also known as laser Doppler anemometry, or LDA). LDV is based on the scattering of light from a moving particle, where the frequency of scattered light will be shifted by an amount dependent on the speed and direction of the movement.

The velocity of a colloidal particle (v) in an electric field (E) is commonly referred to as its electrophoretic mobility ($\mu = \frac{v}{E}$) which is dependent on the strength of the electric field, the dielectric constant and the viscosity of the medium and on the electrical potential at the boundary between the moving particle and the liquid. This boundary is called the slip plane (Figure 2.5). The charge or electrostatic potential at the slipping plane is defined as the zeta potential ζ (Figure 2.5). It corresponds to the potential drop across the mobile part of the electrical double layer. The electrophoretic mobility is related to the zeta potential by the Henry equation:

$$\zeta = \frac{4\pi\eta\mu}{\varepsilon} \cdot f_{\kappa a} \tag{2.29}$$

where ηis the viscosity, μ is the electrophoretic mobility, ε is the dielectric constant and $f_{\kappa a}$ is the correction factor for the electrophoretic deceleration which is the ratio of the particle radius to the thickness of the diffuse layer. The magnitude of the zeta potential gives an indication of the potential stability of the colloidal system. Particles with zeta potentials more positive than +30 mV and more negative than -30 mV are normally considered stable. For a certain pH, defined as the point of zero charge (pH_{pzc}) or iso-electric point (IEP), the surface charge is zero (neutral).

In aqueous media the surface of the oxide is generally represented as a plane covered with hydroxyl groups. The electrical charge localized at the surface is generally assumed to originate in the protonation/deprotonation of these groups according to the following reactions:

$$-M-OH + H^+ \leftrightarrow -M-OH_2^+$$

$$-M-OH + OH^- \leftrightarrow -M-O^- + H_2O$$

This mechanism can be described as an amphoteric dissociation of surface -OH groups. The relative fraction of the dissociated sites depends strongly on the pH of the solution and determines the polarity and the magnitude of the surface charge.

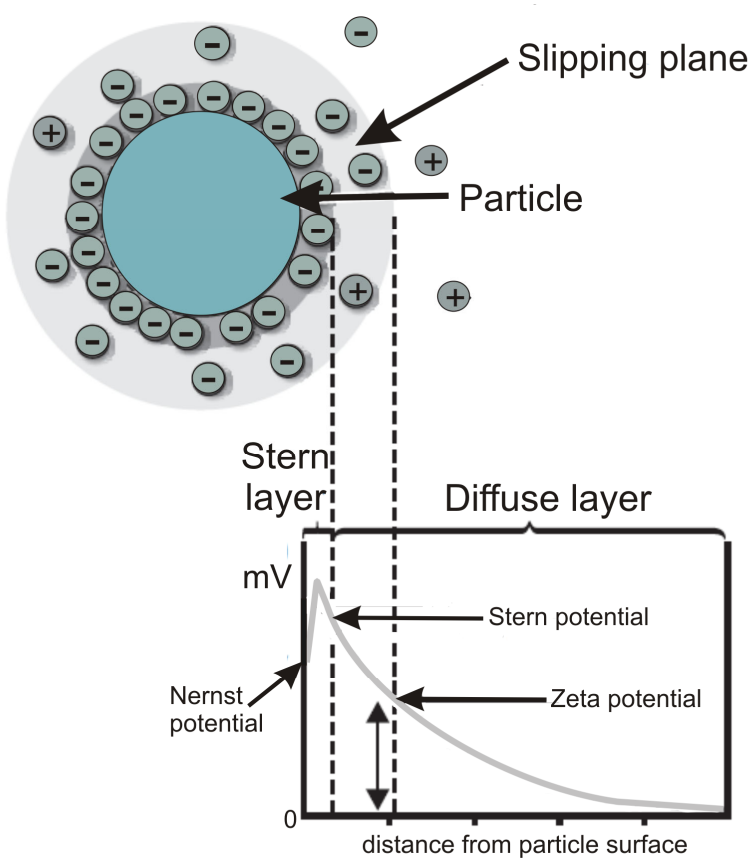

Figure 2.5: Schematic representation of double layer.

2.2.2.3 Pulsed-Field Gradient Nuclear Magnetic Resonance (PFG-NMR) Spectroscopy

PFG-NMR provides a convenient way for measuring translational motion of molecules selectively, without being affected by vibrational or rotational motions. The random translational motion of particles driven by internal kinetic energy is called self-diffusion[87]. PFG-NMR self-diffusion measurements are based on Hahn spin-echo pulse sequences with field gradient pulses of duration δ and magnitude G in each τ period which leads to the attenuation of the spin echo amplitude due to the magnetization of resonant nuclei. Applying magnetic field gradient pulses, the spin echo becomes sensitive to the translational motion of the molecules which carry the nuclear spin under study. The so-called "Stejskal and Tanner sequence" or "PFG sequence" is shown in Figure 2.6. Assuming that the net magnetization is oriented along the z-axis, a 90° r.f pulse rotates the

magnetization from the z-axis into the x-y plane. At the end of the first τ period, spin *i* experience a phase shift ϕ and a 180° r.f. pulse is applied in order to reverse the sign of the phase angle or of the applied gradients and static field. At time $t_1 + \Delta$, a second gradient pulse of equal magnitude and duration is applied which has the effect of changing the sign of the first gradient pulse. If the spins have not undergone any translational motion with respect to the z-axis, the effects of the two applied gradient pulses cancel and all spins refocus. However, if the spins have moved, the degree of dephasing due to the applied gradient is proportional to the displacement in the direction of the gradient (the *z*-direction) in the period Δ. Since this simple sequence is based on a Hahn spin-echo, the echo signal, *S*, is attenuated by both the effects of the spin-spin relaxation and of diffusion. When the magnetic field B_0 is homogeneous and the gradient pulses are well matched, the signal intensity is given by the following equation;

$$S(2\tau) = S(0)\underbrace{\exp(\frac{-2\tau}{T_2})}_{\substack{\text{attenuation due} \\ \text{to relaxation}}}\underbrace{\exp(-D\gamma^2G^2\delta^2(\Delta-\delta/3)}_{\substack{\text{attenuation due} \\ \text{to diffusion}}} \qquad (2.30)$$

$$S(2\tau) = S(2\tau)_{G=0}\exp(-D\gamma^2G^2\delta^2(\Delta-\delta/3)$$

where $S(0)$ is the signal immediately after the 90° pulse, 2τ is the total echo time, T_2 is the spin-spin relaxation time of the species, γ is the gyromagnetic ratio of the observe nucleus, G is the strength of the applied gradient, and δ and D are the duration of the gradient pulses and the separation between them, respectively. To remove the effects of the signal attenuation due to, in the case of the Stejskal and Tanner sequence, spin-spin relaxation, the signal is normalized with respect to the signal obtained in the absence of the applied gradient and thereby the echo attenuation is defined as:

$$E(2\tau) = \frac{S(2\tau)}{S(2\tau)_{G=0}} = \exp(-D\gamma^2G^2\delta^2(\Delta-\delta/3) \qquad (2.31)$$

In a PFG experiment, either G, δ, or Δ is varied while keeping τ constant. Then D is straightforwardly determined.

The integral property of the PFG NMR spectroscopy averages all inhomogeneities over time and space and therefore allows for the calculation of effective macroscopic properties such as conductivity.

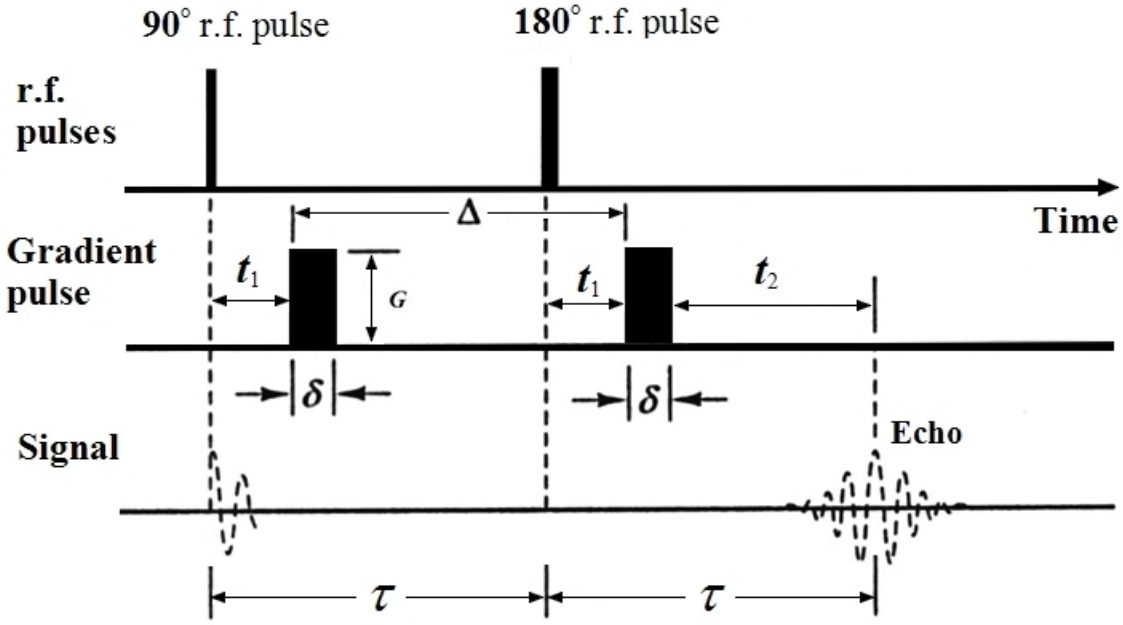

Figure 2.6: Simple scheme of a Stejkal-Tanner pulsed field gradient spin echo diffusion experiment[88].

2.3 Experimental

The chemicals that were used in this study are the following: Imidazole (ImiH, Merck, 99 % purity), titanium dioxide (TiO_2; Alfa Aesar, 99.9%), aluminum oxide (Al_2O_3; Sigma-Aldrich; MSU-X type), sulfated zirconium dioxide ($sZrO_2$; obtained from $sZrO_2$ precursor ($sZr(OH)_4$), Mel Company) and mesoporous titanium dioxide (mesoporous-TiO_2; prepared according to ref. [89], BET surface area: 131 m^2g^{-1}, pore size: 7.4 nm).

BET (Brunauer-Emmett-Teller) analysis was employed to determine the surface area, pore size and pore size distribution of oxides by nitrogen adsorption. A surface area analyzer (Autosorb-1, Quanta Chroma) was used. Prior to the measurements the powders were heated at 120 °C for 12 hours under nitrogen in order to remove the physisorbed water. The results are shown in Table 2.1.

The ion (cation) exchange capacity (IEC) measurements were performed in order determine the surface charge of the oxides. IEC values of the inorganic fillers were determined by performing potentiometric titrations. For that purpose, the oxide fillers were suspended in a 0.1 M aqueous NaCl solution and stirred continuously for 1 hour. A defined amount of a 0.01 M solution was added for each sample and the slurry then was back-titrated with a 0.01 M HCl solution.

The size of the oxide particles were determined via TEM (Philips CM30ST) operating at a voltage of 200 kV.

Composites were prepared by thoroughly mixing (in an agate pestle and mortar) appropriate amounts of imidazole with various as received and preheated oxides (at 300 ^{o}C for 12 hours under vacuum). The volume fraction (φ) of oxides in the ImiH-oxide composites was $\varphi = 0–0.5$.

The composite conductivities were measured in a custom built U-shaped cell with platinum electrodes, and temperature was controlled by immersing the cell in a oil containing thermostat (Lauda E200). Ionic conductivities of the composites were measured as a function of temperature T (range: 70–140 ^{o}C, step size: 10 °C, equilibration time for each temperature point: 30 min) using ac-impedance spectroscopy in the frequency range 10^2–10^6 Hz (Hewlett Packard 4284A). The cell constant was estimated by measuring the ionic conductivity of a standard 0.1 M aqueous KCl (σ = 12.8 mS/cm) solution and 0.01 M (σ = 1.41 mS/cm) at 25 ^{o}C.

ζ–potential measurements were performed according to the electrophoretic technique[90, 91] using a Zeta Master (Malvern Instruments). An aqueous 0.001 M KNO_3 solution, which is generally taken as an inert electrolyte for zeta potential experiments[92], was prepared and a small amount of oxide was added in order to measure the zeta potential of the oxides therein. Different amounts of ImiH were added into the solution to investigate the effect of ImiH on the zeta potential of the oxides. All of the samples were ultrasonicated for 10 min before the measurements in order to break the agglomerates.

^{1}H self-diffusion coefficients of the composites were measured using a home-built NMR spectrometer with a specially designed pulsed magnetic field gradient (PFG) equipment[93]

at a proton resonance frequency of 49.6 MHz in the temperature range between 90 °C and 120 °C. The applied magnetic field gradient strength was 4 T m^{-1} with a maximum pulse length of 1 ms and a maximum diffusion time of 20 ms.

2.4 Results and Discussion

2.4.1 Characterization of the Filler Particles

It is shown in literature for weak solid electrolytes, polymer-salt electrolytes and non-aqueous liquid-salt electrolytes that size, specific surface area and surface groups of the filler particles play a crucial role in the conductivity increase[14, 22, 27, 36]. Composites with acidic oxides having large surface areas are recorded to have much higher conductivities compared to the basic oxides with small surface areas. For this reason, various types of nano-sized (around 10 nm, see Figure 2.7) acidic oxide particles (pH of the dispersed oxides in water are 4.2, 4.7 and 5.1 respectively for $sZrO_2$, TiO_2 and Al_2O_3) have been used in this study. Ion exchange capacities in aqueous solutions (IECs) and surface areas of the as received and heated oxides are given in Table 2.1. Heat treatment is performed in order to eliminate the surface organic impurities and surface water of the oxides. In this way, possible effect of surface water adsorbed on the oxide particles on proton conductivity is eliminated. As shown in Figure 2.8, organic impurities are removed upon heat treatment. The stretching and bending vibrations of Al-O and Ti-O appear in the vicinity of 400-850 cm^{-1} as a broad band[94] (Figure 2.8 and 2.9). The broad band between 3000-3500 cm^{-1} is attributed to the OH stretching vibrations of adsorbed water and the OH stretching mode of the hydroxyl groups (mainly responsible for the band at around 3450 cm^{-1}). The band at 1640 cm^{-1} is assigned to the bending mode of water. The intensity of these bands decreases gradually upon heat treatment. The spectra thus give evidence for the dehydration and dehydroxylation of the sample during heat treatment. The elimination of most of the terminal OH groups upon heat treatment is also confirmed by the IEC measurements which show decay in IEC values (Table 2.1). The surface areas of TiO_2 and Al_2O_3 increase after calcination which might be due to the elimination of surface organic impurities and surface water. However, the surface area of $sZrO_2$ decreases upon heat treatment which corresponds to the densification of the structure accompanied by the loss of micro- and mesopores. The IEC of $sZrO_2$ increases after calcination due to surface

activation. The sharp band at 1380 cm^{-1} is attributed to the stretching vibrations of the S=O group of covalent sulfate groups[95-97]. The IR bands at 1200, 1135, 1055, and 900 cm^{-1} are characteristic bands of bidentate sulphate[98] (Figure 2.10). The broad band with a minimum at 3420 cm^{-1} is attributed to the acidic OH groups[99].

Table 2.1: IECs and BET surface areas of the oxides

	IEC [mmol g^{-1}]	BET surface area [m^2 g^{-1}]
As-received $sZrO_2$	1.39	432
Heated $sZrO_2$	1.91	183
As-received TiO_2	1.61	350
Heated TiO_2	0.89	430
As-received Al_2O_3	0.91	340
Heated Al_2O_3	0.17	370

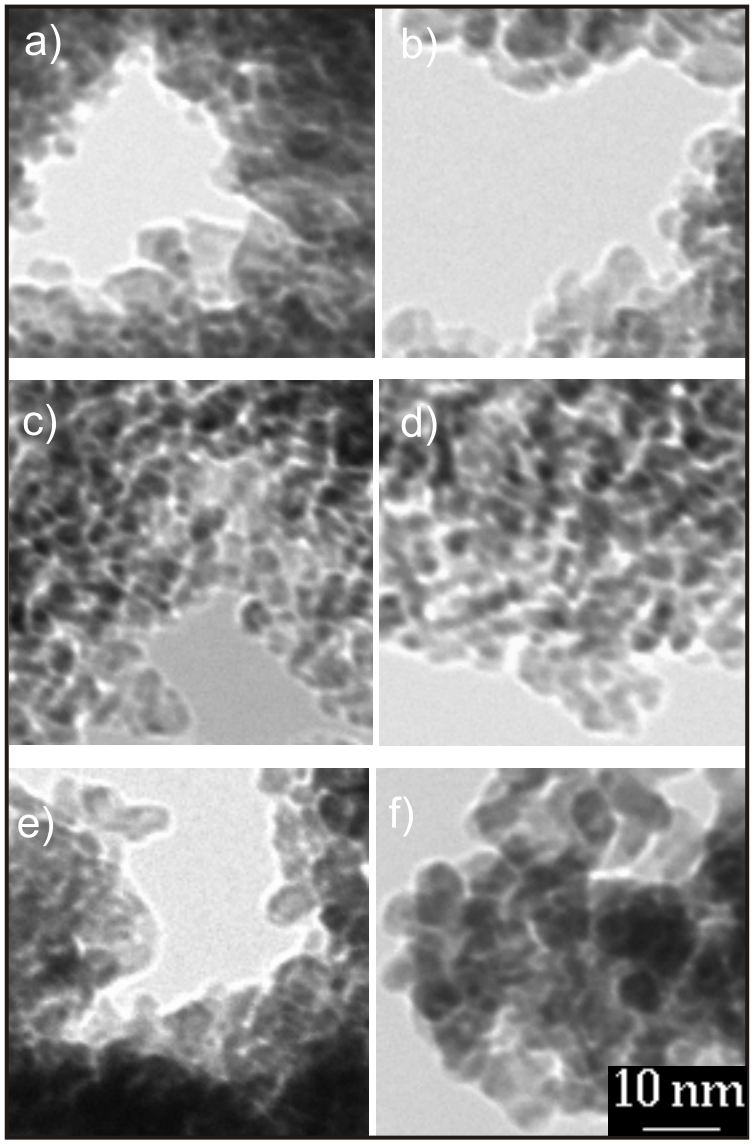

Figure 2.7: Transmission electron micrographs of various oxides: a) as-received TiO_2, b) heated TiO_2, c) as-received Al_2O_3, d) heated Al_2O_3, d) as-received $sZrO_2$ and e) heated $sZrO_2$. The scale is the same for all of the images.

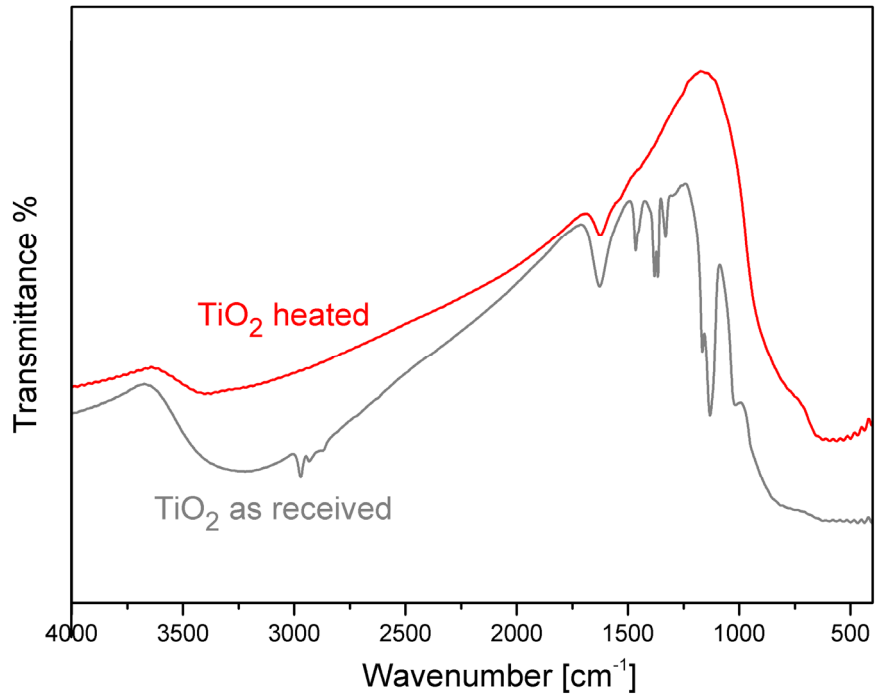

Figure 2.8: IR spectra of as received and heat-treated TiO_2.

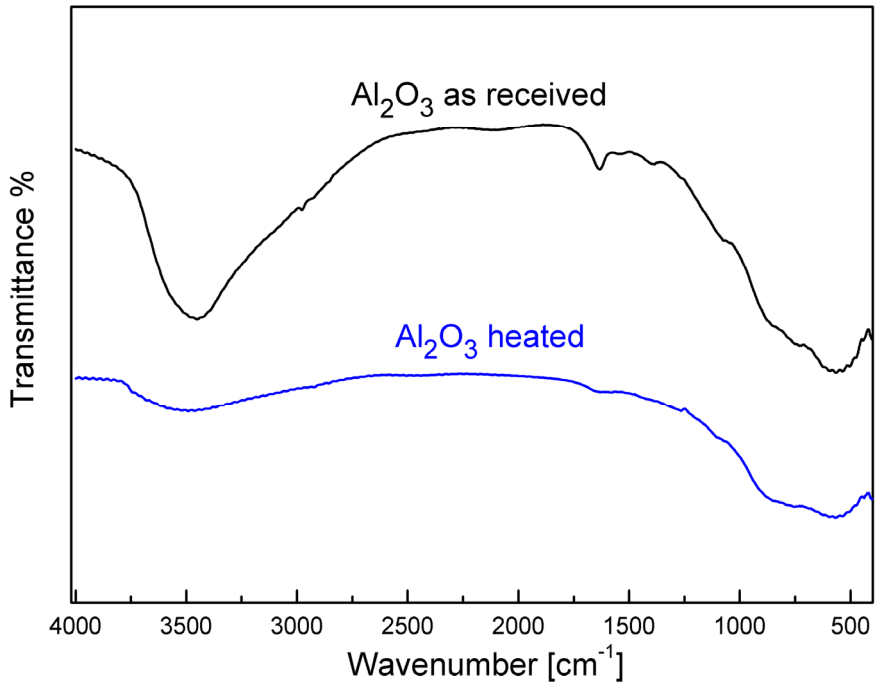

Figure 2.9: IR spectra of as received and heat-treated Al_2O_3.

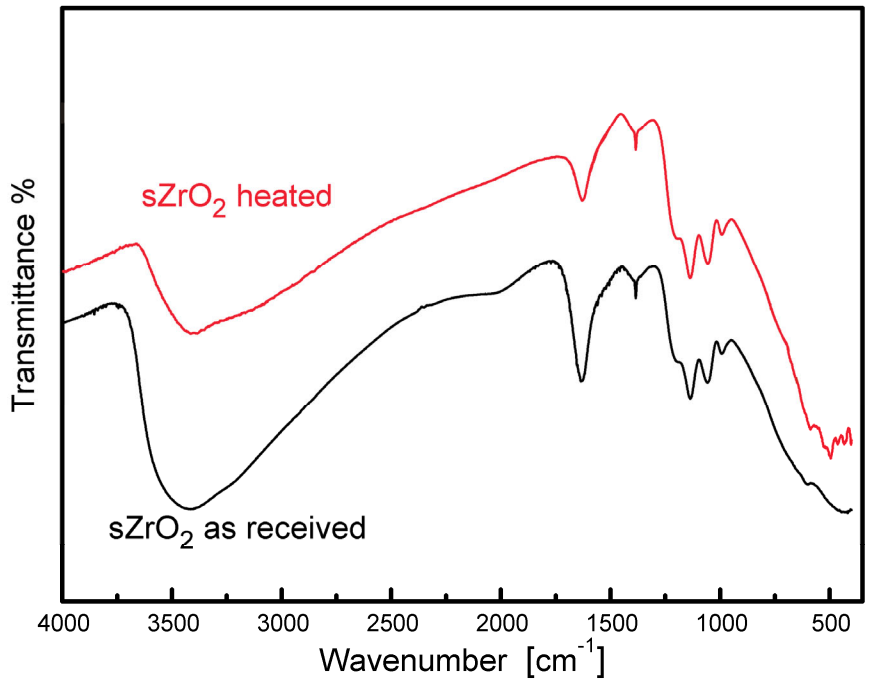

Figure 2.10: IR spectra of as received and heat-treated $sZrO_2$.

2.4.2 Ionic Conductivity

Dispersion of nanometer sized oxide particles in imidazole is observed to increase the ionic conductivity of pure imidazole. Figure 2.11 shows the overall effective conductivity enhancement as a function of oxide volume fraction of the composites obtained by dispersion of nanometer sized $sZrO_2$, TiO_2 and Al_2O_3 particles, respectively, in imidazole. The highest measured composite ionic conductivity is observed for the composite with heated $sZrO_2$, viz. 1.66×10^{-2} Ω^{-1} cm^{-1} at $\varphi = 0.25$ and 90 °C corresponding to an enhancement by a factor of ~10 compared to the pure ImiH at the same temperature. In comparison, the ImiH-TiO_2 composite conductivity is enhanced up to a factor of 4.2 (at $\varphi = 0.07$) and the ImiH-Al_2O_3 composite conductivity only up to a factor of 3.0 (at $\varphi = 0.03$) compared to the pure imidazole.

As a typical percolation characteristic in such systems, conductivity increases with increasing oxide volume fraction (φ), reaches a maximum (percolation threshold i.e. the volume fraction at which an attractive network is established through the composite) and then decreases with further increase in oxide concentration.

The effective conductivities depend on size and volume fraction of oxides as well as on activity and density of the acidic sites on the surface. The conductivity enhancement achieved by incorporating heat-treated TiO_2 and Al_2O_3 particles to imidazole is less compared to the enhancement achieved by using as received particles. This is probably due to the dehydroxylation of the surface of oxides (decrease of IEC values) as a possible impact of water on the ionic conductivity of pure imidazole and the composite is checked by directly adding water into the system with no significant effect being observed. Since the proton transport mechanism of liquid imidazole is quite similar to that of water[70, 71], this result is expected.

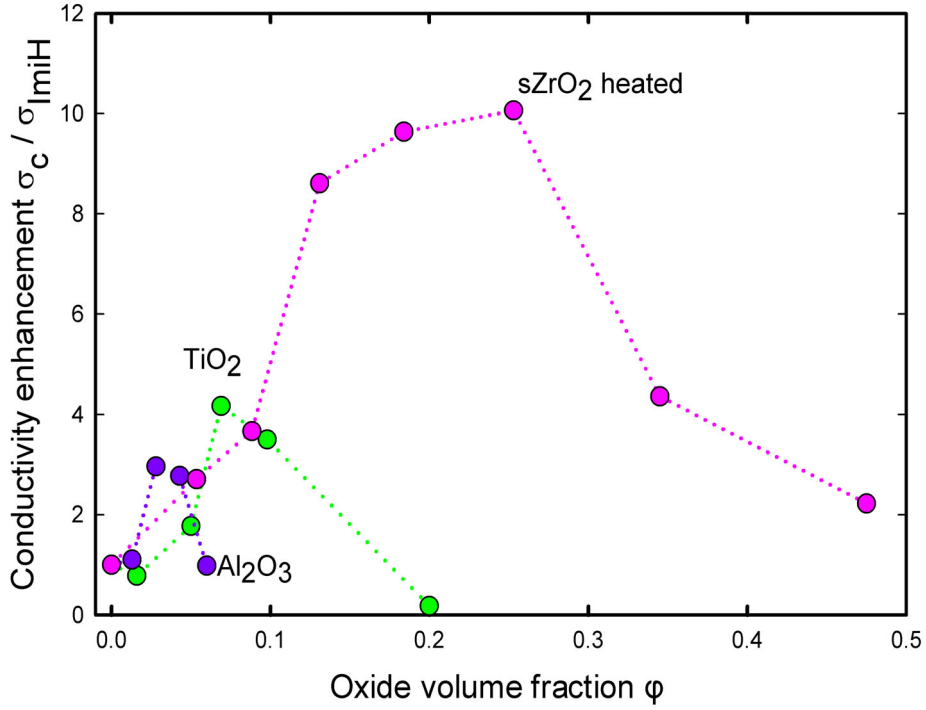

Figure 2.11: Plot of the effective overall conductivity enhancement as a function of oxide volume fraction at 90 °C. $\sigma_{ImiH} = 1.6.10^{-3}\ \Omega^{-1}\ cm^{-1}$ at 90 °C.

The model chosen to estimate the maximum ionic conductivity of such composites is a three-dimensional network of percolating paths and neglects blocking effects. The surface charge is compensated by a space charge layer of conducting species decaying from its maximum value c_0 to the bulk value c_∞. The ionic conductivity can be approximated by the

Equation 2.21. It is important to note that the composite conductivity is synergistic in nature and is highly dependent on the percolation of the space charge regions.

The ionic conductivity enhancement in the ImiH-oxide composites is attributed to the adsorptive interaction at the active oxide surface. Dispersion of fine oxide particles in imidazole leads to an interaction which results in trapping of imidazolate anion (Imi^-) on the oxide surface resulting in an increased concentration of imidazolium cation ($ImiH_2^+$) in the space charge region at the interface of oxide and conductor(Figure 2.12a). If under the bottom-line an excess of Imi^- is adsorbed, an enrichment of $ImiH_2^+$ in the space charge layer (compared to the bulk) adjacent to the oxide's surface is the consequence. Imi^- will be depleted there by the same factor (Figure 2.12b).

A seemingly alternative but conceptually not different possibility is the assumption that surface OH groups of the acidic oxides are dissociated and, the proton injected into ImiH; subsequent solvation again leads to the same products, viz.

$(S... Imi)^- + ImiH_2^+$ (S=OH, S being the surface group).

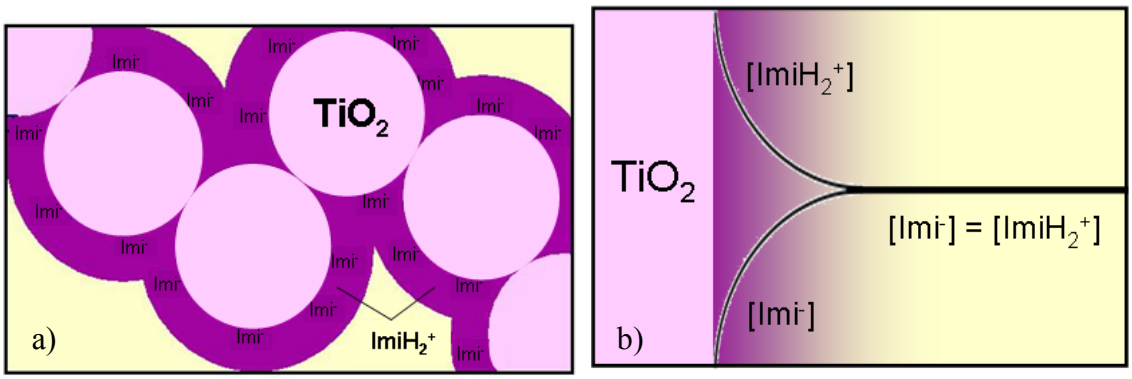

Figure 2.12: Schematic representation of the anion (Imi^-) adsorption on the TiO_2 surface.

Figure 2.13 shows the temperature dependence of the ionic conductivities of the pure imidazole and the composites with various TiO_2 concentrations. Composites prepared with the other oxides show the same kind of temperature dependency (Figures 2.14-2.18). The activation energy of pure imidazole is 0.23 eV. The parallelity in the temperature variation of the composites to that of pure ImiH suggests that the ion conduction mechanism is the

same in both cases. A more detailed analysis corroborates this. As the conductivity of the nominally pure ImiH is higher than for ultra-pure intrinsic ImiH, this obviously refers to an extrinsic situation (slightly doped by negative impurities). This is again consistent with the fact that the slope in the Arrhenius diagram is not far from the migration energy. By using the conductivity data of homogeneous doping of ImiH with sulfanilic acid[65], the migration energy term is estimated as 0.1 eV. In the case of heterogeneous doping, again the migration contribution is dominant as long as the $c_0^{1/2}$ term is T-independent. The remaining difference of ca. 0.1 eV can be well due to the T-dependence of c_0 in Equation 2.21 (or Σ in Equation 2.22), to a slight T-dependence of β_L but also due to the approximation of the rough model. One should also be aware of the high dopant concentrations (> 5%) in the determination of the above migration energy. If the ion exchange capacity value of TiO_2 in water is used to assess Σ in Equation 2.22, a good agreement with experimental results is achieved. The continuous lines shown in Figure 2.13 are the predictions using Equation 2.21 with a degree of percolation (β_L) of 0.2. In ref.[14] a β_L value of ~0.5 was assessed for ideal percolation. Realistic values should be smaller. The satisfactory description suggests that the ionic conductivity enhancement in the case of ImiH-TiO_2 can be well explained by the concept of heterogeneous doping. Transforming Σ-values in c_0-values, we arrive at $c_0 = 1.5\ 10^{-3}$ mol/cm^3 corresponding to a reasonable mole fraction of 0.03. Ionic conductivity data of the other oxides are also fitted by using Equation 2.21 (Figures 2.14-2-18). β_L values differ with different types of oxides (for Al_2O_3 β_L = 0.50 and for sZrO_2 β_L = 0.25) but do not significantly depend on temperature. It has to be noted that the lower value of β_L compared to the ideal percolation may not be solely due to percolation effects. As β_L acts as a fitting parameter it naturally absorbs all the short-comings of the first-order model.

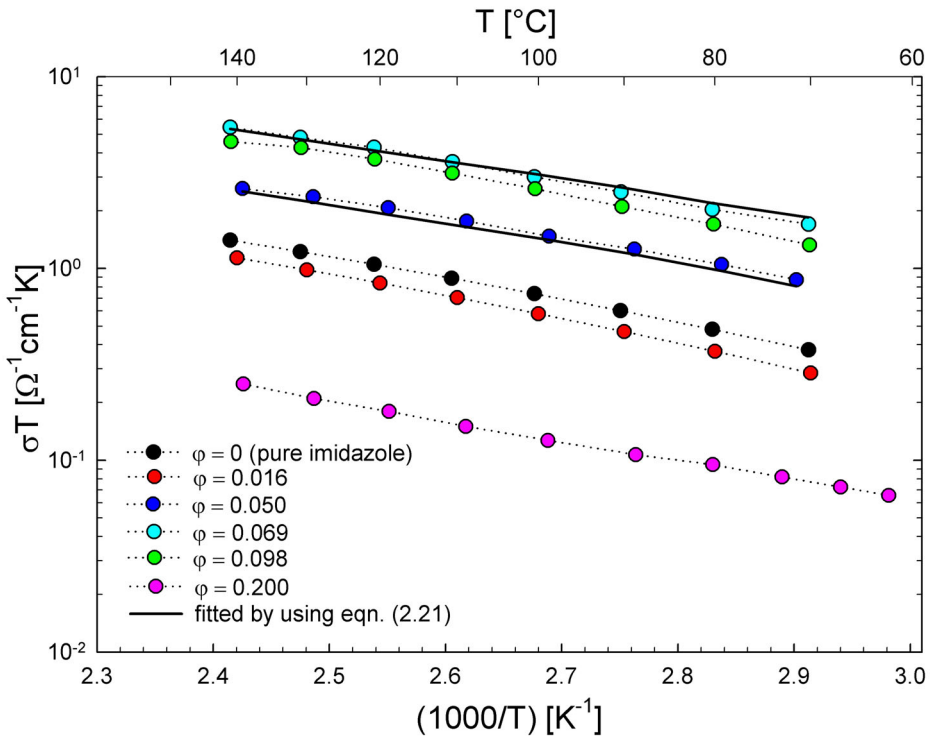

Figure 2.13: Ionic conductivity of ImiH–TiO_2 composites with various volume fractions (φ) of as-received TiO_2 as a function of temperature.

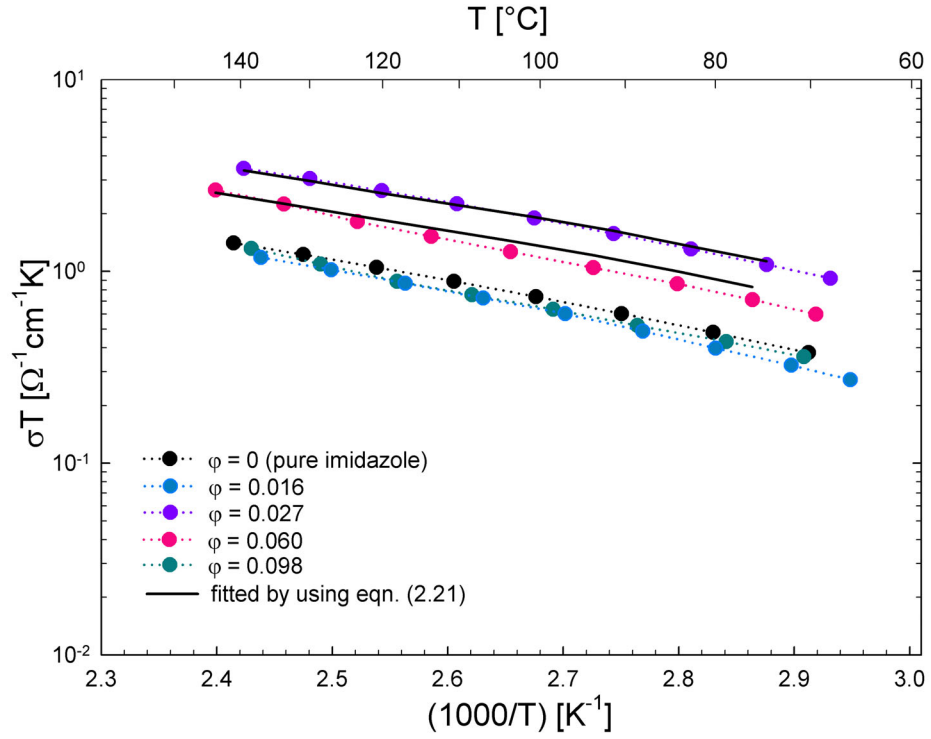

Figure 2.14: Ionic conductivity of ImiH–TiO_2 composites with various volume fractions (φ) of heat-treated TiO_2 as a function of temperature.

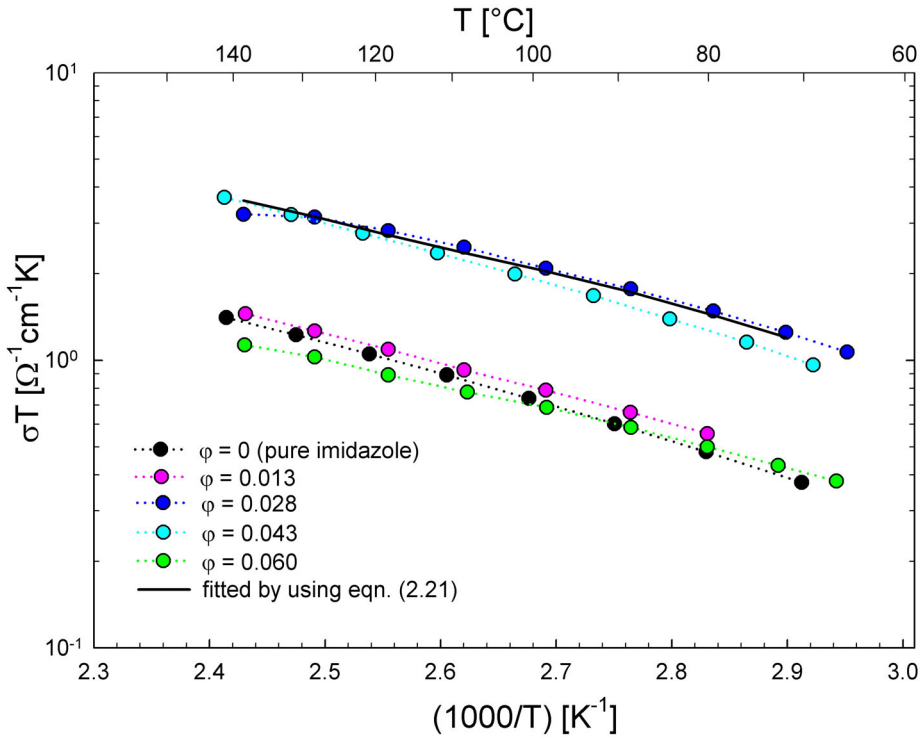

Figure 2.15: Ionic conductivity of ImiH–Al_2O_3 composites with various volume fractions (φ) of as-received Al_2O_3 as a function of temperature.

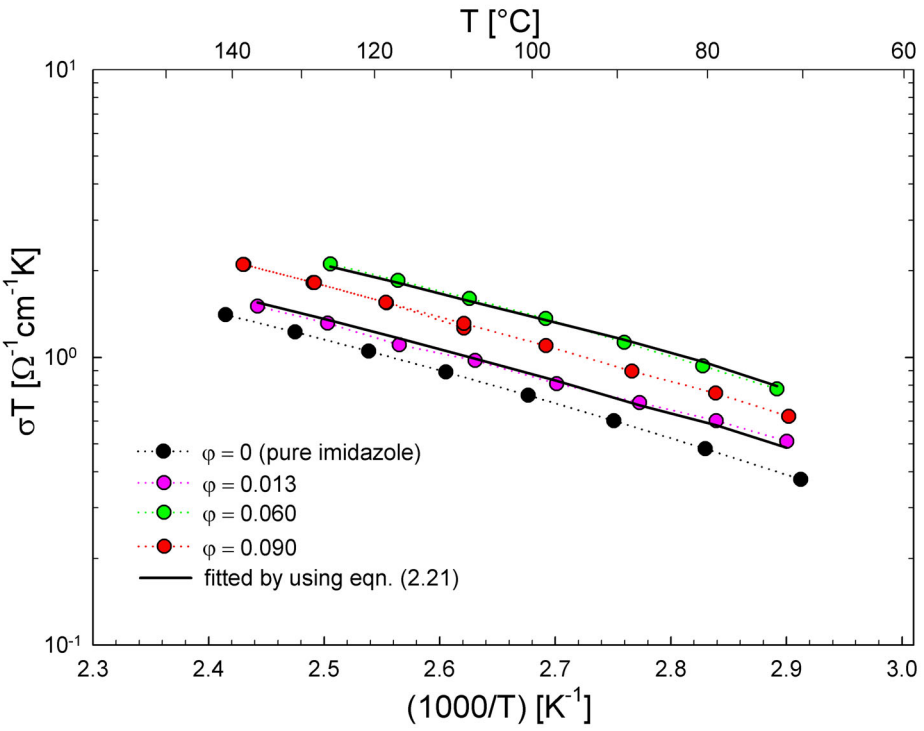

Figure 2.16: Ionic conductivity of ImiH–Al_2O_3 composites with various volume fractions (φ) of heat-treated Al_2O_3 as a function of temperature.

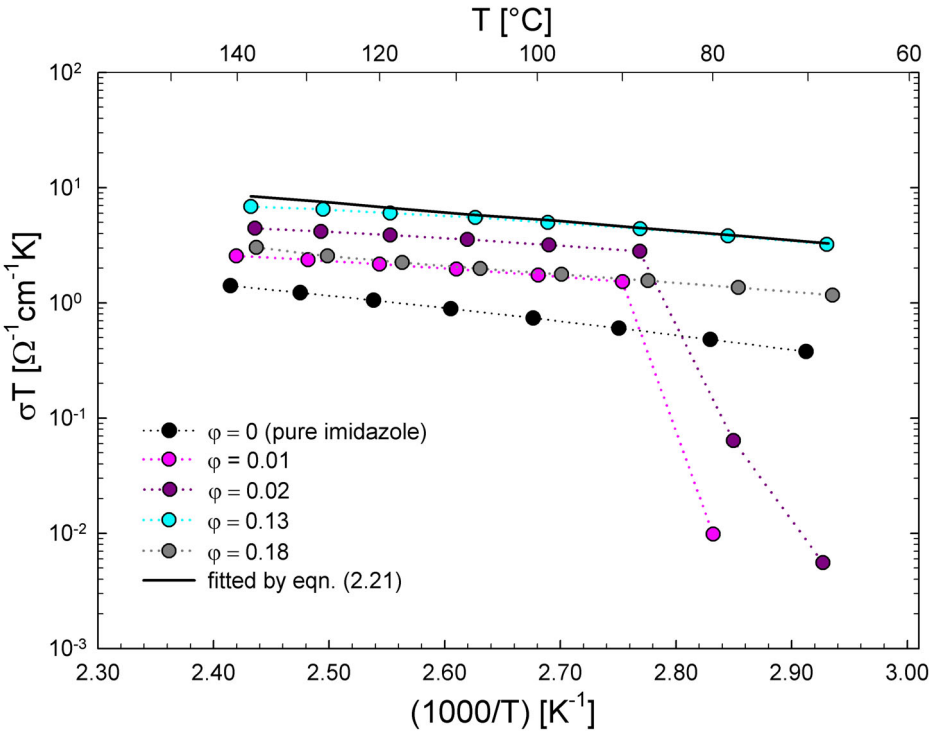

Figure 2.17: Ionic conductivity of ImiH–$sZrO_2$ composites with various volume fractions (φ) of as-received $sZrO_2$ as a function of temperature.

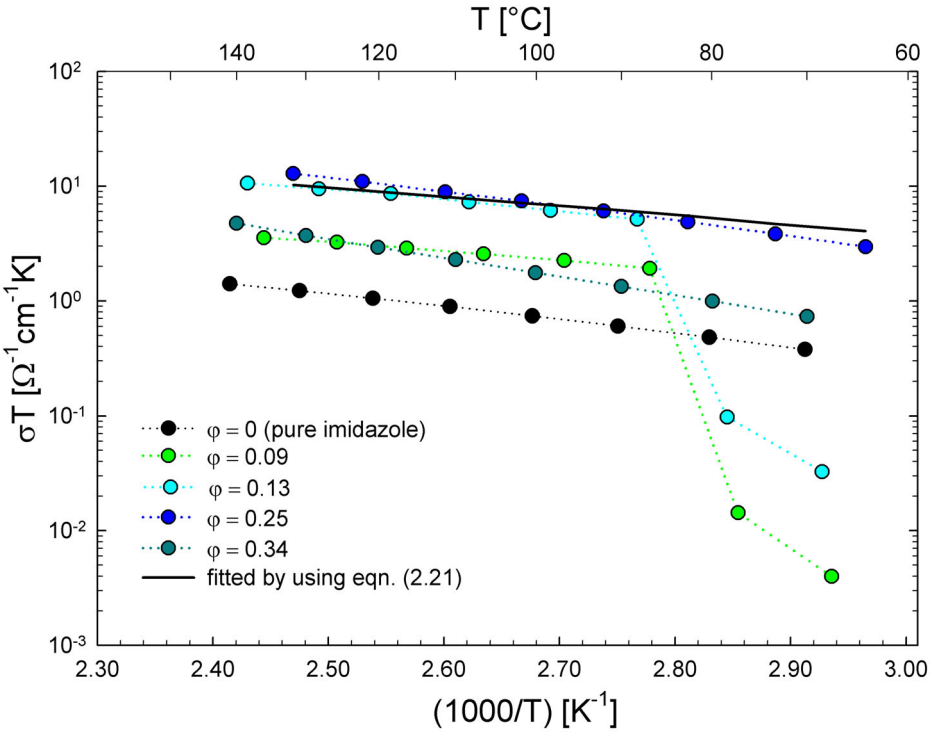

Figure 2.18: Ionic conductivity of ImiH–$sZrO_2$ composites with various volume fractions (φ) of heat-treated $sZrO_2$ as a function of temperature.

Mesoporous materials, owing to their high surface areas and nanometer sized pores have been used as a dispersant in weak electrolytes[85, 100, 101]. In such composites, much higher surface areas and volume fractions (compared to the solid nano-sized particles) can be achieved without losing percolation. Experiments performed on LiI-mesoporous Al_2O_3 composites with mesoporous alumina particles having similar surface areas but different pore sizes show that as the pore size decreases, maximum of the conductivity enhancement increases and shifts to low oxide volume fractions [100]. In the case the distance between two interfaces is comparable to the Debye length, conductivity enhancement due to "size effect" was predicted, as a result of an overlapping space charge regions[14].

Figure 2.19 shows the temperature dependence of the ionic conductivities of the pure imidazole and the composites with mesoporous TiO_2 and nanosized solid TiO_2. Conductivity enhancement is higher for ImiH-mesoporous TiO_2 at low volume fractions reflecting higher Ω values and probably also different percolation behavior.

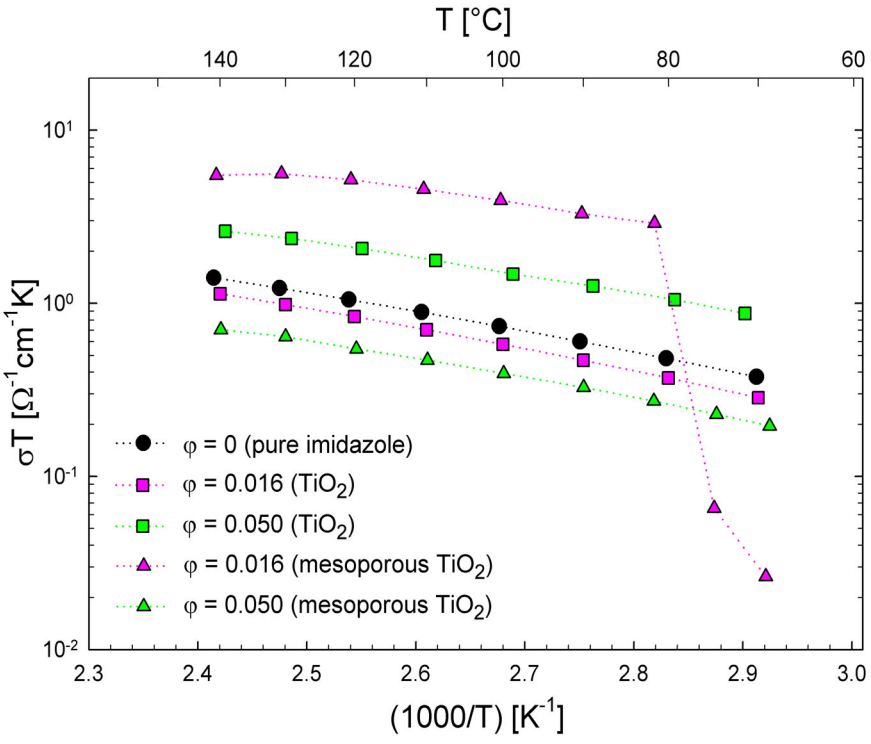

Figure 2.19: Ionic conductiviy of ImiH–mesoporous TiO_2 (triangle symbols) and ImiH–TiO_2 (square symbols) composites with various volume fractions (φ) versus temperature.

The comparison of the conductivity results of the composites with those resulting from homogeneous doping of ImiH with sulfanilic acid[65] shows that the highest heterogeneous doping effect does not reach the overall enhancements that are possible by homogeneous doping, but exceeds them locally by far (Figure 2.20).

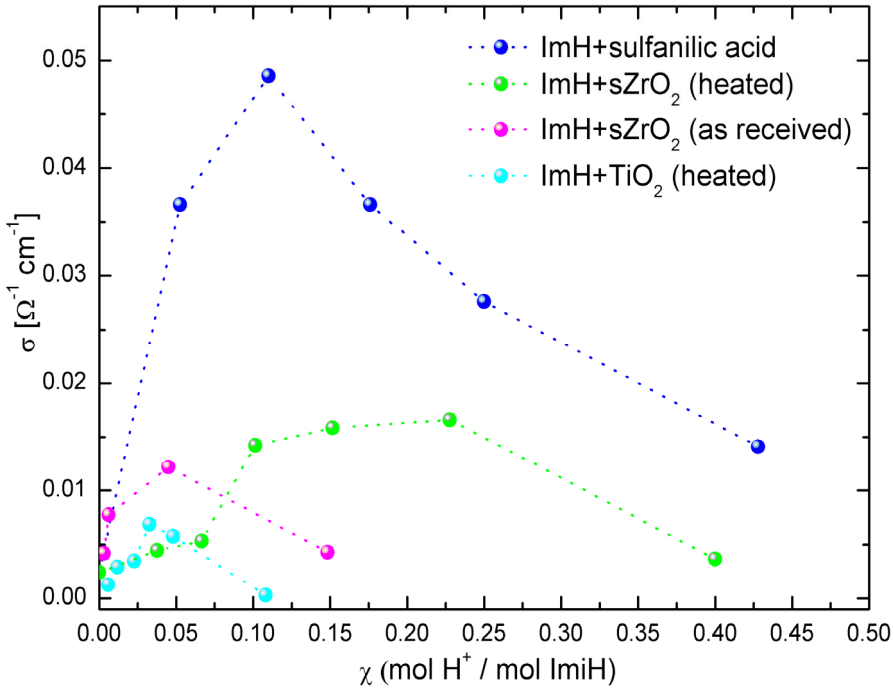

Figure 2.20: Comparison of the conductivity of composites as a function of mole fraction of protons at 90 °C.

2.4.3 Zeta Potential Measurements

Figure 2.21 shows the zeta potential measurements of as received oxide particles. The surface charge of the pure TiO_2 in 0.001 M KNO_3 solution is found to be -11.2 mV at pH 4.7. It, however, changes to -34.3 mV during the addition of imidazole to the system at the same pH. In the same way, the surface charge of $sZrO_2$ decreases from 4 mV to -23.9 mV and Al_2O_3 from 26.3 mV to -0.58 mV. Thus, the surface charge of the all inorganic oxides becomes strongly more negative on the addition of imidazole. This is consistent with the assumed adsorptive interaction of the active oxide surface leading to the formation of negative species on the oxide surface.

Using the determined c_0 values and relating them to the bulk concentration (derived from σ_∞), a potential of 130 mV is calculated for TiO_2. The calculated potentials of Al_2O_3 and $sZrO_2$ are 97 and 163 mV, respectively. Note that owing to the different experimental conditions of conductivity and zeta potential measurements, we can not directly compare the absolute values. One reason for the lower value derived from the zeta potential experiment may be the four times higher dielectric constant of the aqueous KNO_3 solution used.

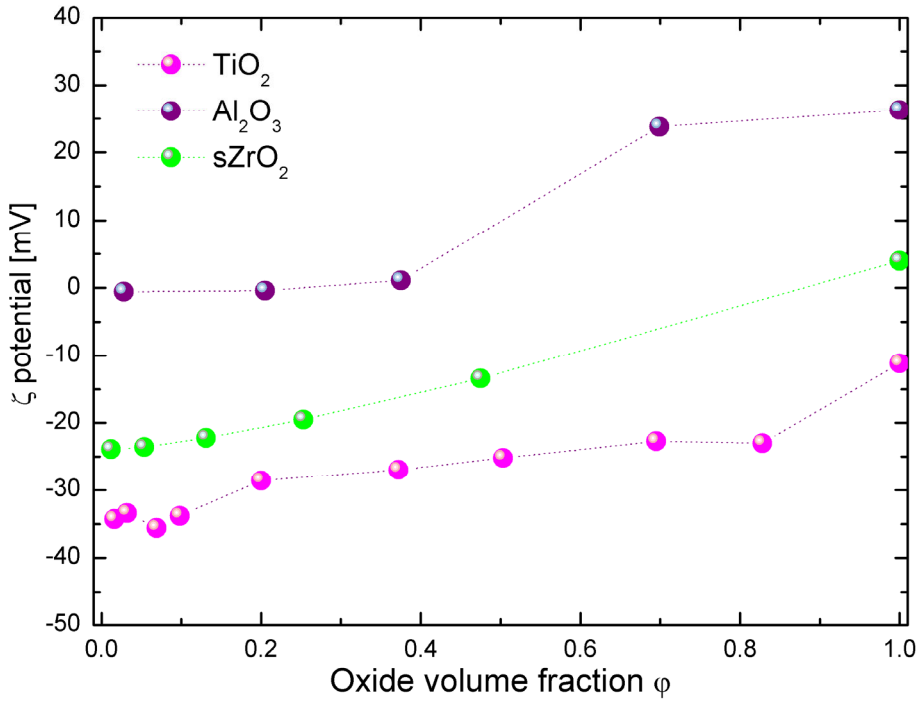

Figure 2.21:Room-temperature zeta potential variation upon addition of ImiH to several oxides.

2.4.4 PFG-NMR Measurements

In this work, the diffusion coefficients of protons coordinated to the imidazole nitrogen ($D(H_{NH})$) and the molecular diffusion coefficient ($D(H_{CH})$) are separated by a site-selective PFG-NMR technique. This technique, which had already been applied to the investigation of proton transport of organic imidazole containing systems[66], relies on the fact that proton transfer exclusively takes place between nitrogens, in particular there is no mixing of the NH and CH protons on the PFG-NMR time scale (typically 1 ms). The proton

diffusion coefficients obtained for pure imidazole and one ImiH-TiO_2 composite (22.6 wt%, φ = 6.9, IEC = 1.61 mmol/g) fall into a very narrow range (Figure 2.22), which is just a consequence of relatively low degrees of charge-carrier concentration and the high molecular self-diffusion coefficient of imidazole for both systems ($D(H_{CH}) \approx 10^{-5}$ cm^2 s^{-1}).

The average NH proton self-diffusion coefficient $D(H_{NH}^{av})$ is actually only about a factor of 1.04-1.06 higher than the molecular self-diffusion coefficient $D(H_{CH})$ for pure imidazole and a factor of 1.14-1.18 for the composite. It is worth noting that the admixture of titania (φ = 6.9) leaves the average molecular diffusion virtually unaffected.

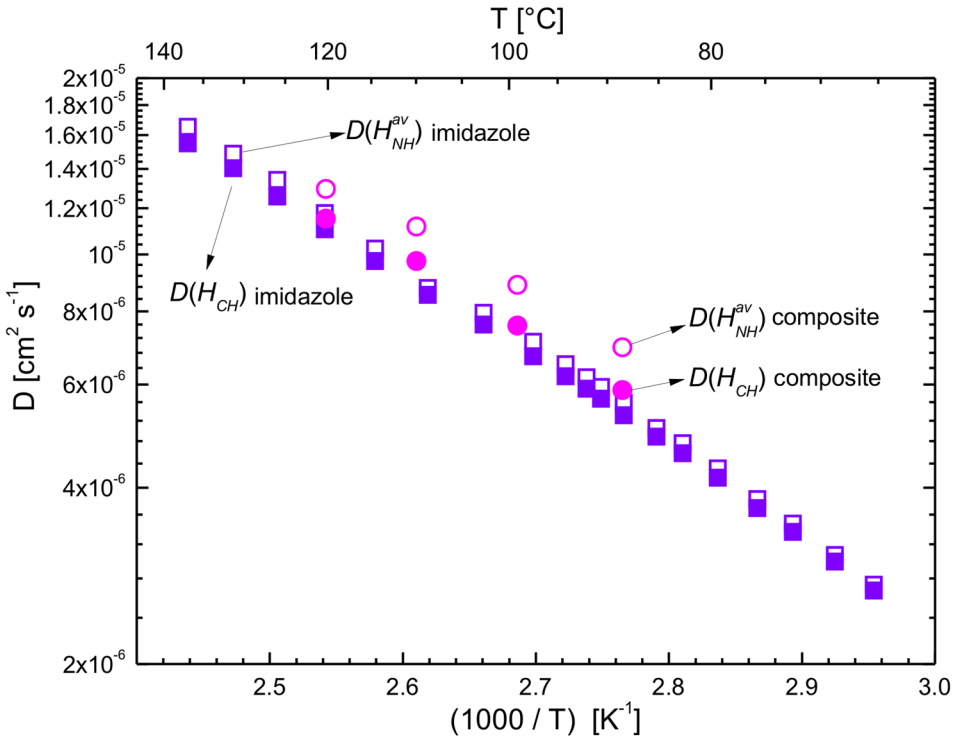

Figure 2.22: Self-diffusion coefficients of NH protons $D(H_{NH}^{av})$ and molecular self-diffusion coefficient $D(H_{CH})$ for pure ImiH and an ImiH–TiO_2 composite (22.6 wt%, φ =6.9 vol% TiO_2).

From these data, proton conductivities can be calculated, and these conductivities should be equal to the experimentally obtained conductivities provided possible correlation effects are identical for both proton diffusion and proton conductivity. From the molecular diffusion coefficient $D(H_{CH})$, the conductivity contributions from the diffusion of

imidazolium ($ImiH_2^+$) and imidazolate (Imi^-) ions (*vehicle mechanism*) are calculated according to:

$$\sigma_D^{vehicle} = \frac{F^2}{RT}\left(c(ImiH_2^+)\,D(ImiH_2^+) + c(Imi^-)\,D(Imi^-)\right) \approx \frac{F^2}{RT}\,2\,\alpha\,c(ImiH)\,D(H_{CH}) \tag{2.32}$$

with c(ImiH) being the concentration of imidazole molecules and F, R and *T* having their usual meanings. About four times smaller value of $\sigma_D^{vehicle}$ compared to the measured conductivity of pure imidazole (Figure 2.23) just confirms the earlier finding[65], but the availability of $D(H_{NH}^{av})$ now also allows the calculation of the conductivity contributions from structure diffusion $\sigma_D^{structure}$, which is approximated by:

$$\sigma_D^{structure} = \frac{F^2}{RT}c(H_{NH})\left(D\left(H_{NH}^{av}\right) - D\left(H_{CH}\right)\right) \tag{2.33}$$

Because this expression does not depend on the charge carrier concentration, the reliability of the values of $\sigma_D^{structure}$ is high. In the case of pure imidazole $c(H_{NH})$ simply equals c(ImiH) while for the composite, the concentration of the N bonded protons $c(H_{NH})$ is the sum of the concentration of imidazole and the excess protons stemming from either the dissociation of the titania surface or the adsorption of imidazolate:

$$c(H_{NH}) = c(ImiH) + 2\,c(ImiH_2^+) \tag{2.34}$$

The conductivity contributions from structure diffusion obtained in this way and the measured conductivities are shown in Figure 2.23 for neat imidazole and the composite. In order to obtain the overall values (σ_m) for the composite, the same average as introduced by Equation 2.21 has to be taken. In both cases, $\sigma_D^{structure}$ significantly exceeds the experimental conductivities: in the case of neat imidazole by a factor of 5-6 and for the composite by a factor of 8-9. This corresponds to Haven ratios (H) of 5-6 and 8-9, suggesting different mechanisms for H_{NH} diffusion and conductance (the difference between 5-6 and 8-9 being within or at least close to the accuracy limit).

As discussed by Kreuer et al.[102], this may be the consequence of long-range electrostatic interaction between charged defects and local details of the proton transport mechanism. The first effect strongly depends on the dielectric constant, which is most likely reduced within the layer of imidazole interacting with the polar titania surface. In this low dielectric region the mobility of protonic defects may be slightly more reduced than the diffusion of NH protons[102], and this may even explain the slight increase of the Haven ratio.

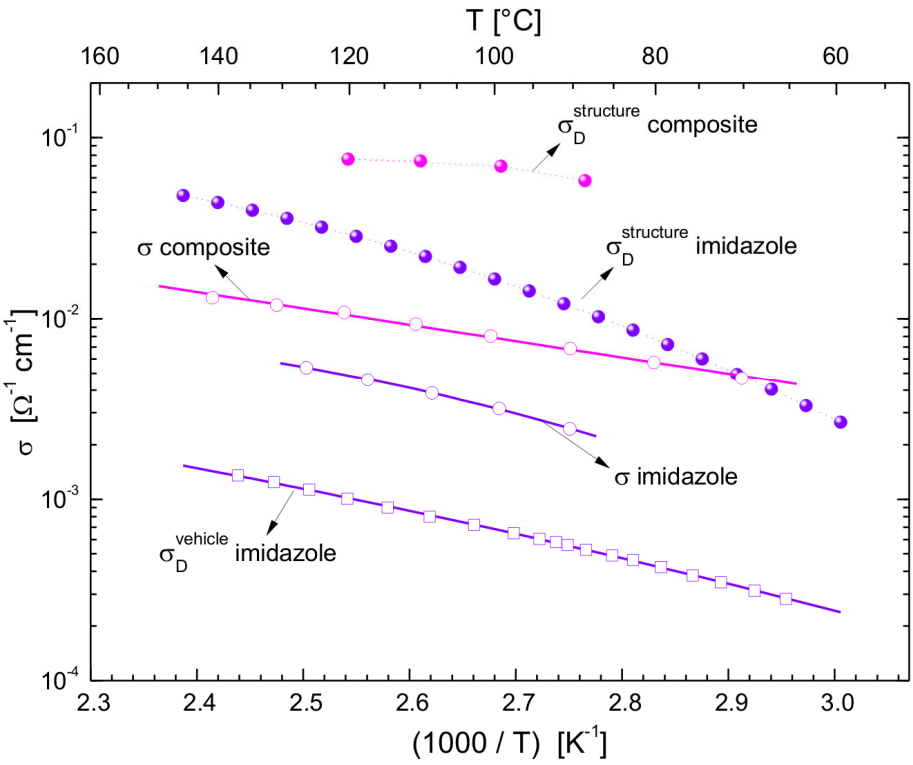

Figure 2.23: Comparison of conductivities σ determined by ac-impedance spectroscopy with conductivities σ_D calculated from ^1H self-diffusion coefficients of pure ImiH and an ImiH–TiO_2 composite (22.6 wt%, φ =6.9 vol% TiO_2). For pure imidazole the conductivity contribution from vehicle diffusion is also shown.

2.5 Conclusion

The purpose of this study is to understand the effect of oxide incorporation on proton conductivity of imidazole. It is demonstrated that the addition of nanometer sized acidic oxide particles (TiO_2, Al_2O_3, $sZrO_2$) enhances the ion conductivity of pure ImiH (~ up to a maximum of ten times in the case of $sZrO_2$). The heterogeneous doping concept, which

was originally applied to ceramic electrolytes and later on to solid polymer electrolytes and soggy-sand electrolytes in order to quantitatively explain the ion conduction mechanism of such composites, is shown to be valid also for a liquid weak proton conducting electrolyte. The experimental results are consistent with the formation of a space-charge layer on the oxide surface as a consequence of adsorptive interaction. Deviations from the first-order model used may be due to the percolation behavior, details of the adsorption process or mobility variation at the contacts.

3 Nafion/Oxide Composites

3.1 Introduction

Fuel cells are considered to be one of the solutions of the future problem of energy conversion. A fuel cell is a device wherein the chemical energy of a fuel (hydrogen, natural gas, methanol, gasoline, *etc*.) and an oxidant (pure oxygen or air) is directly converted into low voltage d.c electricity without going through Carnot's thermodynamic cycle. Therefore, it can attain higher efficiencies compared to that of a heat engine. In this sense a fuel cell as a special case of a galvanic cell, is similar to a battery. However, unlike these, it can continue to operate as long as the reactants and the products are continuously supplied and removed, respectively. Fuel cells have the advantages of high efficiencies, high energy densities and low or zero emission. They are quiet, clean, modular and can be made in a variety of sizes. Since they have no moving parts, they promise a long life. A critical part of a fuel cell is the separator material, electrolyte, which conducts ions but is electronically insulating. Different types of fuel cells are even named after the electrolyte that is used such as: SOFC (solid oxide fuel cell), MCFC (molten carbonate fuel cell), AFC (alkaline fuel cell), PAFC (phosphonic acid fuel cell) and PEMFC (polymer electrolyte or proton exchange membrane fuel cell).

The first operational principle of fuel cells was described by Christian Friedrich Schönbein in 1839. Although the first demonstration of a fuel cell was by William Grove[103] in 1839, it took over a century for a fuel cell to be practically used. The first successful usage of PEMFC in an operational system was the Gemini power plant in the early 1960s. However, this success was not enough to commercialize the fuel cells due to the limited performances and lifetimes which were the result of the degradation of poly (styrenesulfonic acid) membranes employed at that time[104]. The performance and lifetime of PEMFCs have significantly improved since Nafion® was developed by DuPont in the late 1960s. In 1990s a new industry was born with the production of the first passenger car running on PEMFCs. This system had already been known in 1960s, but its importance had felt behind the alkaline systems. In recent years, PEMFCs have been identified as promising power sources for vehicular transportation and for other applications requiring quick start up and portable power. In this type of fuel cell, a polymer membrane is placed

between two porous, electrically conductive electrodes. For a reversible fuel cell running on hydrogen and oxygen, the following electrochemical reactions occur at the two electrodes:

Anode: $$H_2 \rightarrow 2H^+ + 2e^-$$ (3.1)

Cathode: $$\frac{1}{2} O_2 + 2H^+ + 2e^- \rightarrow H_2O$$ (3.2)

Sum: $$H_2 + \frac{1}{2} O_2 \rightarrow H_2O$$ (3.3)

On the anode side, hydrogen diffuses to the anode catalyst where it later dissociates into protons and electrons. The protons are conducted through the membrane to the cathode, but the electrons are forced to travel in an external circuit because the membrane is electronically insulating. On the cathode catalyst, oxygen molecules react with the electrons (which have traveled through the external circuit) and protons to form water.

Perfluorosulfonated ionomer (PFSI) membranes (e.g., Nafion®) have been commonly used as an electrolyte in PEMFCs because of their excellent proton conductivity (0.1 S/cm at 25 °C) under fully hydrated conditions[58-60]. Nafion® membranes have proven to have a lifetime exceeding 11,000 h when operated at 80 °C, 100% relative humidity (RH)[105]. However, at slightly undersaturated conditions, Nafion® quickly looses its desirable ionic conductivity[61-63] which cause fuel cell performance degradation[106-109]. This major drawback of Nafion® limits the PEMFC application to approximately T = 90 °C. Higher service temperatures are desired in order to reduce CO poisoning of the electrode catalysts and the need for noble metal catalysts. The extension of the operation temperature above 100 °C would also increase the electrode kinetics of the oxygen reduction reaction and simplify water and thermal management. Although, the PTFE backbone of Nafion® gives this material a long term electrochemical stability, it is proven that Nafion® can suffer from degradation[110-114]. Also mechanical strength of the membranes above the glass transition temperature (ca. 105 °C) tends to deteriorate[115]. Therefore, significant efforts have been made to modify Nafion® to achieve suitable operation at elevated temperatures. One viable approach is the incorporation of inorganic oxide particles into the membrane. It has been

reported that such incorporation can extend the operation temperature of PEMFCs and DMFCs[40-42, 44-48, 52, 53, 56, 57, 64]. Among others, especially improved water retention and mechanical properties or specific chemical interactions between polymer sulfonate groups and the metal oxide surface have been suggested to account for the increased performance. However, these hypotheses are not fully supported by experimental observations. There is a big debate about the effects of the oxide incorporation into Nafion® on the fuel cell performance. A better understanding of the effects of oxides is essential since it could suggest new routes to enhance the fuel cell performance.

The motivation of this part of the work, therefore, is to investigate the effects of inorganic oxide admixture on proton conductivity, microstructure and mechanical properties of Nafion® membranes for which performance improvements had been proven before[43, 57]. Thermal/hydrothermal treatments are applied to the membranes in order to get insight into the properties of the materials at high temperature and low humidity conditions. In this way, it is planned to understand the reasons for the better fuel cell performance of the composite membranes under high temperature/low humidity fuel cell operation conditions. Various experimental techniques namely, Impedance Spectroscopy, Dynamic Mechanical Analysis (DMA), Small-angle X-ray Scattering (SAXS), Solid State NMR and Attenuated Total Reflection Infrared (ATR-IR) Spectroscopy are employed to characterize the membranes.

3.2 General Part

3.2.1 Fuel Cell Basics

3.2.1.1 Thermodynamics

Gibbs free energy, ΔG, of a chemical reaction is a measure of maximum net work obtainable from the reaction. In a fuel cell, as a result of hydrogen combustion to liquid water (equation 3.3) only a portion of the reaction enthalpy, ΔH can be converted into electrical energy due to loss of entropy, ΔS.

$$\Delta G = \Delta H - T\Delta S \tag{3.4}$$

At standard temperature and pressure (STP), 286 kJ mol^{-1} energy is produced as a result of hydrogen combustion to liquid water. Out of this 237 kJ mol^{-1} can be converted into electrical energy while the rest is transformed into heat.

The standard potential E^0 of a cell reaction, i.e. the potential at STP under current-less reversible condition, is correlated with the corresponding Gibbs energy change of the reaction at STP (ΔG^0) as follows:

$$\Delta G^0 = -nFE^0 \tag{3.5}$$

where n is the number of electrons transferred and F is the Faraday constant (96485.3 C mol^{-1}). According to the equation 3.5, at 25 °C the theoretical H_2/O_2 fuel cell potential is calculated as 1.23 V.

For a H_2/O_2 fuel cell reaction, the actual cell potential can be calculated by using Nernst equation as follows:

$$E = E^0 + \frac{RT}{nF}\ln\left(\frac{P_{H_2}P_{O_2}^{0.5}}{P_{H_2O}}\right) \tag{3.6}$$

where R is the universal gas constant, T the temperature in Kelvin, F is the Faraday constant, n is number of electrons each H_2 molecule provides (i.e. 2).

3.2.1.2 Kinetics

Concerning a simple elementary redox reaction at an interface:

$$Ox + ne^- \underset{k_b}{\overset{k_f}{\rightleftharpoons}} Red \tag{3.7}$$

where k_f and k_b are the rate constants for the forward and the backward reactions, respectively, the net current is the difference between the electrons released (oxidation of the reducing species, *Red*) and consumed (reduction of the oxidizing species, *Ox*).

$$i = nFj = nF\,(k_f C_{ox} - k_b C_{red}) \tag{3.8}$$

where nF is the charge transferred, j is the flux, C_{ox} and C_{red} are the concentration of the reacting species.

At equilibrium, the net current is zero. The reaction proceeds in both directions at the same rate. This rate is called exchange current density i_0 (per unit of electrode geometrical area), which is a measure of the electrode ability to support the respective electrochemical reaction. The higher the exchange current density, the more active is the surface of the electrode. In a H_2/O_2 fuel cell, the anode exchange current density (oxidation of H_2) is much larger than the cathode exchange current density (reduction of O_2).

The relation between current density i and potential E is for simple conditions given by Butler-Volmer equation:

$$i = i_0 \left\{ \exp\left[\frac{\alpha_A nF(E - E_r)}{RT} \right] - \exp\left[-\frac{\alpha_C nF(E - E_r)}{RT} \right] \right\} \tag{3.9}$$

where i_0 is the exchange current density, α_A and α_C (1- α_A) the charge transfer coefficients for the anodic and cathodic reaction which is best considered as the fraction of the change of overpotential that leads to a change in the rate constant for charge-transfer reaction. The cell voltage at zero net and also local current is called equilibrium or reversible cell potential, E_r. The difference between the respective cell potential and the reversible cell potential (E- E_r) is referred to as overpotential, η. The theoretical cell voltage of a H_2/O_2 fuel cell, E = 1.23 V at STP is practically not achievable. Whenever a net current is flowing, the cell voltage is reduced by polarization (overvoltage) effects. There are various types of overvoltage such as activation, ohmic and concentration polarization, which lead to irreversible losses. The activation polarization η_{act}, results from the slow rate of the charge transfer reaction which occurs across electrode-electrolyte interface. Ohmic losses η_{ohm}, are simply the voltage drop across the resistive components of the cell. In our context the ohmic resistance of the electrolyte is to the fore. Concentration losses η_{conc}, are observed when a concentration gradient is formed between the electrode surface and bulk. Slow transport of reactants and products to and from the electrochemical reaction site is the major contribution to the concentration polarization. Concentration polarization may cause the cell potential to decrease rapidly to zero. The current (density) corresponding to the zero cell potential is called limiting current (density). These losses are shown in polarization curve (Figure 3.1).

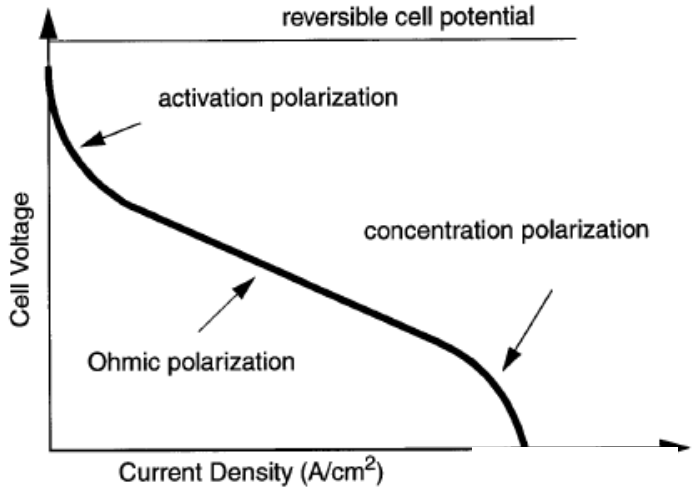

Figure 3.1: Typical polarization curve of a fuel cell with major loss contributions.

3.2.1.3 Fuel Cell Efficiency

The ratio between usable energy output and energy input is defined as efficiency:

$$\eta = \frac{E_{out}}{E_{in}} \qquad E_{out} < E_{in} \tag{3.10}$$

Assuming that an electrochemical energy converter is working ideally, that is totally reversible, the withdrawn electrical energy equals the change in free energy. Thus, the thermodynamic efficiency of a fuel cell can be given by:

$$\eta = \frac{\Delta G}{\Delta H} \tag{3.11}$$

Using the higher heating value of hydrogen (the produced water is in liquid state, higher entropy loss), the maximum theoretical efficiency value of a fuel cell is calculated as 83%. With the produced water in gaseous state (lower entropy loss), 95% efficiency can be obtained. If the reaction entropy is positive (i.e., $2C+O_2 \rightarrow 2CO$), the reversible efficiency is greater than 100%. In such reactions thermal energy taken from surroundings is converted into electrical energy.

3.2.2 Membrane Electrode Assembly (MEA)

A typical PEMFC is depicted in Figure 3.2. The multilayer assembly of the membrane sandwiched between two electrodes is called membrane electrode assembly (MEA). The MEA is located in between two flow plates which distribute the reactant gases across the face of the MEA and collect the electrical current from the MEA. Because of the reason that the voltage of a fuel cell is quite small, many cells have to be connected in series to produce a useful voltage. Such a collection of fuel cells in series is called a ´stack` and it is achieved by connecting the edge of each anode to the cathode of the next cell. If the connections are made all over the surface of one cathode and the anode of the next cell, then it is called a ´bipolar plate`. The bipolar plates must be electrically and thermally conductive and impermeable to gases. They must have adequate strength as well as light weight. Metallic plates coated with non corrosive yet electrically conductive layers such as graphite and conductive polymers or thermoplastics (polyethylene, polypropylene) with fillers (carbon black, carbon/graphite powder) are the materials used for fuel cell bipolar plates.

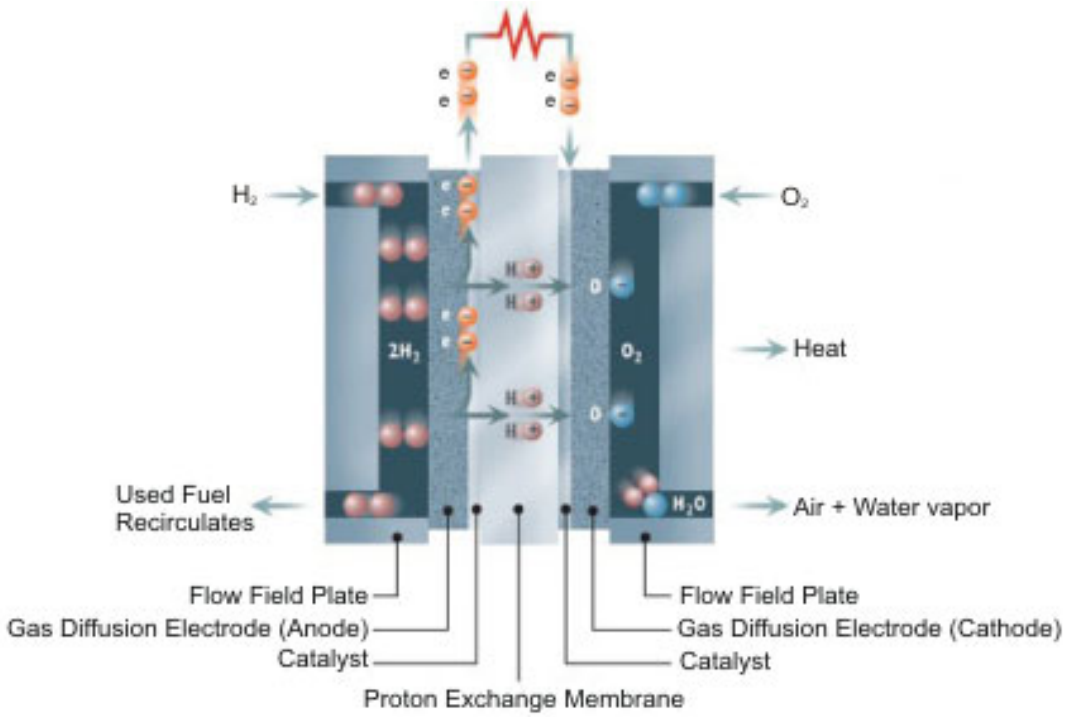

Figure 3.2: PEMFC components and the basic principle of operation.

3.2.3 Main Fuel Cell Components

The main components of a PEM fuel cell are the followings:

- Polymer Electrolyte Membrane (PEM)

- Electrodes: Anode and Cathode

- Gas Diffusion Layer (GDL)

- Collector Graphite Plates

3.2.3.1 Polymer Electrolyte Membrane (PEM)

The polymer electrolyte membrane (PEM) is an electronic insulator, but an excellent proton conductor. High proton conductivity, high chemical and thermal stability, good mechanical properties, low water drag, fast kinetics for electrode reactions, low gas permeability, low cost and ready availability are the requirements that have to be fulfilled for a polymer electrolyte membrane to be used in a fuel cell.

Typically, PEMs are ionomeric materials that contain a small fraction of ionic groups covalently bonded to the polymer backbone as pendant moieties. The amount of ionic groups in an ionomer is generally presented in terms of either equivalent weight (EW=grams of polymer per mole of the ionic group) or ion exchange capacity (IEC=1000/EW). Among commercially available ionomers such as Flemion® (Asahi Glass Co.) and Aciplex® (Asahi Chemical Industry Company), Nafion® (DuPont) is the most frequently studied ionomer in literature. The chemical composition of Nafion® is shown in Figure 3.3, where x = 5-13, y = z = 1, *n* = ca. 1000. Generally, characterizing numbers such as “117, 115, 112” are given to specify the respective membrane, i.e. the numeral 117 stands for an EW of 1100 with a thickness of 0.007 inches. Nafion® incorporates the high hydrophobicity of the poly(tetrafluoroethylene) (PTFE) backbone with the high hydrophilicity of the side chains terminated with a sulfonic acid group ($-SO_3H$) which imparts proton conductivity to the polymer.

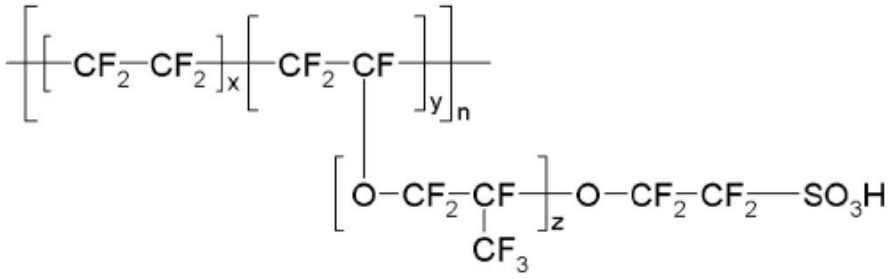

Figure 3.3: Chemical structure of Nafion®.

Nafion® films are produced by both extrusion and solution casting processes. Extruded Nafion® is synthesized by the copolymerization of tetrafluoroethylene (TFE) and a derivative of a perfluoro (alkyl vinyl ether) with sulfonyl acid fluoride. From the resulting $-SO_2F$ containing thermoplastic precursor, sheets of required thickness are extruded. Hot aqueous NaOH is used to convert sulfonyl fluoride ($-SO_2F$) groups into sulfonate groups ($-SO_3^-Na^+$). This neutral or salt form of Nafion® is finally converted to the acid form containing sulfonic acid ($-SO_3H$) groups. Commercially available dispersions of Nafion® in selected solvents are employed to form recast Nafion® membranes. These membranes are preconditioned (purified, acidified) before usage.

3.2.3.1.1 Water Uptake

The water content in the membrane is expressed either as volume fraction (φ) or as ratio of moles of water molecules to moles of sulfonic acid group present in the polymer (λ)[116]. With increasing temperature, generally water uptake increases, yet the absolute value depends on the membrane pre-treatment. Membranes dried out at T=105 °C are shown to have lower water uptake capacities than the membranes dried at room temperature[117]. This is attributed to the morphological changes of the membranes above glass transition temperature (T_g). It has been reported that the water uptake of polymer electrolyte membranes equilibrated with liquid water is higher than the water uptake of membranes equilibrated with water vapor under the same conditions. This phenomenon, known as Schroeder's paradox[118], is inconsistent with thermodynamics. Many papers have been dedicated to this phenomenon and many different explanations have been reported[119-122].

The vapor uptake isotherm can be divided into two main regions[63]: 1) low vapor activity region, i.e. from 15 to 75 % relative humidity (RH). In this region, there is a relatively gradual increase in the water uptake which corresponds to the uptake of water by solvation of the ions in the membranes; 2) high water activity region, i.e., from 75 to 100% RH. In this region water involves in polymer swelling. Therefore, a steep increase in the water uptake with increasing water activity is observed.

3.2.3.1.2 Proton Conductivity

The proton conduction in perfluorosulfonic acid ionomer (PFSI) membranes depends on the water content, diffusion coefficients, and concentration and distribution of the excess protons. High concentration of water molecules in the system together with the relatively large diameter of the interconnecting channels between ionic clusters promotes water diffusion.

Dependency of proton conductivity of Nafion® on relative humidity is studied by Anantaraman and Gardner[61] and the proton conductivity decay with decreasing humidity is reported. A decrease in proton conductivity with decreasing water content is shown by Zawodzinski et al[63]. Both temperature and humidity dependency of proton conductivity is investigated by Sone et al[62].

At the highest degree of hydration, large water content in the system shields the charge associated with the sulfonic acid anion, and preserves the system symmetry (hydrogen bond network), leading to quicker reorientation of water molecules and formation of a continuous pathway for the protons across the medium. Therefore, in a well-hydrated membrane, the major proton conduction mechanism is structure diffusion. At low humidity levels, there are fewer water molecules per sulfonic acid group, resulting in concentration increase and poor shielding of the protonic charge carriers. In this case, hydrogen bonds get tighter which leads to a reduced rate of bond breaking and forming processes. Therefore, intermolecular proton transfer is suppressed and protons preferentially diffuse as a part of bigger species (vehicle mechanism)[74, 123].

The effects of thermal/hydrothermal treatments on proton conductivity of Nafion® 117 have been recently studied and noticeable proton conductivity decay observed. The

proposed hypotheses intending to explain the decay of conductivity are not fully supported by the experimental observations. Alberti et al. showed that the conductivity of the heat-treated Nafion® 117 (140 °C, 100 % RH for 3 days), measured at 100 °C and 100% RH, is lowered approximately by 30% compared to that of the untreated membrane[124]. As the change of the ion exchange capacity (IEC) upon heat treatment is not significant, the conductivity decay is attributed to the irreversible crystallization of the polymer. Unfortunately, information about the crystallinity and the IEC of the membrane is not given. It is also observed by Casciola et al. that after 4 days equilibration of Nafion® 117 at 120 °C and 95 % RH, the conductivity of the membrane decreases by 25%[125]. The reason for this conductivity decrease is not discussed. Sone et al. analyzed the conductivity of a commercial Nafion® 117 membrane before and after annealing the membrane at 80, 105 and 120 °C for 10 hours. Reduction of the proton conductivity after heat-treatment is observed for the membranes which are measured under different relative humidities (20-100% RH). The most significant decay in conductivity is observed for the heat treated membrane that is measured at low relative humidities. This behavior is explained by the shrinkage and the low water content of the membrane[62]. However, there is no information available about the water content of the membrane.

3.2.3.1.3 Morphology

It is generally accepted that because of Coulombic interactions, the polar perfluoroether side chains containing sulfonic acid groups tend to aggregate, leading to a nanophase-separated morphology where the ionic domains, termed clusters, are distributed over the nonpolar PTFE matrix. In addition, randomly distributed crystalline domains which have a crystal structure similar to poly(tetrafluoroethylene) (PTFE) are detected (for PTFE crystallinity is 100%, for Nafion 117 ~3-12%)[59]. This complex, phase-separated morphology has been focus of several investigations. The cluster-network model of Gierke et al. can be considered as the most widely referenced model[126]. Based on small-angle X-ray scattering (SAXS) studies and several further assumptions, the model proposes that there are clusters of sulfonate-terminated side chains that are organized as inverted micelles and these micelles are interconnected by a network of short and narrow channels which allow water and ion transport. Another model proposed by Yeager and Steck depicts a three-phase model based on a fluorocarbon phase, an interfacial region and ionic

clusters[127, 128]. Yeo and Eisenberg proposed one of the first theories which explain the formation of ionic clusters in organic polymer[129]. The other models that have been proposed to date include a core-shell model by Fujimura et al.[130], a rod-like model by Rubatat et al.[131], a sandwich-like model by Haubold et al[132] and an inverted-micelle cylinder model by Schmidt-Rohr et al.[133]. Consistency between these models includes a network of ionic clusters; the models differ in the cluster geometry and distribution. Over the last 30 years, a wealth of morphological information from numerous scattering and diffraction studies of Nafion® has been obtained and reported. However, a universally accepted morphological model for the solid-state structure of Nafion® has not been given due the low crystallinity, complexity of co-organized crystalline and ionic domains and morphological variations with solvent swelling.

3.2.3.2 Electrodes

A fuel cell electrode is a thin catalyst layer where the electrochemical reactions take place. The catalyst surface must be in contact with the electrically conductive surface in order to allow electrons to travel through and it must have a contact with ionomer to allow protons to have an access to meet with electrons. The electrode must be porous and thin to allow reactant gases to travel to the reaction sites and to minimize the cell potential losses due to the rate of proton diffusion. The product water must be effectively removed to prevent flooding of the electrode. Therefore, the catalyst layer must be hydrophobic. The most common catalyst in PEM fuel cells is platinum (Pt) since it is the most active electrocatalyst for the oxygen reduction reaction and has high stability to operate in the acidic medium. It is important to have small Pt particles with large surface area which are finely dispersed on the surface of catalyst support (carbon). The catalyst surface active area can be enlarged by incorporating ionomer in the catalyst layer or coating it with thin ionomer layer except for some allowance for electrical contacts. The attachment of the catalyst layer to the ionomer membrane is achieved by first depositing the catalyst layer to the porous substrate, and then hot-pressing it to the membrane.

3.2.3.3 Gas Diffusion Layer

A gas diffusion layer is a porous substrate between catalyst layer and bipolar plate that provides a pathway for reactant gases to flow to the catalyst layer and for product water to

flow to the field channels. It must be both electrically and thermally conductive, and must have rigidity and flexibility. The best materials that meet these requirements are carbon fiber based materials such as carbon fiber papers or carbon cloth. Typically, both anode and cathode gas diffusion media are PTFE treated in order to avoid flooding.

3.2.4 Shortcomings Associated With Low Temperature Operation

3.2.4.1 CO Poisoning

Reformed fuels such as natural gas, gasoline, or alcohols contain small amounts of CO and even trace amounts of CO (more than 10 ppm) poison the Pt catalyst at the anode. The reason is the very high affinity of the CO molecule to the platinum surface at relatively low operating temperatures. Alloy electrocatalyst (e.g, Pt-Mo, Pt-Ru[134-137]) show good activity towards hydrogen oxidation in the presence of CO and CO_2. However, problems still exist due to i) a 5-10 times higher Pt loading than required for pure Pt catalyst, ii) their tolerance level is about 50 ppm which is still not sufficient. Owing to the fact that the absolute free energy of adsorption of CO on Pt has a larger positive temperature dependence than that of H_2, lower CO coverage can be achieved by raising cell temperature above 100 °C. The CO tolerance will be drastically enhanced, from 10-20 ppm at 80 °C, to 1000 ppm at 130 °C. This high CO tolerance makes it possible for a fuel cell to use hydrogen directly from a reformer and also leads to a reduction in electro-catalyst loadings.

3.2.4.2 Water Management

To achieve sufficient membrane hydration, water is supplied to the membrane by the humidification of the feed gases and it is also produced at the cathode by electrochemical reduction of oxygen. Under fuel cell operation conditions, the protonic current through the membrane produces an electro-osmotic water current which leads to a depletion of water at the anode, resulting in an increased membrane resistance. Water generation and electro-osmotic drag build up a large concentration gradient across the membrane. Because of this gradient, water back diffuses from cathode to the anode. However, some amount of water produced at the cathode does not dissolve in the electrolyte and back diffuse to anode, instead, is carried out of the fuel cell by excess oxidant flow. Thinner membranes are required to assure sufficient back diffusion.

Operation of a PEMFC at a temperature close to the boiling point of water involves a dual-phase water system. When the humidification is too high, water condenses and gas diffusion electrodes are flooded. Above the boiling point of water, the operation of a fuel cell is simplified by involving a single phase of water.

The equilibrium partial vapor pressure of water can not be compensated at above 100 °C at normal atmospheric pressure. In order to keep the membrane hydrated, the total cell pressure has to be raised above 1 atm. Pressurized operation results in a large loss in the system efficiency because of the energy needed to compress the oxidant air. Membranes that are capable of operating at reduced humidities would not require pressurization at elevated temperatures.

3.2.5 New PEMs for High Temperature Operation

As discussed above, operating the PEMFCs at higher temperatures (T >100 °C) and reduced humidities avoids most of the shortcomings associated with the low-temperature operation. Nafion® and other perfluorinated PEMs have been widely used because of their excellent proton conductivity (0.1 S/cm at 25 °C) under fully hydrated conditions. However, at elevated temperatures Nafion® quickly looses its desirable ionic conductivity due to the membrane dehydration, thus limiting the PEMFC application to approximately 90 °C. Therefore, there are several approaches being employed to synthesize new PEMs with the ultimate goal of elevated temperature and low humidity operation. These may be generalized under three main themes:

1) Modifications of PFSI membranes with

a) Hygroscopic oxides (e.g., SiO_2, TiO_2, ZrO_2)[40, 42, 46-48, 52-54, 56, 57, 138]

b) Inorganic solid proton conductors (e.g., zirconium phosphates[81, 139-141], heteropolyacids[142, 143])

c) Organically modified silicates[49, 53, 144, 145]

2) Alternative sulfonated polymer membranes and their composites

a) Fluoropolymers[146] (e.g., sulfonated styrene grafted poly(vinylidene fluoride)[146, 147], styrene grafted poly(tetrafluoroethylene-co-hexafluoropropylene[148]))

b) Sulfonated hydrocarbons (e.g., sulfonated polyetheretherketones (SPEEK[149, 150]), sulfonated polysulfones (SPSF)[151, 152], sulfonated polyimides (SPI)[153, 154])

3) Acid-base polymer membranes

a) Phosphoric acid or sulfuric acid doped polymers having basic sites such as, imine, amide, or imide groups (e.g., acid doped polybenzimidazole (PBI)[155, 156])

b) Modifications of acid-base polymers with inorganic oxides and organic plasticizers (e.g., polyethyleneimine (PEI)/H_3PO_4/SiO_2[157], PVDF/DMF/H_3PO_4[158])

c) Organic acid-base blends (e.g., SPSF or SPEEK/PBI[159]) and further doped acid base blends (e.g., SPSF/PBI/H_3PO_4[160]).

3.2.6 Nafion®/Oxide Composite Membranes: A Literature Survey

Composite membranes of Nafion® modified by inorganic additives (e.g., SiO_2, TiO_2, ZrO_2) have been developed and studied during the last few decades[40, 42, 46-48, 52-54, 56, 57, 138]. General motivations for fabricating inorganic-organic composite ionomers may include the following: 1) improving self-humidification of the membrane at the anode side; 2) reducing the electro-osmotic drag and therefore the drying-out of the membranes at the anode side; 3) suppressing fuel crossover; 4) improving the mechanical strength of the membrane; and 5) improving thermal stability.

Inorganic-organic composite membranes can be prepared by: 1) in-situ formation of inorganic components in a polymer membrane or in a polymer solution, or 2) casting a bulk mixture of inorganic oxides with a polymer solution.

A simple procedure to grow an inorganic phase inside an organic matrix by hydrolysis and condensation of alkoxy silanes is named as sol-gel process. Mauritz et al. investigated in-situ formation of silica in recast Nafion® via hydrolysis of tetraethoxysilane (TEOS) in 1995[161]. Upon admixture of silica particles into Nafion®, an increase in water uptake and

ionic conductivity and a decrease in MeOH permeability is observed[53]. Extension of the PEMFC and DMFC working temperature above 100 °C is also detected. For a Nafion® 115 membrane in an H_2/O_2 cell at 130°C (gases pre-humidified at 130 °C and 3 atm of pressure), the current density improves approximately four times by the addition of 6% w/w SiO_2. More significantly, 6% w/w SiO_2 silica doped Nafion® 115 MEA withstands operation for at least 50 h at 130°C (humidifiers 130°C), whereas the undoped Nafion®115 membrane fails in less than 1 h[64]. Unfortunately, proton conductivity data of these membranes is not available.

Composite membranes with 3% w/w TiO_2 loading are tested in a single cell between 80 and 130 °C in humidified H_2/air. Higher current densities are obtained for the composite membranes compared to Nafion® 115[56]. The result is attributed to the higher water uptake and ion exchange capacity of the composites compared to the bare recast membrane. However, there is no available information about the water uptake of the membranes at the given temperature and humidification.

Compared to the parent membrane Nafion® 112 and membranes containing SiO_2 and TiO_2, the Nafion®-ZrO_2 composite membrane (the amount of inorganic oxide in the membranes is not specified) is observed to have higher water uptake, ion exchange capacity, and conductivity at 90 and 120 °C over the complete range of water activity. Although composites containing SiO_2 and TiO_2 demonstrate higher water uptake, they show lower conductivity than Nafion® 112. Therefore, it is concluded that higher water uptake does not inevitably result into higher conductivity. Despite the fact the ZrO_2 containing membrane takes-up more water and has better conductivity at a given temperature and relative humidity compared to Nafion® 112, the H_2/O_2 fuel cell performance of the composite and Nafion® 112 are found to be nearly the same at 110 °C (humidifiers, 80°C)[52].

Composite membranes prepared by casting a bulk mixture of inorganic oxide with a polymer solution also show impressive PEMFC and DMFC performances, especially at high temperatures. Among a large number of studies, some recent investigations are summarized below.

Composite membranes prepared by using TiO_2 with different surface areas are compared by a H_2/O_2 fuel cell test. The composite containing titania with higher specific surface area and zeta potential shows a four times higher current density at 120 °C and 26% RH in a H_2/O_2 fuel cell[47]. Another study of the same author exhibits that at 120 °C and 50% RH the Nafion/20% w/w TiO_2 membrane delivers about six times higher current density than that obtained with an unmodified Nafion® membrane. This improvement is mainly attributed to the enhanced water uptake and the proton conductivity (at 120 °C between 20 and 100% RH) of the composite membranes although there is no data available about water uptake at the given conditions[48].

The composite membranes containing different percentages of ZrO_2 and recast Nafion® in a commercial single H_2/air fuel cell from 80 to 130 °C at 100 % RH are investigated by Saccà et al. The composite containing 10% w/w ZrO_2 shows better fuel cell performance especially at high temperatures compared to the recast Nafion® which is attributed to the higher water uptake of the membrane. There is no information provided about proton conductivity[57]. The work of Navarra et al. exhibits that 5 wt% incorporation of sulfated zirconia ($sZrO_2$) increases water retention and thermal stability of the recast Nafion® membranes. The proton conductivity of the composite membrane remains stable at high temperatures, i.e. extending up to 150 °C, while Nafion® looses its conductivity dramatically beyond 100 °C[54]. In the last two studies that are mentioned above, the water uptake measurements are performed by room temperature gravimetric measurements which hardly give information about the water uptake of the membranes during fuel cell operation.

It is observed by Satterfield et al. that addition of TiO_2 particles improves the fuel cell performance at 80 °C, 100 % RH[162]. The composite membrane shows lower resistivity at high humidification. However, the measurements of equilibrated water sorption do not show any significant increase in the water content due to the presence of oxide particles. The reason of the performance and conductivity increase is not clear.

In another study, composites of Nafion® with 3% w/w inorganic oxide particles (SiO_2, TiO_2, Al_2O_3 and ZrO_2) of various sizes are investigated in a H_2/O_2 fuel cell at 130 °C and different relative humidities ranging from 75 to 100%. At 100% RH, there is no

remarkable difference in fuel cell performance due to oxide impregnation. At lower relative humidities, while the cell potential of Nafion® at a certain current density decreases steeply and irreversibly by operation time, the cell potential of the composites decreases less steep and shows higher reversibility. It is suggested that there is a specific chemical interaction between polymer sulfonate groups and metal oxide surface which explains the better fuel cell performance of the composite membranes[40].

Ye et al. investigated transport properties of Nafion® 112 and Nafion®/SiO_2 composite membranes. The proton diffusion coefficients of the pre-dried Nafion®/SiO_2 composite obtained by PFG NMR are found to be about two times higher than the proton diffusion coefficients of Nafion® 112. However, there is an insignificant difference in diffusion coefficients between hydrated Nafion® 112 and Nafion®/SiO_2 composite membranes. The conductivity measurement results are consistent with the PFG NMR data. These results are explained as: i) in the dried composites, the proton transport is achieved by Grotthuss hopping mechanism on the surface of the oxides, ii) in the hydrated membranes, since proton transport is dominated by vehicle mechanism, insignificant difference in proton diffusion between composite and bare membrane is observed[138].

3.2.7 Experimental Techniques

3.2.7.1 Attenuated Total Reflection Infrared (ATR-IR) Spectroscopy

Attenuated total reflection infrared (ATR-IR) spectroscopy is a special mode of conventional IR spectroscopy which is used for analysis of the surface of materials. It is also suitable for characterization of materials which are either too thick or absorbing too strong to be analyzed by transmission spectroscopy. The method takes advantage of the difference between refractive indices of the sample being measured and a high-refractive index crystal such as Si, Ge, or diamond. In ATR-IR spectroscopy, the infrared radiation passes through an infrared transmitting crystal with a high refractive index, allowing the radiation to reflect within the crystal several times. To obtain internal reflectance, the angle of incidence must exceed the so-called ‘critical’ angle. This angle is a function of the real parts of the refractive indices of both the sample and the ATR crystal:

$$\theta_c = \sin^{-1}(n_2 / n_1) \tag{3.12}$$

where n_2 is the refractive index of the sample and n_1 is the refractive index of the crystal. This internal reflectance creates an evanescent wave that extends beyond the surface of the crystal into the sample held in contact with the crystal. The evanescent wave decays into the sample exponentially over a distance of the order of microns. The depth of penetration d_p depends on the angle of the incident beam θ, the optical constants of the interface and on the wavelength of radiation λ. It is given by

$$d_p = \frac{\lambda / n_1}{2\pi\sqrt{\sin^2\theta - (n_2 / n_1)^2}} \tag{3.13}$$

In regions of the infrared spectrum where the sample absorbs energy, the evanescent wave will be attenuated or altered and less intensity is reflected.

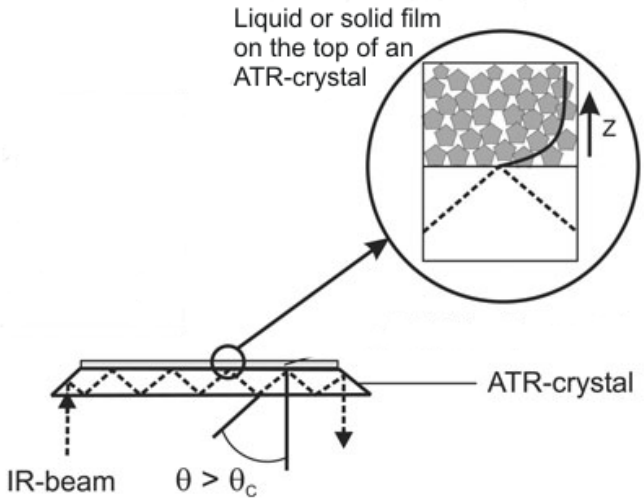

Figure 3.4: Schematic representation of the ATR-IR principle.

3.2.7.2 Small-Angle X-Ray Scattering (SAXS)

Small angle X-ray scattering (SAXS) is an analytical X-ray diffraction technique used for the structural characterization of solid and fluid materials in the range that extends from few interatomic distances up to hundreds of nanometers[163]. In a SAXS instrument, a monochromatic beam of X-rays having wavelength λ is sent through a sample. Some of the X-rays scatter, while most simply pass through the sample without interacting with it. Scattering is only observed when local electron density inhomogeneities exist in the

sample. During a SAXS measurement, the intensity of the scattered wave, which contains information on the structure of the sample due to the interaction with the electronic environment of the material, is recorded as a function of the scattering angle θ. For a phase-separated system, the invariant quantity Q of overall mean square electron density fluctuation is obtained by integrating $I(q)q^2$ all over the scattering angles.

$$Q = (1/2\pi)\int I(q)q^2 dq \tag{3.14}$$

where $I(q)$ is the scattering intensity at the scattering vector q.

The scattering SAXS patterns are typically represented as scattered intensity as a function of the magnitude of the scattering vector q which is defined as:

$$q = \frac{4\pi}{\lambda}\sin(\frac{\theta}{2}) \tag{3.15}$$

The dependence of $I(q)$ on q follows:

$$I(q) \propto q^{-\alpha} \tag{3.16}$$

The exponent α is related to the mass fractal dimension D_v and to the surface fractal dimension D_s of the scatter structures according to the equation:

$$\alpha = 2D_v - D_s \tag{3.17}$$

For mass fractals, α takes values in between 1-3 ($1 < \alpha < 3$) in a three-dimensional space. If $3 < \alpha < 4$, the material shows a surface fractal behavior (the surface of the material displays fractal characteristics, but the bulk of the object does not.). Typically, the exponent $\alpha = 2$ is exhibited by Gaussian chains, discs, or sheet-like lamellar objects[164].

At the high resolution end of the SAXS pattern if the contribution to the scattering comes from the interface between two phases, the intensity drops with the fourth power of q. The power law of q^{-4} is referred to as Porod Law and is usually interpreted as originating from non-fractals with smooth interfaces (D_v=3, D_s=2).

3.2.7.3 Dynamic Mechanical Analysis (DMA)

Dynamic mechanical analysis is a technique to measure the mechanical properties of materials as a function of time, temperature and frequency. The DMA supplies an

oscillatory force to be applied to the sample. The resulting sinusoidal response to that force is analyzed. The applied force is called stress and denoted by σ. When subjected to a stress, a material exhibits a deformation or strain ε. By measuring the amplitude of the deformation and the lag between the stress and strain sine waves, quantities like modulus and damping can be calculated. In purely elastic materials, stress and strain occur in phase, so that the response of one occurs simultaneously with the other. The ratio of the stress to strain gives material's stiffness or its resistance to deformation, called modulus. Young's modulus, the slope of the initial linear portion of the stress-strain curve, is commonly used as an indicator of material performance. In purely viscous materials, there is a phase difference between stress and strain, where strain lags stress by 90°. Viscoelastic materials exhibit behavior somewhere in between that of purely viscous and purely elastic materials, showing some phase lag in between 0 and 90°. For a viscoelastic material, stress-strain relationship under a continuous sinusoidal loading is defined by its complex dynamic modulus (E^*). Stress and strain can be represented using the following expressions:

$$\text{Stress: } \sigma = \sigma_0 \sin(\omega t - \delta) \tag{3.18}$$

$$\text{Strain: } \varepsilon = \varepsilon_0 \sin(\omega t) \tag{3.19}$$

where δ is phase the lag between stress and strain.

$$E^* = \frac{\sigma}{\varepsilon} = \frac{\sigma_0 \sin(\omega t - \delta)}{\varepsilon_0 \sin(\omega t)} = E' + iE'' \tag{3.20}$$

where E' is the storage (elastic) modulus which is related to the sample's stiffness and E'' is the loss modulus (viscous component) and it is related to the sample's ability to dissipate mechanical energy through molecular motion. E' and E'' can be expressed as following:

$$E' = \frac{\sigma_0}{\varepsilon_0} \cos\delta \tag{3.21}$$

$$E'' = \frac{\sigma_0}{\varepsilon_0} \sin\delta \tag{3.22}$$

Viscoelastic materials such as polymers typically exist in two distinct states. They exhibit the properties of a glass at low temperatures and those of a rubber at higher temperatures. By scanning the temperature during a DMA experiment, this change of state, the glass transition or alpha relaxation, can be observed. The glass transition temperature (T_g) is often measured by DSC (Differential Scanning Calorimetry), but the DMA technique is more sensitive and yields more easily interpreted data. DMA can also be used to

investigate the frequency (and therefore time) dependent nature of the transition. DMA can also resolve sub-T_g transitions, like beta, gamma and delta transitions in many materials that the DSC technique is not sensitive enough to pick up.

3.2.7.4 Solid-State NMR Spectroscopy

Solid state nuclear magnetic resonance (NMR) spectroscopy is a widely used tool for studying molecular structure and dynamics[165]. When an NMR active nucleus (spin quantum number ≠ 0) of a compound is placed in a magnetic field and irradiated with electromagnetic radiation, the compound may absorb energy through a process called magnetic resonance. This absorption of energy is quantized and produces a characteristic spectrum for the compound. By using solid-state NMR spectroscopy, it is possible to get information about the full effects of anisotropic or orientation-dependent interactions, i.e., chemical shift anisotropy, dipolar and quadrupolar couplings, in solid-state. The chemical shift anisotropy and quadrupolar interactions provide insight into electronic structure and bonding, while the dipolar coupling offers direct access to internuclear distances. In media with no or little mobility, anisotropic interactions have a substantial influence on nuclear spin energy levels (and hence the resonance frequency) of all sites in a molecule, and often contribute to a line-broadening effect in NMR spectra. However, these interactions in solids can be averaged by Magic-angle spinning (MAS) technique. This technique involves rotating the sample about an axis oriented at 54.74° with respect to the external magnetic field (B_0) (Figure 3.5). In this way, broad lines become narrower, increasing the resolution for better identification and analysis of the spectrum.

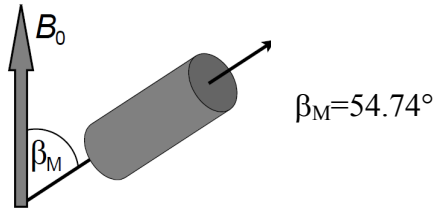

Figure 3.5: Representation of a MAS experiment.

3.3 Experimental

3.3.1 Preparation of the Membranes

Composite Nafion+10% w/w ZrO_2 (Composite 1) and recast Nafion (Recast Nafion 1) membranes were prepared according to the following procedure described by Saccà et al.[57]. Commercially available 5% w/w Nafion (*Ion Power*®) alcoholic solution was dried and re-dissolved in dimethyl acetamide (DMAc). 10% w/w ZrO_2 powder (*Aldrich*, 100-200 nm, 8% Y_2O_3 stabilized ZrO_2) was mixed with 10% w/w Nafion solution in an ultrasonic bath and then casted on a glass sheet. The solvent was evaporated by heating at 80 °C on a hot plate. The resulting membranes were detached from the glass with distilled water and treated at 155 °C for 10 min. The respective bare membrane (Recast Nafion 1) was prepared following the same procedure except inorganic oxide incorporation.

Composite Nafion+3% w/w SiO_2 (Composite 2) and recast Nafion (Recast Nafion 2) were prepared by using a procedure described by Arico et al[166]. Differently from the previous procedure, 5% w/w Nafion alcoholic solution (*Ion Power*®) was directly mixed with 3% w/w SiO_2 (*Cabot*, 7 nm) and the resulting membranes were hot pressed between PTFE foils at 160 °C for 10 min at 2 bars. The respective bare membrane (Recast Nafion 2) was prepared in the same way except addition of oxide particles.

Composite Fumion+3% w/w sZrO_2 (Composite 3) and recast Fumion were prepared in a similar way as described above. This time, 5% w/w alcoholic Fumion solution (*Fumatech*®) was dried and re-dissolved in dimethyl formamide (DMF). The prepared solution was mixed with 3% w/w sZrO_2 (*Mel Chemicals*, submicron, 5% SO_3 doped) in an ultrasonic bath. The prepared membranes were treated at 155 °C for 30 min. Recast Fumion was also prepared in the same way without adding oxides.

Commercial Nafion® 117 was included in this study for comparative purposes. All of the membranes were preconditioned by heating at 80 °C for 4 h in 10% w/w HNO_3. The excess acid was removed by keeping the membranes at 80 °C for 4 h in distilled water and washing them several times with distilled water at room temperature. Hereafter, the preconditioned membranes will be indicated as *as-received* membranes.

Thermal treatment was done by heating the preconditioned membranes at 140 °C for 4 h in vacuum oven (1000 mbar). The membranes after this procedure are named as *heat-treated* membranes. Hydrothermal treatments were done by keeping the membranes at 120 °C and 50, 30 and 10% relative humidity (RH).

3.3.2 IEC (Ion Exchange Capacity) Measurements

The amount of $-SO_3^-$ groups available for ion exchange was determined by acid-base titrimetry. The membranes were soaked in 1 M NaCl solution for 1 hour before titrating with 0.01 M NaOH (Mettler Titrator DL21). The samples (in their Na^+ form) were dried after titration in a vacuum oven at 140 °C for 4 h. IEC values were calculated by dividing the moles of protonic charge carriers by the dry weight of the membrane (mol/g). Equivalent weight (EW) of the membranes is determined by inversing IEC values.

3.3.3 Swelling

Swelling in water was determined by immersing square shaped membranes (2 cm x 2 cm) in double distilled water for 2 h between 30-150 °C with steps of 10 °C. Stainless steel autoclave was used at temperatures above 100 °C in order to prevent the water from evaporation. The liquid water on the surface of the wet membranes was removed by tissue paper before weighting and determining dimensions. The dry weight of the membranes was obtained by drying the membranes at 140 °C in a vacuum oven.

3.3.4 Water Hydration Isotherms

Water hydration isotherms were determined at room temperature under variable relative humidities. Different saturated salt solutions having different equilibrium H_2O partial pressures (Table 3.1) were placed at the bottom of a desiccator and the membranes were equilibrated inside of this desiccator for 2 days. Relative humidities (RHs) were changed from high to low and from low to high values, which resulted into somewhat different degrees of hydration. The hydration levels were determined by weighting on an external balance and comparing the weight to that of the dried membrane (T=140 °C, 4 h in vacuum).

Table 3.1: Saturated salt solutions and their relative humidity (RH) values at room temperature.

Salt	RH (%)	Salt	RH (%)
K_2SO_4	97	NaBr	59/60
KNO_3	93	$MgCl_2$	33
$BaCl_2$	90	LiCl	11
$(NH_4)_2SO_4$	81	NaOH	6
NaCl	75		

3.3.5 Ac-Impedance Spectroscopy

The ionic conductivity of the membranes were measured as a function of temperature T (range: 30–80 ^{o}C, step size of 10 °C, 15 min equilibration time for each temperature point) using ac-impedance spectroscopy in the frequency range 100–10 MHz (Hewlett Packard 4284A). The measurements were performed in a closed cell in order to keep the water content constant during the measurements. 20–30 stacked slices of each membrane with a diameter of ~4 mm were squeezed between two gold electrodes. Conductivity measurements in constant water pressure of $p_{H2O}=10^5$ Pa were carried out in a double wall temperature controlled glass chamber at temperatures between 105 and 140 °C. Note that this corresponds to a decreasing relative humidity with increasing temperature. 10–20 stacked slices of membranes with a diameter of ~6 mm were placed in a porous glass tube with a gold electrode at the bottom. The second gold electrode was pressed from the top onto the stack of membranes by a screw in order to assure optimum contact. Specific conductivities were obtained from the high-frequency intercept of the complex impedance with the real axis and the dimensions of the stacks. Proton diffusion coefficients (D_σ) were calculated from the conductivity data σ using Nernst-Einstein equation:

$$D_\sigma = \frac{RT\sigma}{F^2 c_{H^+}} \tag{3.23}$$

where c_{H^+} is the concentration of protonic charge carriers, T is the absolute temperature, F is Faraday's constant and R is the gas constant.

Another cell (Fumatech LFZ-MK3) was used in order to perform controlled temperature and relative humidity measurements. The stainless steel sealed-off cell consists of three

compartments: one part houses the sample, the other part reserves water and the third part connects these two compartments. The temperature of these three compartments can be set up to different values. The temperature of the connection part was kept higher than the sample temperature in order to avoid condensation. The RH was calculated from the ratio between water vapor pressure at the temperature of the water reservoir and the sample compartment. The membrane tangential conductivity was determined by four-probe impedance measurements in the frequency range 100–10 MHz. The membranes having ~1.5 cm width were placed on top of the four platinum wire electrodes which were placed on a Teflon disc with a distance of 1 cm in between. Subsequently, the membranes were squeezed by a second Teflon disc which has four rectangular windows allowing hydration of the membranes.

3.3.6 Attenuated Total Reflection Infrared (ATR-IR) Spectroscopy

ATR-IR spectra were measured by using a special ATR kit with a diamond crystal coupled with a Bruker IFS 66 Spectrometer and recorded with a DTGS detector at a resolution of 2 cm^{-1}. The membranes were squeezed between the surface of a diamond crystal and a pressing counterpart device in order to achieve a good contact. All measurements were derived by averaging 250 scans in the range of 4000-400 cm^{-1}.

3.3.7 X-Ray Diffraction Measurements

X-Ray diffraction studies were conducted with a PHILIPS-PW 3710 diffractometer with Cu K_α radiation source (λ=0.15, 418 nm). X-ray tube voltage and current were set at 40 kV and 30 mA, respectively. For short runs, step size was 0.02° with 1 s time difference between each step. For long run measurements, step size was 0.02° with 15 s time difference between each step. The measurements were carried out under ambient conditions between 10° and 80°. Silicon (Si) standard was used to improve the precision of the diffraction patterns.

3.3.8 Small Angle X-Ray Scattering (SAXS)

SAXS experiments were performed at the DUBBLE beam line (BM26B) at the European Synchrotron Radiation Facility (ESRF) in Grenoble (France). 2-3 stacked slices of

membranes with a total thickness of 300-500 μm were placed in between two thin Mylar sheets serving as windows and transferred into a gas tight sample holder. The data were collected using a 2D multiwire gasfilled detector with pixel array dimensions of 512 x 512. Two different sample-to-detector positions were used (1.5 and 5 m) in order to investigate a wide *q*-range. The *q*-scale was calibrated using the position of diffracted peaks from a standard silver behenate powder. The exposure time for each sample was about 60 s and a wavelength of $\lambda = 1.54$ Å was used. The experimental data were corrected for the background scattering and transformed into 1D plots by azimuthal angle integration.

3.3.9 Dynamic Mechanical Analysis (DMA)

The mechanical properties of the membranes were studied by using a dynamic mechanical analyzer DMA (TA instruments, type Q800) connected to a humidifier (Setaram, type Wetsys) as a function of temperature and relative humidity RH. In order to control RH, the sample holder was constructed (Figure 3.6) which was hermetically encapsulated[115]. The RH was measured by a Rotronic Hygroclip IC-1 humidity sensor with an accuracy of ±1%. For each measurement temperature and RH were kept constant for at least one hour. The measurements were performed by applying an oscillatory sinusoidal tensile deformation (frequency: 1Hz, amplitude: 5 μm, preload force: 0.01 N) on a rectangular film sample of approx. 20 mm x 5 mm x 0.05–0.2 mm. In order to determine α-relaxation of the ionic clusters, the membranes were heated with a rate of 3 °C/min between 40-150 °C. The mechanical response data were analyzed in terms of elastic (storage) modulus E' and viscous (loss) modulus E''. In order to investigate the effect of heat treatment on the membrane properties, storage moduli were determined as a function of temperature at a constant water pressure of p_{H2O} = 23 mbar (note that this corresponds to a decreasing relative humidity with increasing temperature).

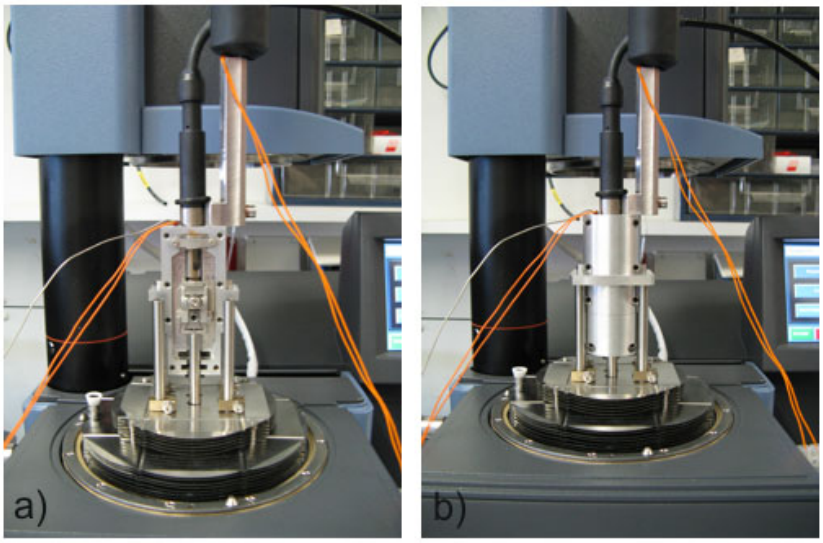

Figure 3.6: DMA sample holder constructed to perform controlled temperature and humidity measurements.

3.3.10 Solid State NMR

^{19}F solid state NMR spectroscopy was performed on a Varian InfinityPlus 400 NMR spectrometer at 376.09 MHz. The NMR spectra were acquired under MAS conditions using a 4 mm HFXY magic-angle spinning probe at a spinning frequency of 15 kHz. The acquisition parameters were as follows: the ^{19}F 90° puls length was 3 μs, the recycle delay was 2s and the dwell time was 5 μs. The ^{19}F signal of Teflon at -122 ppm was used as a secondary internal reference.

3.4 Results

3.4.1 Properties of the Membranes

Equivalent weight (EW), number of water molecules per sulfonic acid group (λ) and water volume fraction (φ) are the generally used parameters to characterize the membranes. Due to a characteristic ratio of $-SO_3H$ groups for a specific type of membrane, the respective EW is known to be constant. However, in this study EW values of the membranes are observed to increase both by keeping the membranes in deionised water at room temperature for a long period of time and upon thermal/hydrothermal treatments. The results are shown in Tables 3.2-3.5.

Depending on the time that the membranes resided in water at RT, EW and λ values of the membranes is observed to increase slightly. Water volume fractions of the membranes either stay unchanged or decrease very slightly.

All of the membranes which were heat-treated after being kept in deionised water at RT for 1-2 weeks show higher EWs, lower λ and φ values compared to the as-received membranes. Compared to all types of heat treated bare material, respective heat treated composite membranes have higher λ and φ values. Recast Nafion membranes, which are produced differently but preconditioned in the same way (described in section 3.3.1), show similar EWs, λ and φ values. However, after heat treatment Recast Nafion 1 shows a lower EW and higher λ and φ values compared to Recast Nafion 2. The Recast Fumion membrane has the lowest change in EW, λ and φ upon heat treatment compared to the other heated recast membranes. Composite 3 has a comparable EW change (upon heat-treatment) to the respective recast membrane (Recast Fumion), but it has higher amount of water. In comparison to the other composite membranes, Composite 3 has a lower EW and higher λ and φ.

A more significant EW increase, λ and φ decrease is detected for all of the membranes which were heat treated after being kept in deionised water at RT for 3-4 months. Composite 1 and Composite 2 have lower EWs compared to the respective bare membranes. All of the composite membranes have higher λ and φ values compared to the respective bare material. Recast Nafion 1 shows a lower EW and higher λ and φ compared to Recast Nafion 2. Compared to Recast Nafion 1 and Recast Nafion 2, Recast Fumion has a lower EW and higher λ and φ. The same trend is observed for the composite membranes: Composite 2 has the maximum and Composite 3 has the minimum change of EW, λ and φ after heat treatment.

The most pronounced effect upon heat treatment is observed for Nafion® 117 which was kept in deionized water at RT for approximately 2 years after preconditioning.

In addition to the above described thermal treatments, hydrothermally treated Nafion® 117 membranes (120 °C, 50, 30 and 10% RH) also show higher EWs and lower λ and φ values compared to the as-received membranes (Table 3.6).

Table 3.2: EW, λ and φ values of Nafion® 117 membranes which are after conditioning with HNO_3 kept in deionised water at RT for different periods of time and then heat treated at 140 °C for 4 hours.

	Nafion® 117 1-2 weeks			**Nafion® 117 3-4 months**			**Nafion® 117 ~ 2 years**		
	EW	**λ**	**φ**	**EW**	**λ**	**φ**	**EW**	**λ**	**φ**
Before heat treatment	1071	17.6	0.38	1105	17.4	0.37	1163	19.5	0.37
After heat treatment	1120	11.9	0.28	1233	11.9	0.27	1428	11.0	0.23

Table 3.3: EW, λ, φ values of Recast Nafion 1and Composite 1 (Nafion+10% w/w ZrO_2) which are after conditioning with HNO_3 kept in deionised water at RT for different periods of time and then heat treated at 140 °C for 4 hours.

	Recast Nafion-1 1-2 weeks			**Recast Nafion-1 3-4 months**			**Composite 1 1-2 weeks**			**Composite 1 3-4 months**		
	EW	**λ**	**φ**	**EW**	**λ**	**φ**	**EW**	**λ**	**φ**	**EW**	**λ**	**φ**
Before heat treatment	1123	21.6	0.43	1263	24.4	0.42	1163	24.5	0.44	1299	26.3	0.44
After heat treatment	1265	12.1	0.26	1517	11.9	0.23	1320	12.3	0.27	1466	13.6	0.27

Table 3.4: EW, λ, φ values of Recast Nafion 2 and Composite 2 (Nafion+3% w/w SiO_2) which are kept in deionised water at RT for different periods of time after conditioning with HNO_3.

	Recast Nafion-2 1-2 weeks			**Recast Nafion-2 3-4 months**			**Composite 2 1-2 weeks**			**Composite 2 3-4 months**		
	EW	**λ**	**φ**	**EW**	**λ**	**φ**	**EW**	**λ**	**φ**	**EW**	**λ**	**φ**
Before heat treatment	1111	22.0	0.43	1193	24.5	0.44	1075	24.5	0.46	1141	25.4	0.46
After heat treatment	1360	10.8	0.23	1724	11.3	0.20	1342	13.3	0.27	1470	14.9	0.28

Table 3. 5: EW, λ, φ values of Recast Fumion and Composite 3 (Fumion+3% w/w sZrO_2)which are heat treated at 140 °C for 4h after conditioning with HNO_3 and then kept in deionised water at RT for different periods of time.

	Recast Fumion 1-2 weeks			**Recast Fumion 3-4 months**			**Composite 3 1-2 weeks**			**Composite 3 3-4 months**		
	EW	**λ**	**φ**	**EW**	**λ**	**φ**	**EW**	**λ**	**φ**	**EW**	**λ**	**φ**
Before heat treatment	1076	30.0	0.51	1233	32.0	0.49	1056	31.2	0.55	1256	33.4	0.53
After heat treatment	1138	14.8	0.33	1310	16.0	0.32	1136	16.9	0.38	1449	17.4	0.33

Table 3. 6: EW, λ and φ values of Nafion® 117 membranes which are after conditioning with HNO_3 kept in deionised water at RT for different periods of time and then kept at 120 °C, 50 and 30% RH for 1 week and 10% RH for 2 weeks.

		EW	λ	φ
Nafion® 117 ~ 2 years	120 °C, 50% RH, 1 week	1267	11.0	0.25
Nafion® 117 3-4 months	120 °C, 30% RH, 1 week	1320	13.4	0.28
Nafion® 117 3-4 months	120 °C, 10% RH, 2 weeks	1389	11.9	0.25

In short, by the above presented results it is understood that: (1) membrane properties (EW, λ and φ) slowly change with time when the membranes are kept in water at RT; (2) membrane properties change more significantly upon thermal treatment; (3) the most pronounced change is observed if the two processes are combined (time plus thermal treatments): either the membranes were kept in water for a period of time and afterwards heat-treated, or the membranes were hydrothermally treated for a while; (4) considering time plus thermal treatments, composite membranes have lower EWs (higher charge carrier concentrations) and higher water contents compared to the respective bare membranes; (5) the effects of the treatments on the membrane properties differ significantly among differently produced recast membranes; (6) EWs, λ and φ values differ only slightly between different composites.

3.4.2 Water Hydration Isotherms

Figure 3.7 shows the room-temperature hydration isotherms of the Composite 1, Recast Nafion 1 and Nafion® 117 membranes. Adsorption properties of water vapor on the membranes are consistent with the observations reported previously[63, 167-169]. In the low vapor activity region, i.e. from 6 to 60 % RH, there is a gradual increase in the water uptake which is due to the solvation of the ions. In the high water activity region, i.e. from 70 to 100 % RH, there is a steep increase in the water uptake with water activity. In this region water fills the pores and swells the polymer. Swelling includes pressure terms due to stretching of polymer matrix. Therefore, it is related with the elastic properties of the polymer. For each isotherm, relative humidities are changed from high to low and from

low to high values, which resulted into somewhat different degrees of hydration in high water activity region. The water contents of the membranes in contact with liquid water are also given in the plot. The values are much higher than the ones obtained under saturated water vapor. This observation, known as Schroeder's Paradox, is widely investigated in literature and there is a big debate about it[119, 121, 170].

Composite 1 has a comparable isotherm to Nafion® 117 and both of them take up more water than Recast Nafion 1 in the high water activity region. In low water activity region, water uptake values of the membranes are nearly identical.

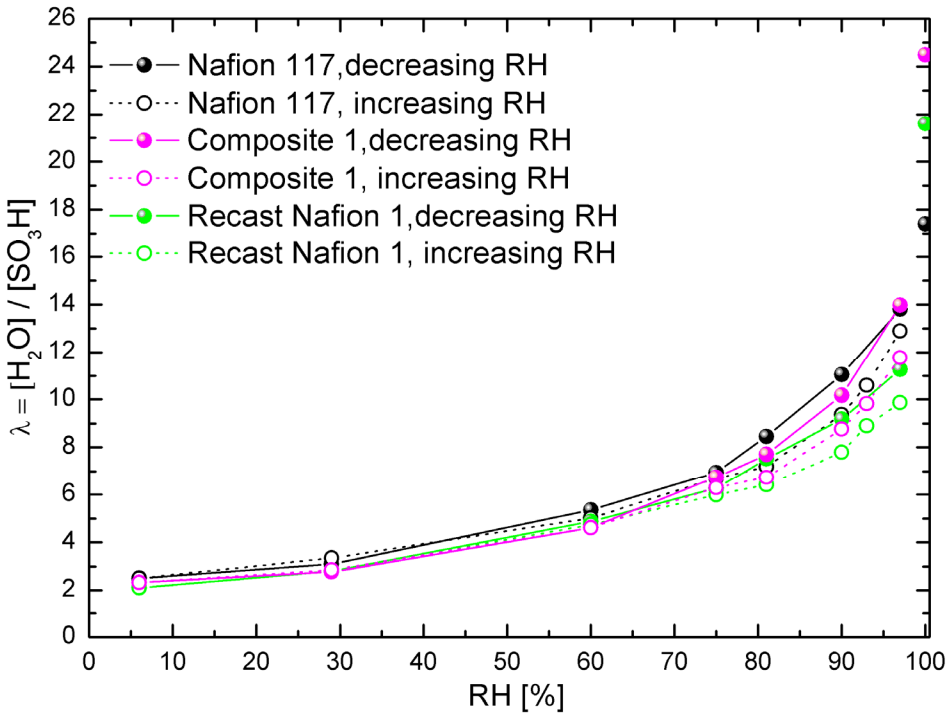

Figure 3.7: Hydration isotherms recorded at RT for Nafion® 117, Recast Nafion 1 and Composite 1.

3.4.3 Swelling

Membranes which were kept in water and heated between 90 and 130 °C, do not show significant weight or dimension change. However, above 130 °C water uptake (change in λ upon water sorption) increases significantly and therefore, weight and dimensions of the membranes change (swelling) (Figure 3.8, inset figure shows λ as a function of volume change (V/V_0) due to the swelling). Even though swelling of all of the membranes starts at

the same temperature, the extent of it varies according to the different membranes. Swelling is observed to be most pronounced for Recast Nafion 1 and least pronounced for Nafion 117.

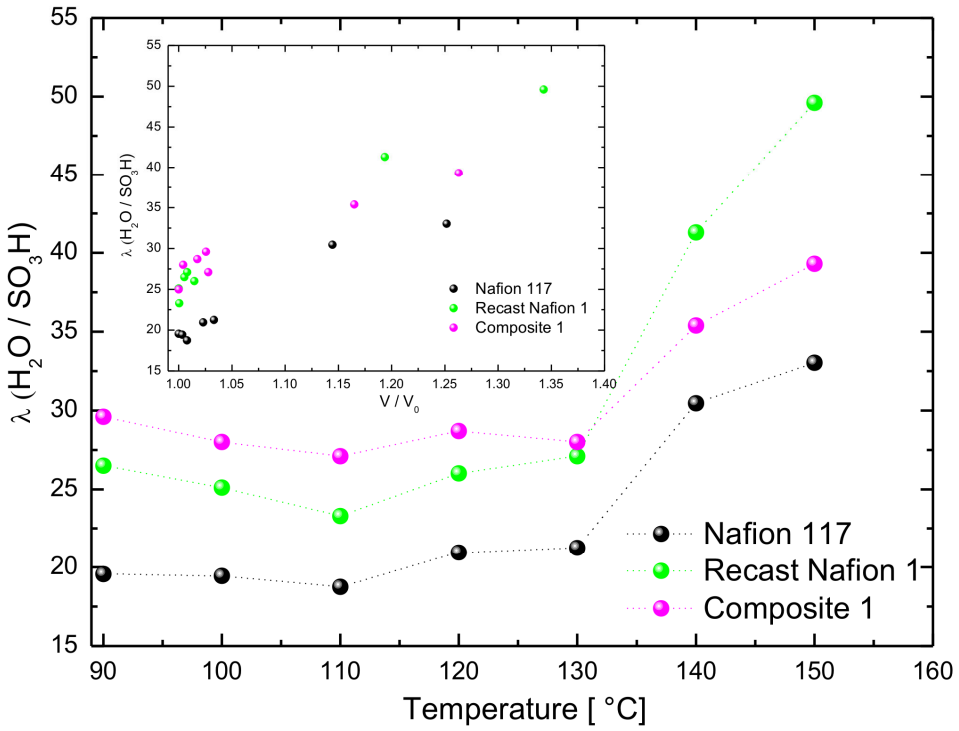

Figure 3.8: Water uptake of the Nafion® 117, Recast Nafion 1 and Composite 1 membranes as a function of temperature. Inset shows water uptake versus volume change recorded by heating the membranes in double distilled water for 2 h in the range of 90-150 °C with steps of 10 °C.

3.4.4 Proton Conductivity

Heat-treatment effect on proton conductivity is investigated systematically by performing ac-impedance spectroscopy measurements between 30-80 °C at a given λ (water content). The results shown in Figure 3.9 indicate that the proton conductivity of the heat-treated Nafion® 117 is lower than that of the as-received Nafion® 117 for a given λ. The conductivity decay due to the heat treatment at high water contents (λ ~ 16) is around 20% (EWs of the as-received and the heat-treated Nafion® 117 membranes are 1163 g/eq and 1428 g/eq, respectively). However the difference increases up to ~ 50% at low water contents (λ ~ 4) and low temperatures (T = 30 °C). Due to the fact that the temperature dependence of the proton conductivity of the heat-treated membrane is more pronounced,

the conductivity difference between as-received and heat-treated Nafion® 117 decreases with increasing temperature (at 80 °C and λ ~ 4, as-received membrane has ~ 20% higher conductivity than heat-treated membrane).

Proton conductivities of the membranes, measured between 110-140 °C at a constant water partial pressure of p_{H2O} = 10^5 Pa (1 atm) (hydrothermal treatment), are also shown in Figure 3.9. At 120 °C and 50% RH, as-received membrane has 36% higher conductivity than the heat-treated membrane. However, the difference increases with temperature (47% at 140 °C).

Activation enthalpies calculated from the temperature dependence of proton conductivity in the temperature range T = 30–80 °C as a function of λ are shown in Figure 3.10. The activation enthalpies of as-received and heat-treated Nafion® 117 are comparable with each other at high water contents (λ ~ 16). With decreasing hydration levels, activation enthalpies of the heat-treated membrane increase steeper and exceed the values of the as-received membrane.

Proton conductivity as a function of water volume fraction at T = 303 and 353 K are displayed in Figure 3.11. At T = 353 K, as-received and heat-treated Nafion® 117 membranes have quite comparable conductivities at a certain φ value. However at T = 303 K, the proton conductivity of the heat-treated membrane is slightly lower than that of the as-received membrane.

Room temperature proton conductivity diffusion coefficient D_σ values of the as-received and heat-treated Nafion® 117 membranes as a function of φ are plotted in Figure 3.12. The structure diffusion of protons, which takes place dominantly at high water contents, is suppressed at low water contents. The water diffusion coefficient also decreases with decreasing water content. As is the case for all hydrated sulfonic acid ionomers, D_σ closely follows the water diffusion coefficient, especially at low degrees of hydration, where proton transport is essentially vehicular[102]. The D_σ values of the heat-treated and as-received Nafion® 117 are very similar at φ > 0.2. However, at lower water volume fractions, heat treated membrane has slightly lower mobility.

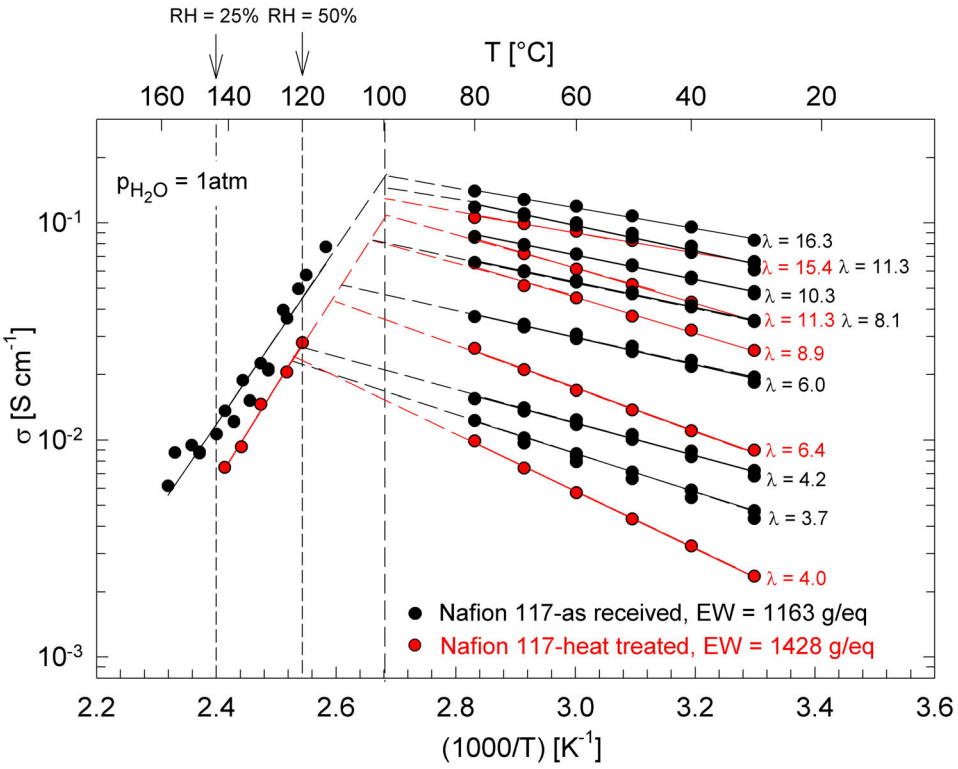

Figure 3. 9: Proton conductivities of as-received and heat-treated (140 °C, 4h in vacuum) Nafion® 117 as a function of temperature (T = 30–80 °C) for different water contents λ = [H_2O]/[-SO_3H]. Dashed lines are extrapolations to the conductivity measured at a constant water pressure of p_{H2O} = 10^5 Pa (1 atm) between T = 110–140 °C.

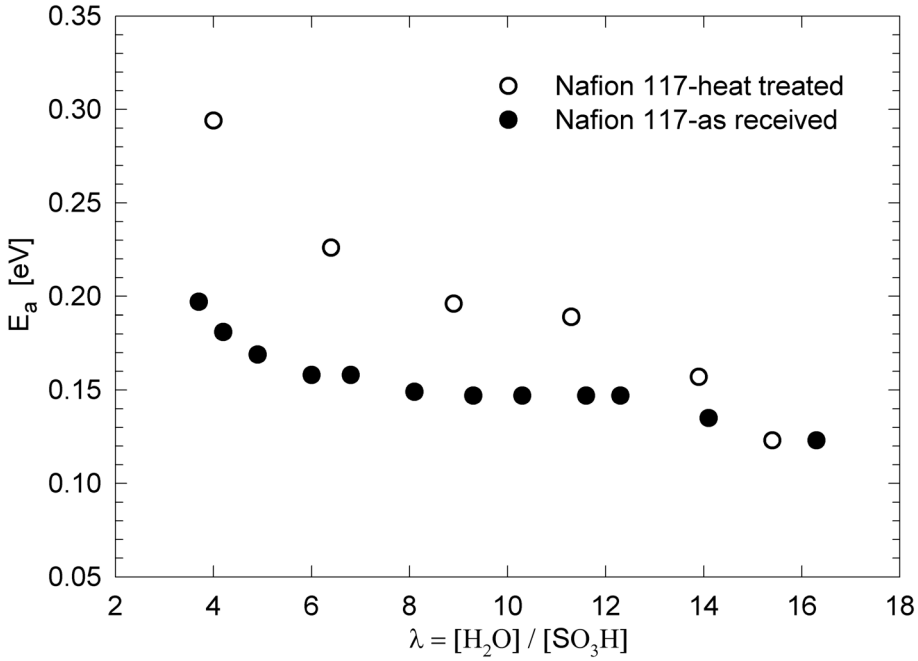

Figure 3.10: Activation enthalpies of as-received and heat-treated (140 °C, 4h in vacuum) Nafion® 117 calculated from the temperature dependence of proton conductivity in the range T = 30–80 °C for different water contents λ = [H_2O]/[-SO_3H].

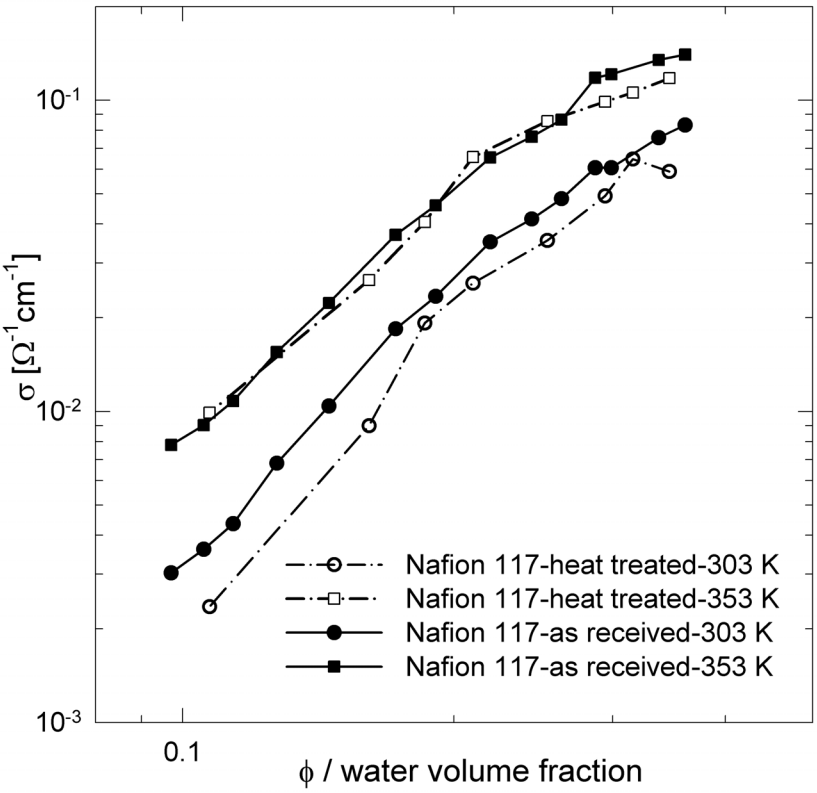

Figure 3.11: Proton conductivity values of as-received and heat-treated Nafion® 117 as a function of water volume fraction ϕ.

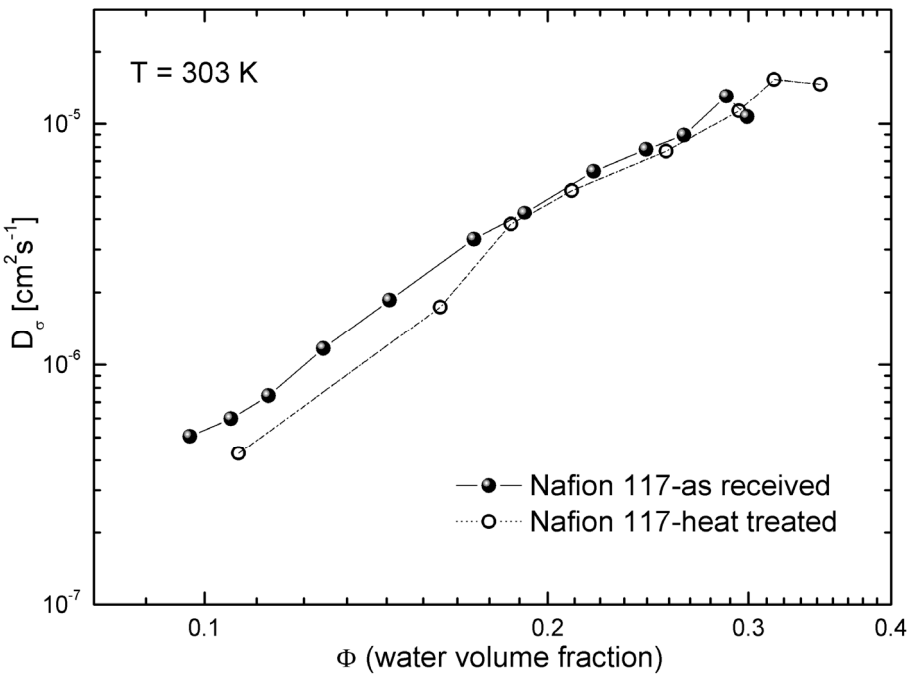

Figure 3.12: Conductivity diffusion coefficient D_σ of as-received and heat-treated Nafion® 117 as a function of water volume fraction φ.

Figure 3.13 shows Arrhenius plots of the heat-treated Composite 1 and Recast Nafion 1 membranes for different water contents. With respect to Recast Nafion 1, Composite 1 shows considerably higher proton conductivity over the whole temperature range (at a given λ value). Although EWs of the heat-treated Composite 1 and Recast Nafion 1 differ by only about 4% (EWs of the composite and the recast membrane are 1466 and 1517 g/eq, respectively), the proton conductivity difference between the membranes is significantly higher. At 30 °C and λ ~ 23, the Composite 1 membrane has 46% higher proton conductivity than the respective recast membrane. At the same temperature and lower λ values (λ ~ 4.5) the difference increases up to 90%. The results of the hydrothermal treatments are also plotted in Figure 3.13. Compared to the bare membrane, Composite 1 shows approximately 60% higher proton conductivity.

Based on the experimental results provided in Figure 3.13, activation enthalpies are calculated (Figure 3.14). At high hydration levels activation enthalpy values of all of the membranes are comparable. The temperature dependence of the conductivity (activation enthalpy) increases with decreasing λ values as it is also observed for Nafion® 117 (Figure 3.10). This increment for the heat-treated recast membrane is much severe compared to that of the heat-treated Composite 1 and Nafion® 117 membranes.

The proton conductivity and the D_σ values of heat-treated Nafion® 117 and Composite 1 are quite similar (Figures 3.15 and 3.16). On the other hand, heat-treated Recast Nafion 1 has lower proton conductivity and D_σ values than the other membranes at the same water volume fraction.

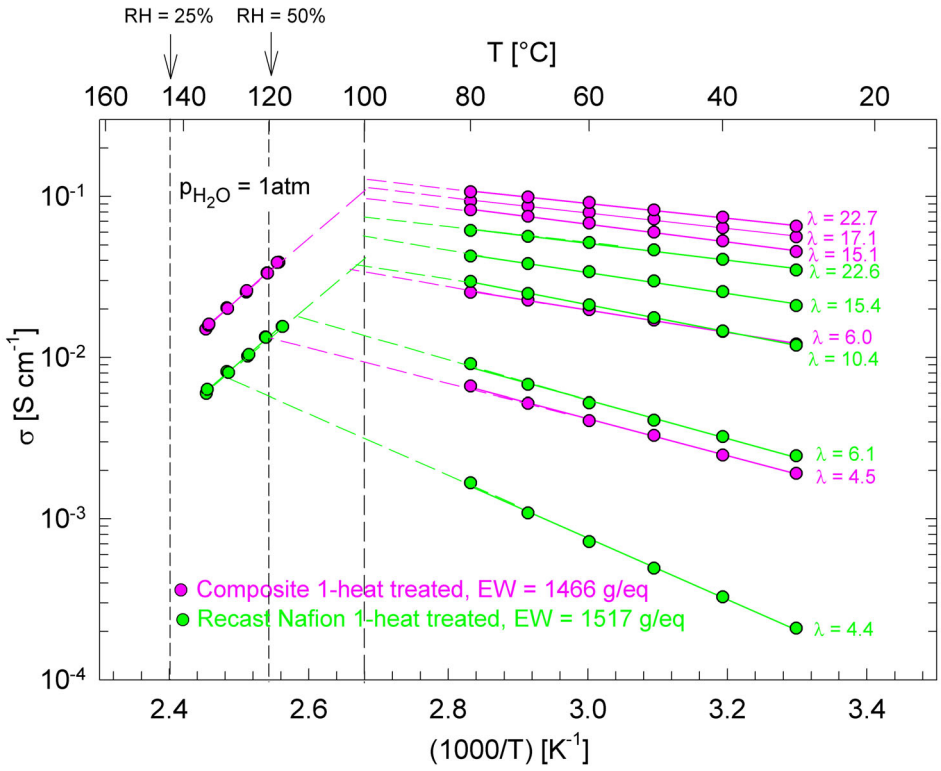

Figure 3.13: Proton conductivities of heat-treated Recast Nafion 1 and Composite 1 (Nafion+10 % w/w ZrO_2) as a function of temperature (T = 30–80 °C) for different water contents λ = [H_2O]/[-SO_3H]. Dashed lines are extrapolations to the conductivity measured at a constant water pressure of p_{H2O} = 10^5 Pa (1 atm) between T = 110–140 °C.

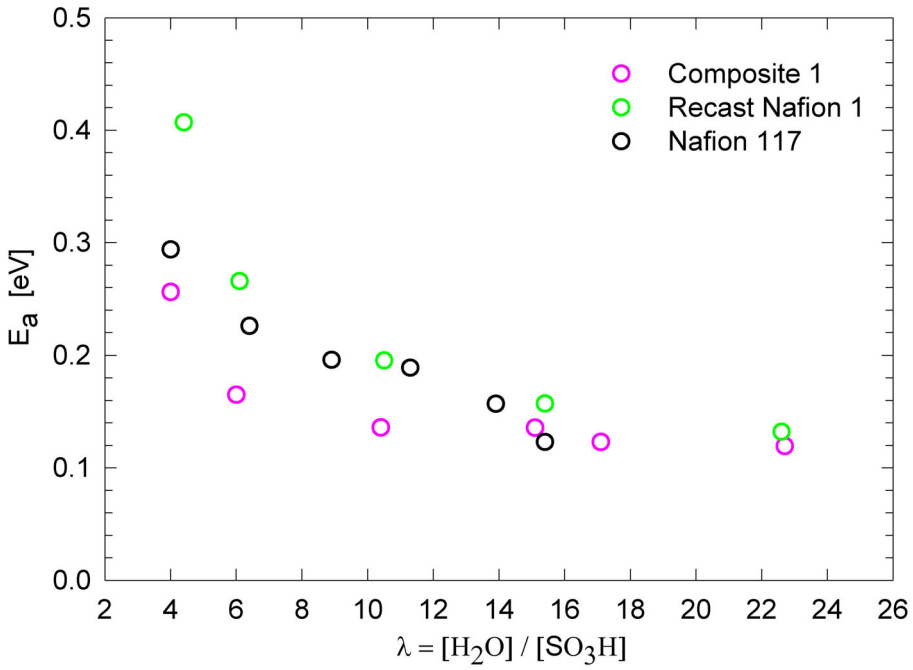

Figure 3.14: Activation enthalpy values of heat treated (140 °C, 4h in vacuum) Nafion® 117, Recast Nafion 1 and Composite 1 (Nafion+10 % w/w ZrO_2) calculated from the temperature dependence of proton conductivity in the range T = 30–80 °C for different water contents λ = [H_2O]/[-SO_3H].

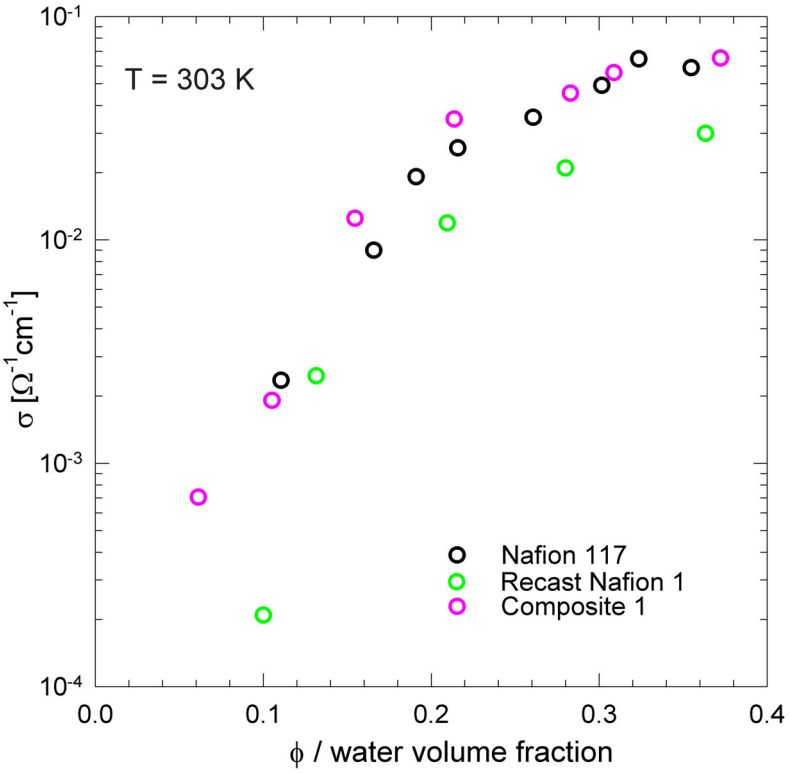

Figure 3.15: Proton conductivity of heat treated (140 °C, 4h in vacuum) Nafion® 117, Recast Nafion 1 and Composite 1 (Nafion+10 % w/w ZrO_2) as a function of water volume fraction ϕ.

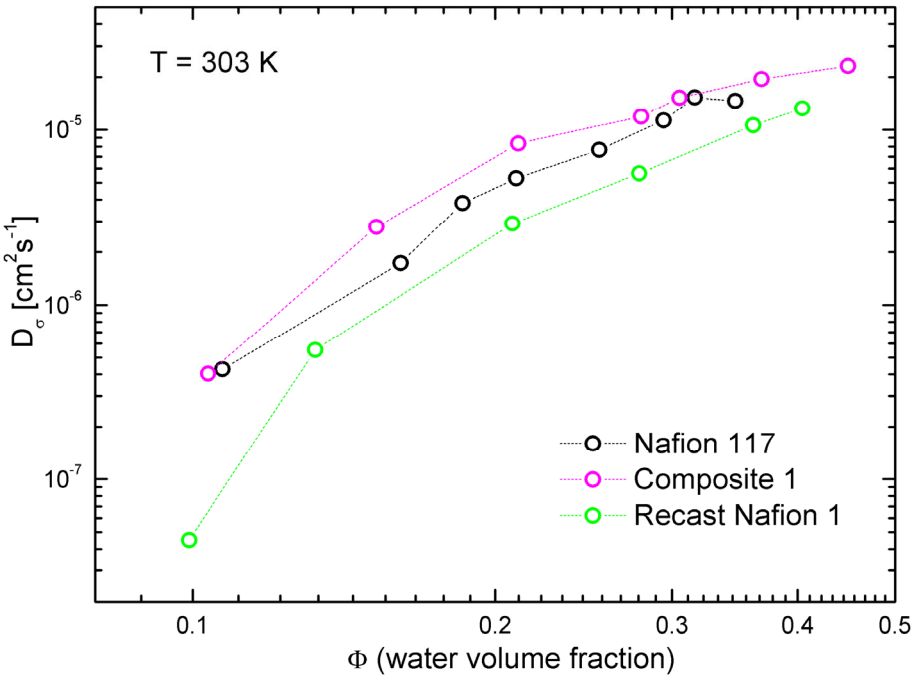

Figure 3.16: Conductivity diffusion coefficient D_σ of heat treated (140 °C, 4h in vacuum) Nafion® 117, Recast Nafion 1 and Composite 1 (Nafion+10 % w/w ZrO_2) as a function of water volume fraction φ.

The temperature and water content dependence of the proton conductivity of the as-received Recast Nafion 2-Composite 2 and Recast Fumion-Composite 3 membranes is displayed in Figure 3.17 and 3.18, respectively. Composite 2 and Composite 3 have slightly higher proton conductivity compared to the respective recast membranes at high water contents. The water content dependence of proton conductivity is less for the composite membranes. In other words, with decreasing water content the conductivity of the composites decreases less compared to the respective bare membranes. Therefore, the composites show higher conductivity at a given, low water contents. The temperature dependence of proton conductivity, on the other hand, does not differ between as-received composite and recast membranes (Figure 3.19). In Figure 3.19 the activation enthalpy values of the heat treated membranes are also given for comparison. The heat-treatment procedure leads to a strong increase in activation enthalpy (especially at low λ values) only for the membranes without oxide particles. For this reason, the heat-treated composite membranes have lower activation enthalpy values compared to the respective heat-treated bare material (especially at low λ values). At a constant water partial pressure of p_{H2O} = 10^5 Pa (1 atm) and temperatures between 110-140 °C, the proton conductivity of the composite membranes are also observed to be higher than the respective bare membranes (Figure 3.17 and 3.18). Figure 3.20 and 3.21 demonstrate that the proton conductivity and the conductivity diffusion coefficient values of the composites and the respective bare membranes are similar to each other at the same water volume fraction. However, the heat-treated membranes at low water volume fractions have lower conductivities and D_σ values compared to the as-received membranes.

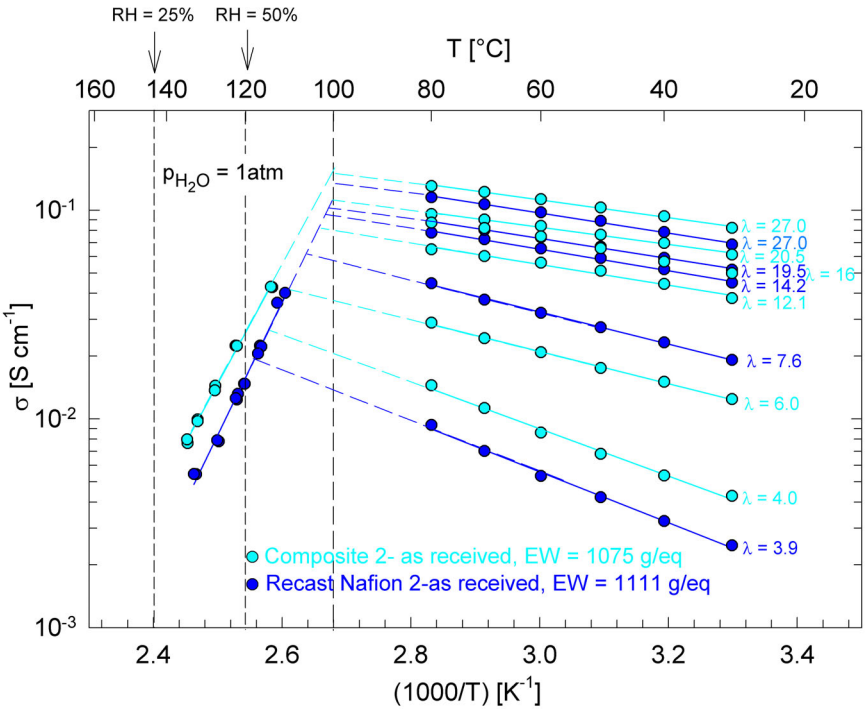

Figure 3.17: Proton conductivities of as received Recast Nafion 2 and Composite 2 (Nafion+3 % w/w SiO_2) as a function of temperature (T = 30–80 °C) for different water contents λ = [H_2O]/[-SO_3H]. Dashed lines are extrapolations to the conductivity measured at a constant water pressure of p_{H2O} = 10^5 Pa (1 atm) between T = 110–140 °C.

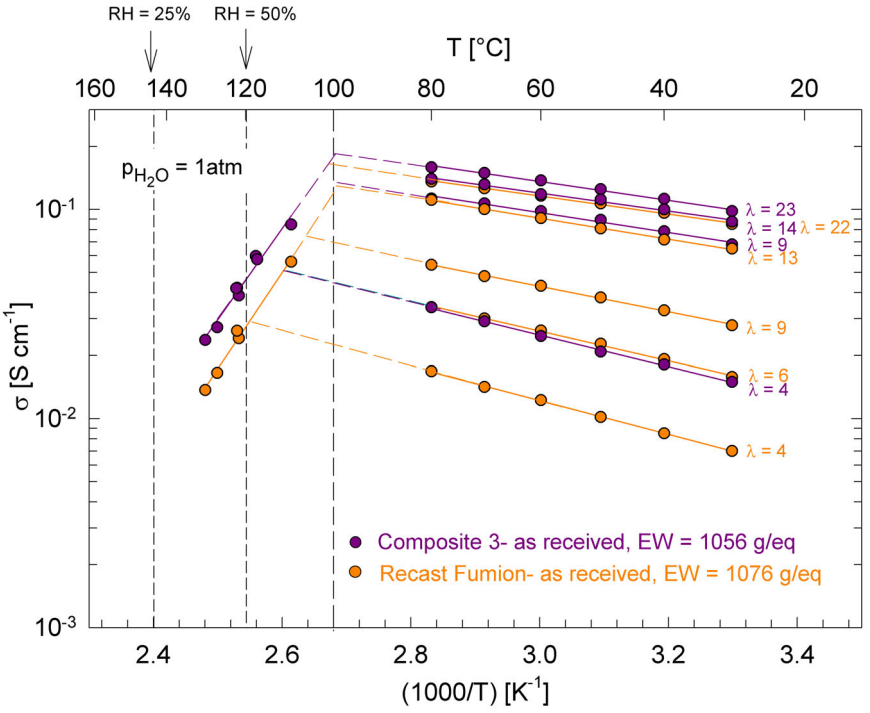

Figure 3.18: Proton conductivities of as received Recast Fumion and Composite 3 (Fumion+3 % w/w $sZrO_2$) as a function of temperature (T = 30–80 °C) for different water contents λ = [H_2O]/[-SO_3H]. Dashed lines are extrapolations to the conductivity measured at a constant water pressure of p_{H2O} = 10^5 Pa (1 atm) between T = 110–140 °C.

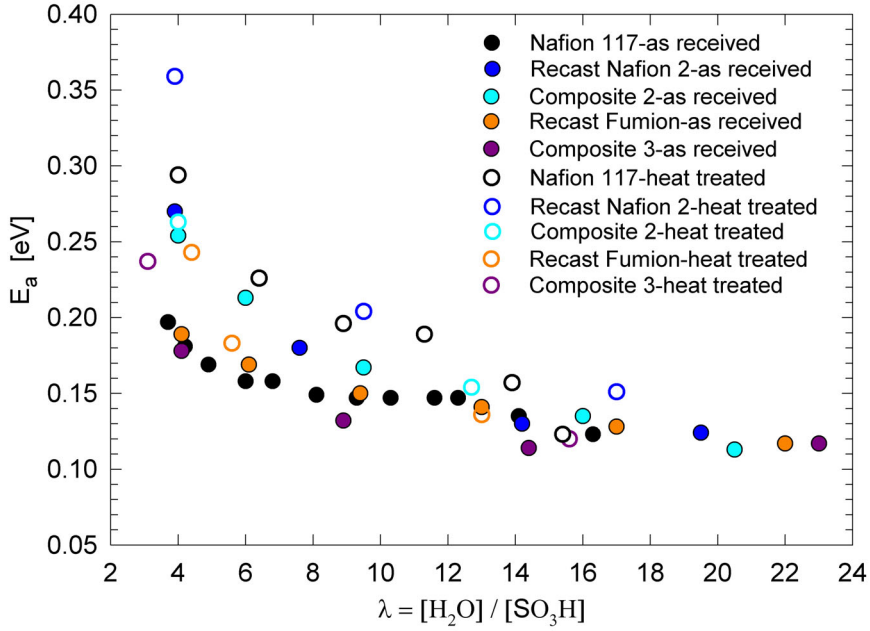

Figure 3.19: Activation enthalpy values of as-received and heat-treated (140 °C, 4h in vacuum) Nafion® 117, Recast Nafion 2, Composite 2 (Nafion+3 % w/w SiO_2), Recast Fumion and Composite 3 (Fumion+3 % w/w $sZrO_2$) calculated from the temperature dependence of proton conductivity in the range T = 30–80 °C for different water contents $\lambda = [H_2O]/[-SO_3H]$.

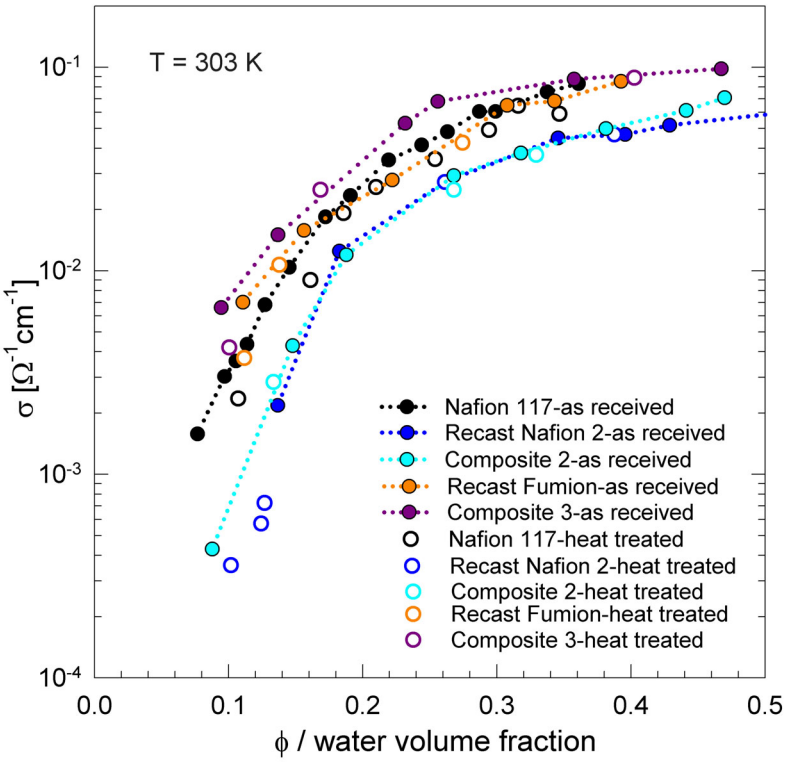

Figure 3.20: Proton conductivity values of as-received (solid symbols) and heat-treated (open symbols) Nafion® 117, Recast Nafion 2, Composite 2 (Nafion+3 % w/w SiO_2), Recast Fumion and Composite 3 (Fumion+3 % w/w $sZrO_2$) as a function of water volume fraction ϕ.

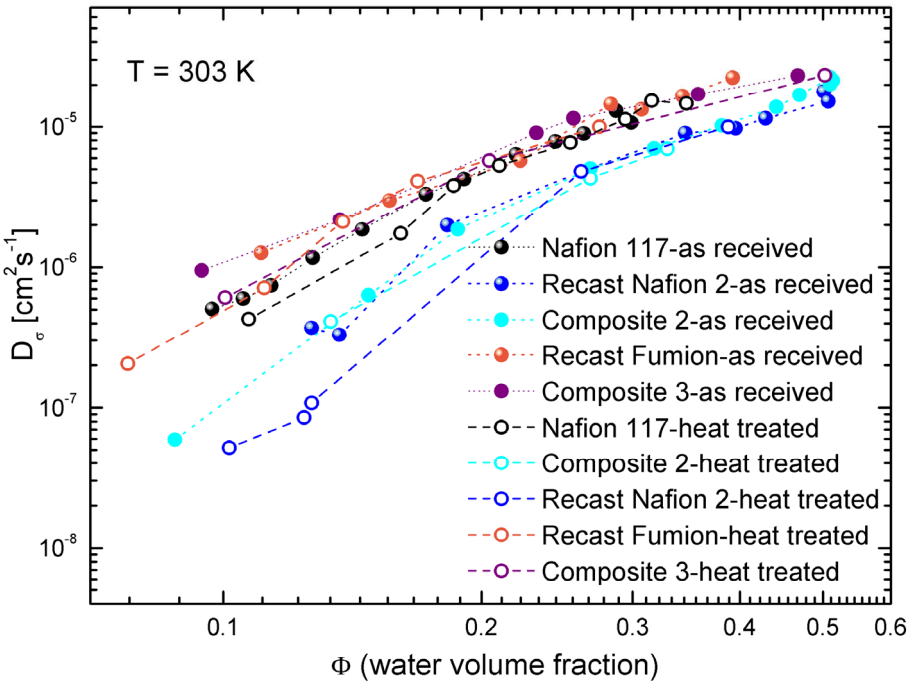

Figure 3.21: Conductivity diffusion coefficient D_σ of as-received and heat-treated (140 °C, 4h in vacuum) Nafion® 117, Recast Nafion 2, Composite 2 (Nafion+3 % w/w SiO_2), Recast Fumion and Composite 3 (Fumion+3 % w/w $sZrO_2$) as a function of water volume fraction φ.

The effects of hydrothermal treatments on the proton conductivity behavior of the Composite 1 and Recast Nafion 1 membranes are investigated in detail. The results are shown in Figure 3.22. The proton conductivity of the as-received composite membrane measured between 70 and 130 °C at a constant (30%) relative humidity (each data point was taken after 3 h of equilibration) is observed to be slightly higher than that of the respective bare membrane measured at the same conditions (shown in circles). The square symbols represent the measurements that were performed after treating the membranes at 120 °C, 30% RH for 12 hours and later on keeping in deionised water at RT for 3 days. Each data point was taken after equilibrating the membranes 12 hours at 120 °C and 30% RH. The conductivity of the composite membrane is observed to be more stable and significantly higher than the conductivity of the respective membrane upon such a treatment. After the conductivity measurements the membranes were kept in deionised water at RT for 1 month and re-measured. The results are shown in triangles. The

conductivity of the recast membrane is observed to be significantly lower than that of the composite membrane and it has a strong temperature dependence.

The circle symbols shown in inset in Figure 3.22 represent the effect of decay of relative humidity on proton conductivity behavior of the as-received membranes at a constant temperature (T = 120 °C). The conductivity of Composite 1 is slightly higher than that of the Recast Nafion 1. The conductivities were re-measured after treating the membranes at 120 °C, 30% RH for 12 hours and later on keeping in deionised water at RT for 3 days (represented in square symbols). The conductivity of the recast membrane is observed to be significantly lower than that of the composite membrane which also shows a more pronounced dependence on relative humidity.

Considering all of the observations that are described above, the results may be summarized as following: (1) thermal and hydrothermal treatments lead to a decay of the proton conductivity and an increase of the activation enthalpy at a given λ; being much more pronounced for the recast membrane compared to the respective composite and at the low water contents compared to the high water contents; (2) only at a given, low water volume fractions the proton conductivity and the mobility of the heat-treated membranes are lower compared to that of the as-received membranes; (3) the proton conductivity and the mobility of the heat-treated Composite 1 membrane are higher compared to the respective bare membrane at a given water volume fractions; (4) as-received composite membranes have slightly higher conductivities at high water contents and strongly higher conductivities at low water contents compared to the as-received bare membranes (the temperature dependence of the proton conductivity of both of the as-received composite and recast membranes are comparable); (5) a detailed investigation of the effect of hydrothermal treatments on the proton conductivity behavior shows an irreversible decay in conductivity (aging) which is less pronounced for the composite compared to the respective bare membrane.

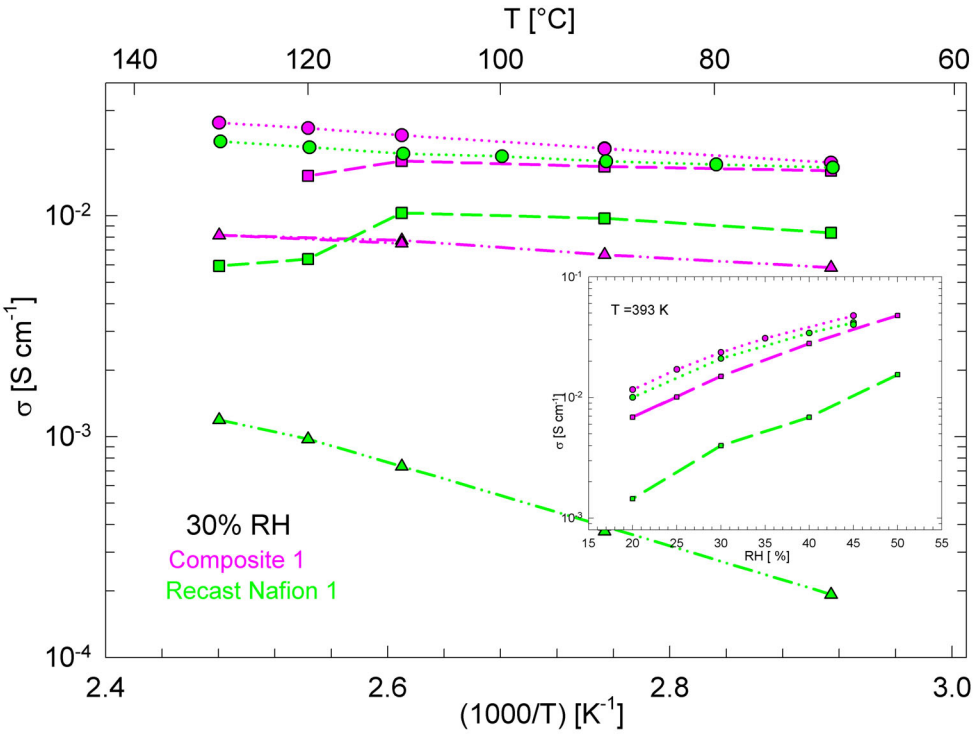

Figure 3.22: Temperature dependence of proton conductivity of as-received Recast Nafion 1 and Composite 1 at 30% RH. The inset shows the relative humidity dependence of proton conductivity at 120 °C. The circles represent the measurements performed on the as-received samples. The squares represent the measurements performed after treating the membranes at 120 °C, 30% RH for 12 hours and later on keeping in deionised water at RT for 3 days. Following this, the membranes stored in deionised water at RT for 1 month and re-measured (triangles).

3.4.5 ATR-IR Measurements

At temperatures above glass-transition temperature (T_g), side chain movement brings the $-SO_3H$ groups out of the bulk to the surface in order to decrease surface energy. Therefore, ATR is a reliable method to investigate the changes that take place on the side chains upon thermal and hydrothermal treatments.

ATR spectra of the as-received, thermally and hydrothermally treated membranes are shown in Figures 3.23-3.25. ATR spectra of the as-received membranes are consistent with the reported values in literature[50, 51, 171] and they do not differ according to the type of the membrane. Changes of the bands of Recast Nafion 1 and Composite 1 detected after heat treatment are given in Table 3.7.

The shoulder at ~667 cm^{-1} is attributed to the C-S stretching vibration[172]. The intensity of the shoulder decreases slightly after the heat treatment. The bands appear at around 930 and 1416 cm^{-1} after heat treatment can be attributed to the S-OH and S=O stretching modes of the undissociated -SO_3H groups, respectively[173, 174]. These peaks turn into shoulders again after soaking the heated membranes into water. The band at 1057 cm^{-1}, arising from symmetric stretching of the -SO_3^- ion, shifts to slightly lower wavenumbers (1052 cm^{-1}) after heat treatment. The broad band at 1718 cm^{-1} associated with the bending vibrations of hydrated oxonium ions[173] becomes sharper and shifts to lower wavenumbers. Two new bands at 1459 and 1497 cm^{-1} appear upon thermal treatment.

The above explained observations are also observed for the hydrothermally treated membranes (the membranes are cycled between 110-180 °C at p_{H2O} = 1 atm or kept at 120 °C, 10% RH for 2 weeks) except the bands appear at 1459 and 1497 cm^{-1}. Instead, a broad band at around 1440 cm^{-1} is detected.

Table 3.7: ATR-IR band assignments of as-received and heat-treated Composite 1 and Recast Nafion 1.

	Recast Nafion 1 as-received	**Composite 1 as-received**	**Recast Nafion 1 heated**	**Composite 1 heated**
ν [C-S]	667 cm^{-1} (sh)	667 cm^{-1}(sh)	667 cm^{-1}	667 cm^{-1}
ν_s [S-OH]	-	-	928 cm^{-1}	930 cm^{-1}
ν_s [S-O] of $-SO_3^-$	1057 cm^{-1}	1057 cm^{-1}	1052 cm^{-1}	1052 cm^{-1}
ν_s [CF_2]	1202 cm^{-1}	1202 cm^{-1}	1205 cm^{-1}	1205 cm^{-1}
ν_s [C-F]	1300 cm^{-1}(sh)	1300 cm^{-1}(sh)	1304 cm^{-1}	1304 cm^{-1}
ν_s [S-OH]	-	-	1416 cm^{-1}	1416 cm^{-1}
ν_{as} [SO_2]	-	-	1459 cm^{-1}	1459 cm^{-1}
ν_{as} [SO_2]	-	-	1497 cm^{-1}	1497 cm^{-1}
δ [O-H] (H_3O^+.$[H_2O]_n$)	1718 cm^{-1}(b)	1718 cm^{-1}(b)	1700 cm^{-1}	1700 cm^{-1}

v, stretching; δ, bending; as, antisymmetric mode; s, symmetric mode; b, broad; sh, shoulder.

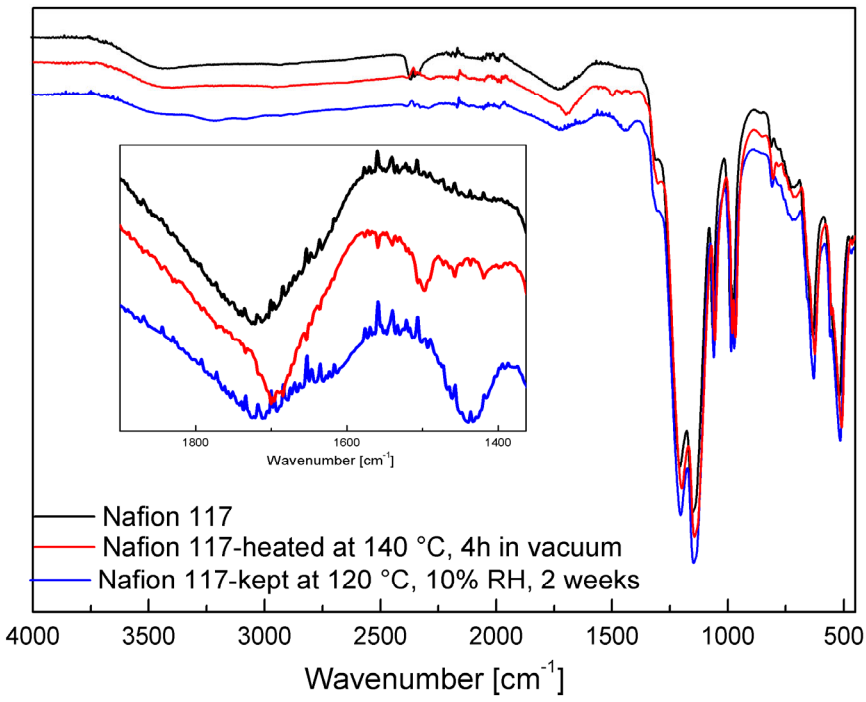

Figure 3.23: ATR-IR spectra of the as-received, thermally and hydrothermally treated Nafion® 117 membranes.

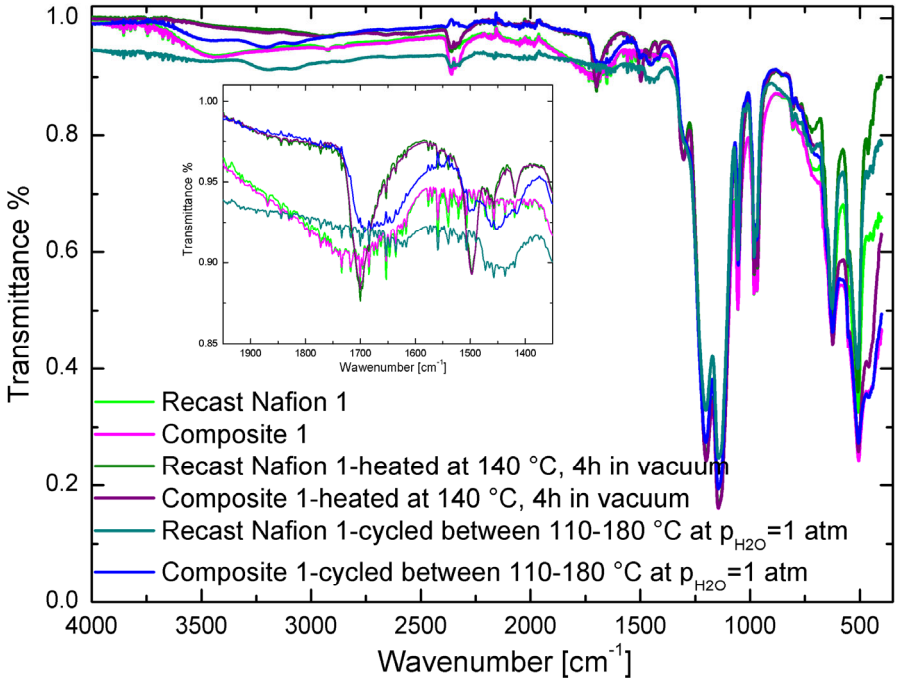

Figure 3.24: ATR-IR spectra of the as-received, thermally and hydrothermally treated Recast Nafion 1 and Composite 1 (Nafion+10 % w/w ZrO_2) membranes.

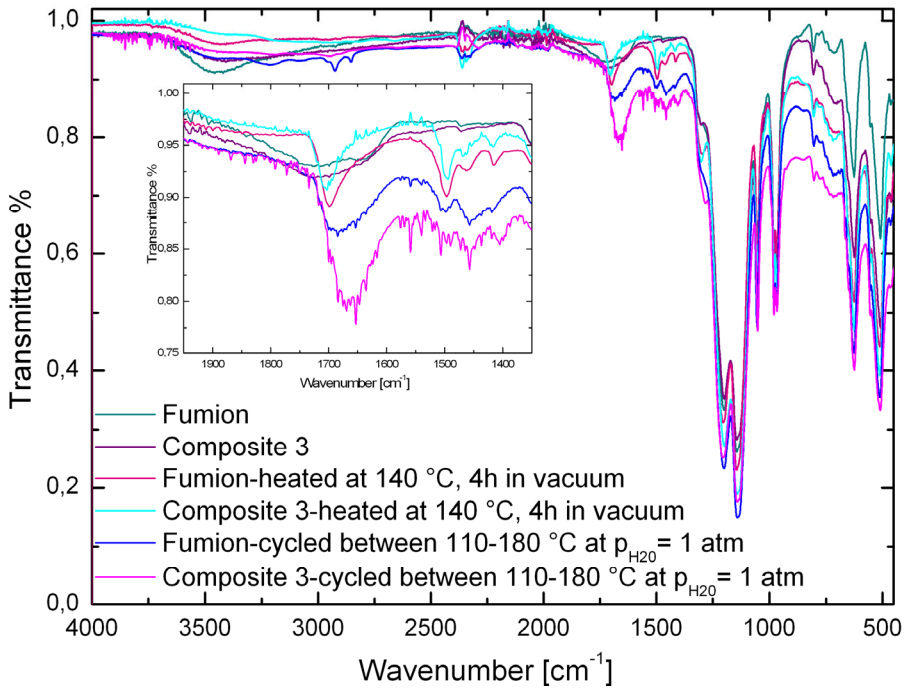

Figure 3.25: ATR-IR spectra of the as-received, thermally and hydrothermally treated Recast Fumion and Composite 3 (Fumion+3 % w/w sZrO$_2$) membranes.

3.4.6 Small-angle X-ray Scattering (SAXS)

Small-angle X-ray scattering (SAXS) is used to investigate the microstructural changes occurring in the membranes upon thermal and hydrothermal treatments. A detailed knowledge of the ionomer morphology is important since it determines the network connectivity of the membrane and strongly influences its conductivity and mechanical performance.

For Nafion membranes, the heterogeneities result from the phase separation of perfluoro-backbone crystalline structures, perfluoro-backbone amorphous domains, and ionic side chain aggregations. The ionomer peak is basically formed due to the difference between the electron density of similarly sized hydrated clusters of sulfonic acid terminated side chains and that of the perfluorocarbon matrix. The ionomer peak which in turn represents the average interionic cluster distance depends on the water content of the membranes. As the size of the hydrophilic domains increases, the scattering maximum shifts to smaller q values due to the increased contrast between hydrophilic and hydrophobic regions in the

polymer. Conversely, as the cluster size decreases, the ionomer peak shifts to higher q values[175]. The scattering maximum at smaller angles, which is named matrix knee/peak, is attributed to the distance between crystalline parts of the polymer[175].

The general shape of the scattering curves of Nafion® 117 for different water contents (Figure 3.26) are consistent with the data given in ref.[175]. As the water content in the membrane decreases, both the ionomer and matrix peaks shift to higher q values and the intensity of the matrix peak increases[175]. Same kind of behavior is observed with the membranes which are thermally and hydrothermally treated (Figures 3.27 and 3.28). If the scattering curve of the heat-treated and humidified Nafion® 117 ($\lambda = 12$) is compared with that of as-received Nafion® 117 ($\lambda = 2$) which was dried at RT, one observes that the matrix peak positions are identical ($q \sim 0.05$ A^{-1}). However, the ionomer peaks appear at different positions as expected (due to different water contents in the membranes).

In Figure 3.27 it is shown that the ionomer peak positions of heat-treated Composite 1 and Nafion® 117 are nearly identical (~ 0.14 A^{-1}) and the peak appears at lower q compared to the heat-treated Recast Nafion 1 (~ 0.19 A^{-1}). The matrix peak of Recast Nafion 1 is at higher q values (~ 0.071 A^{-1}) compared to the one of Nafion® 117. Contrary to the heat-treated Nafion® 117 and Recast Nafion 1 membranes, the matrix peak of Composite 1 has a quite small intensity.

The origin of the small angle upturn at low q is attributed to long-range heterogeneities in electron density caused by an inhomogeneous distribution of the aggregates. Compared to the respective recast Nafion and Nafion® 117, the composite membrane shows steeper negative upturn in the scattered intensity which is shifted to greater q values ($q = 0.012$ A^{-1}, d = 52 nm).

The effects of hydrothermal treatments on microstructure of the membranes are demonstrated in Figure 3.28. Although the ionomer peak position of all of the membranes is nearly the same, the matrix peak of Recast Nafion 1 appears at greater q values (~ 0.068 A^{-1}) compared to that of Nafion® 117 (~ 0.053 A^{-1}).

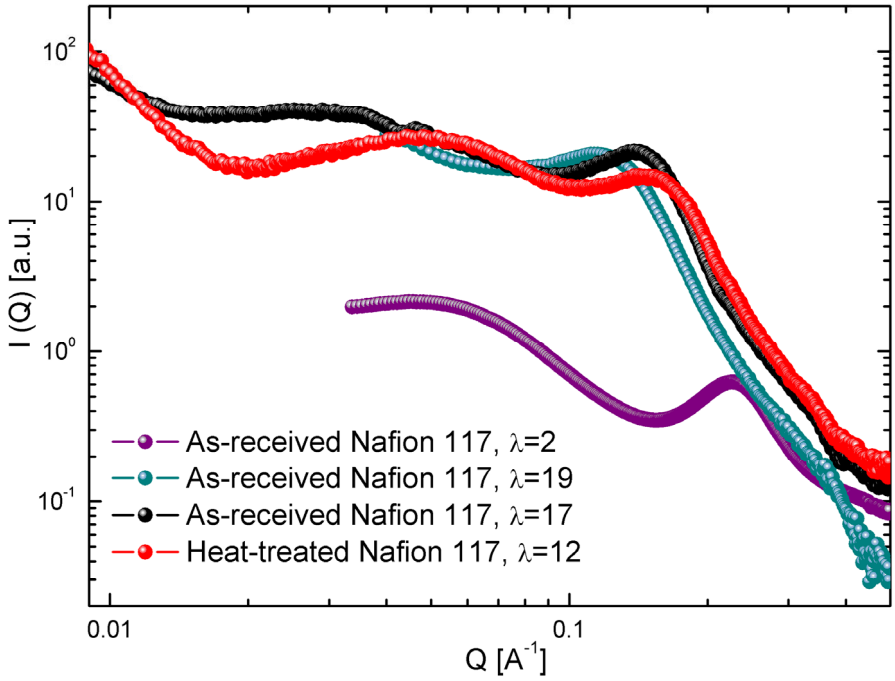

Figure 3.26: log-log representation of SAXS curves of as-received and heat-treated Nafion® 117 with different water uptakes.

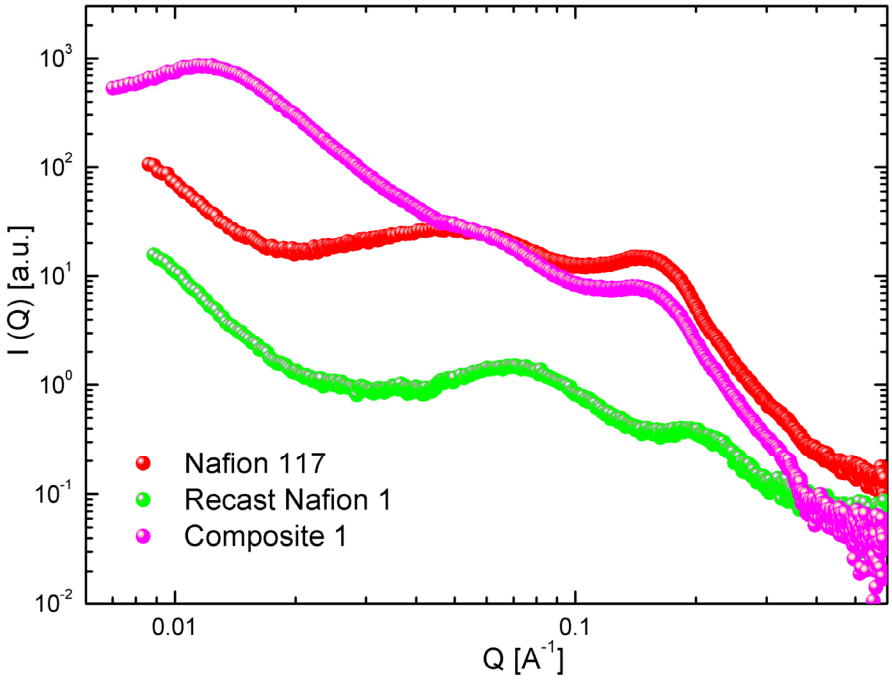

Figure 3.27: log-log representation of SAXS curves of heat-treated Nafion® 117, Recast Nafion 1 and Composite 1 (Nafion+10 % w/w ZrO_2) λ values of all of the membranes are around 12.

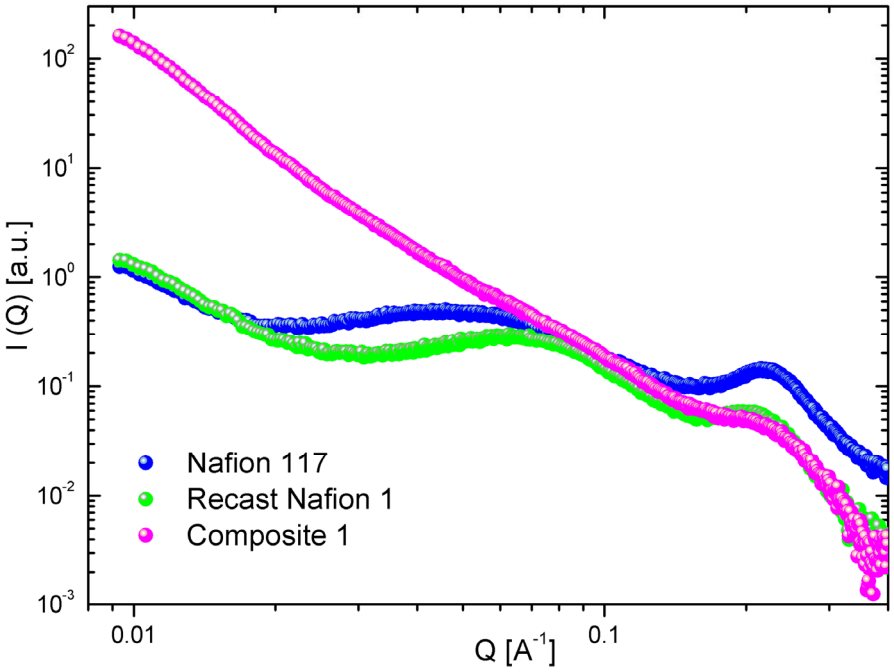

Figure 3.28: log-log representation of SAXS curves of hydrothermally treated (120 °C, 30% RH, 1 week) Nafion® 117 (λ = 3.5), Recast Nafion 1 (λ = 6.1) and Composite 1 (Nafion+10 % w/w ZrO_2) (λ = 2.1).

The above presented results can be summarized as follows: (1) thermal and hydrothermal treatments affect the microstructure of Nafion® 117 more strongly compared to the room temperature drying procedure; (2) the matrix peaks of the membranes are affected more by the thermal/hydrothermal treatments compared to the ionomer peaks; (3) the composite membrane hardly displays a matrix peak but it shows a steeper and enhanced small angle upturn at low *q* values.

3.4.7 XRD Measurements

In agreement with Moore and Martin[176], Fujimura[177] and Gierke[126], Nafion® samples display a broad diffraction feature at 2θ = 10-25° which can be deconvoluted into two peaks. The broad peak at approximately 2θ = 15.5° assigned to a diffraction maximum associated with amorphous regions and the sharp peak at approximately 2θ = 17.5° is attributed to the crystalline perfluorinated backbone regions of the membranes.

It has been observed that an increase of the annealing temperature (from 80 to 250 °C) results in a sharpening of the Bragg peak[178, 179]. Both bare and composite membranes show this characteristic peak, which becomes sharper upon the heat treatment. The composite membrane shows additional peaks scattering from ZrO_2 particles which is present in tetragonal (JCPDS data no. 81-1544) and monoclinic (JCPDS data no. 88-2390) phases. The peaks of the internal standard (Si) (JCPDS data no. 27-1402), which was added on the top of the membranes in order to permit a correction for systematic errors, are also seen in both diffraction profiles. In the pattern of the heat-treated Recast Nafion 1, there is a broad shoulder appearing at around $2\theta = 23^{\circ}$ (Figure 3.29). However, this shoulder is not present in the X-ray profile of the heat-treated composite membrane.

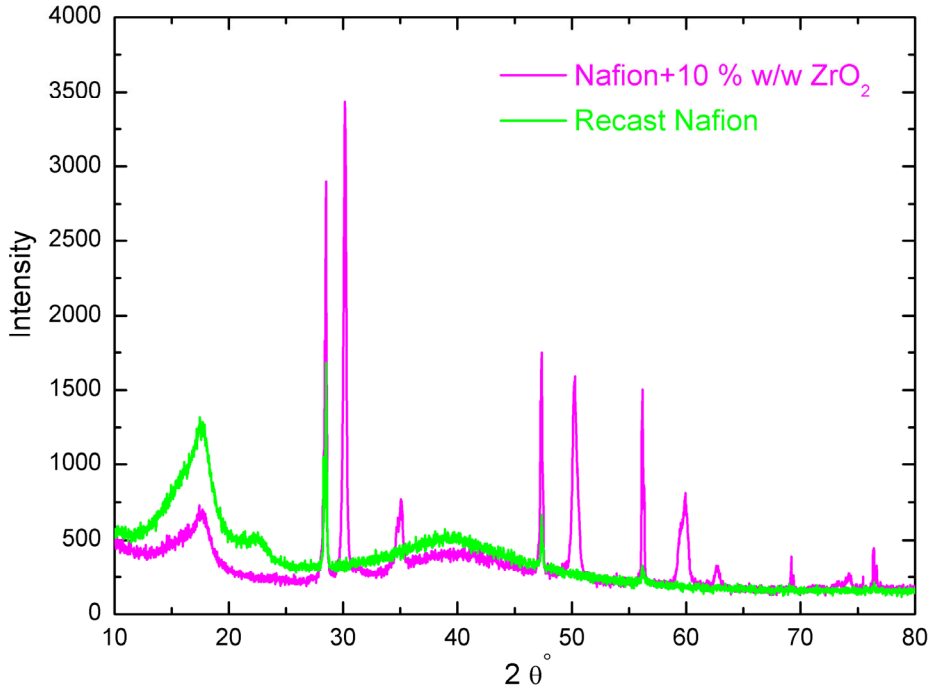

Figure 3.29: X-ray diffraction profiles of heat treated Recast Nafion 1 and Composite 1 (Nafion+10 % w/w ZrO_2).

3.4.8 Dynamic mechanical analysis (DMA)

In order to investigate the effect of inorganic particles on the structural relaxation of Nafion®, tan δ (E''/E') is analyzed as a function of the temperature in the presence and absence of humidity. Figure 3.30 shows that a relaxation takes place at 97 °C for Recast

Nafion 1 which can be attributed to motions in the cluster aggregates of side chains (α-relaxation of the ionic clusters which is close to the glass-transition temperature (T_g)) [50, 180]. For the Composite 1 membrane, α-relaxation is observed at 111 °C. Tan δ values which are determined at 15% RH are also given in Figure 3.30. At constant RH, tan δ increases slower and makes a maximum at higher temperatures. Upon annealing, glass-transition temperature of the Recast Nafion 1 and Composite 1 membranes increase from 97 to 107 °C and 111 to 119 °C, respectively (Figure 3.31). The same tendency is observed for Nafion® 117; T_g increases from 107 to 115 °C upon heat treatment (Figure 3.31). T_g values of the other membranes are determined in the same way. Composite 2 and Recast Nafion 2 show α-relaxations at 111 °C and 103 °C, respectively (Figure 3.32). On the other hand, Recast Fumion has a higher glass transition temperature (101 °C) compared to the Composite 3 (94 °C) membrane (Figure 3.33).

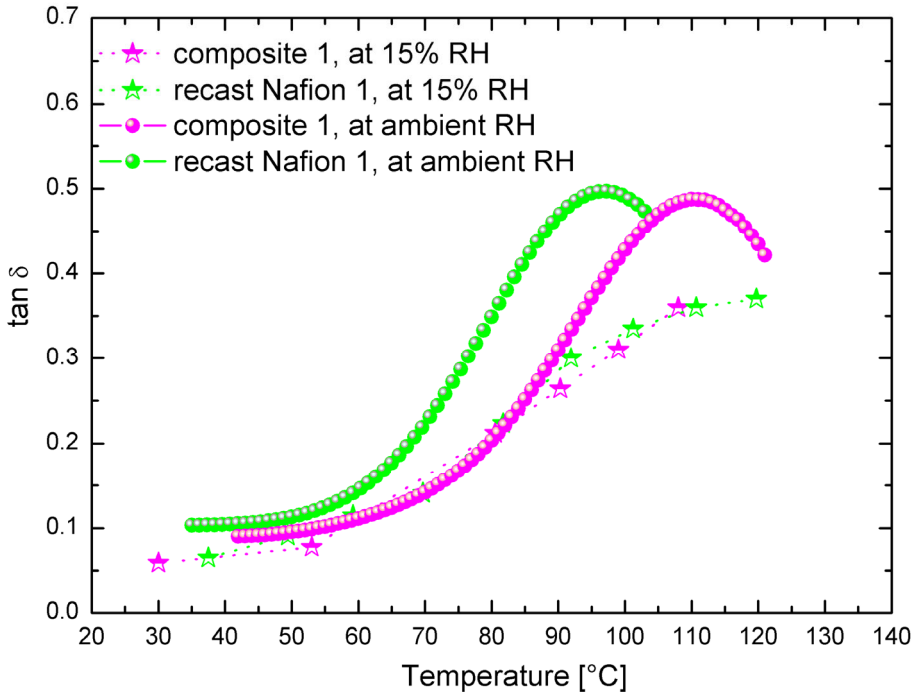

Figure 3.30: Tan δ as a function of temperature for the as-received Recast Nafion 1 and Composite 1 (Nafion+10 % w/w ZrO_2) membranes. The data shown with the solid circles is taken at ambient RH. Note that this corresponds to a decreasing relative humidity with increasing temperature.

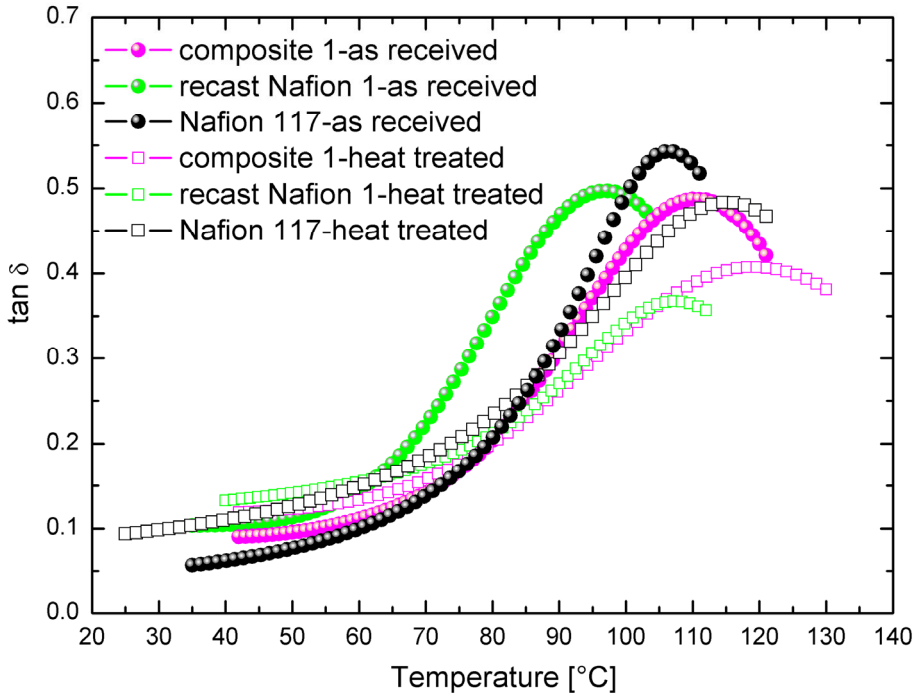

Figure 3.31: Tan δ as a function of temperature for the as-received (solid symbols) and heat-treated (open symbols) Nafion® 117, Recast Nafion and Nafion+10 % w/w ZrO_2 membranes at ambient RH. Note that this corresponds to a decreasing relative humidity with increasing temperature.

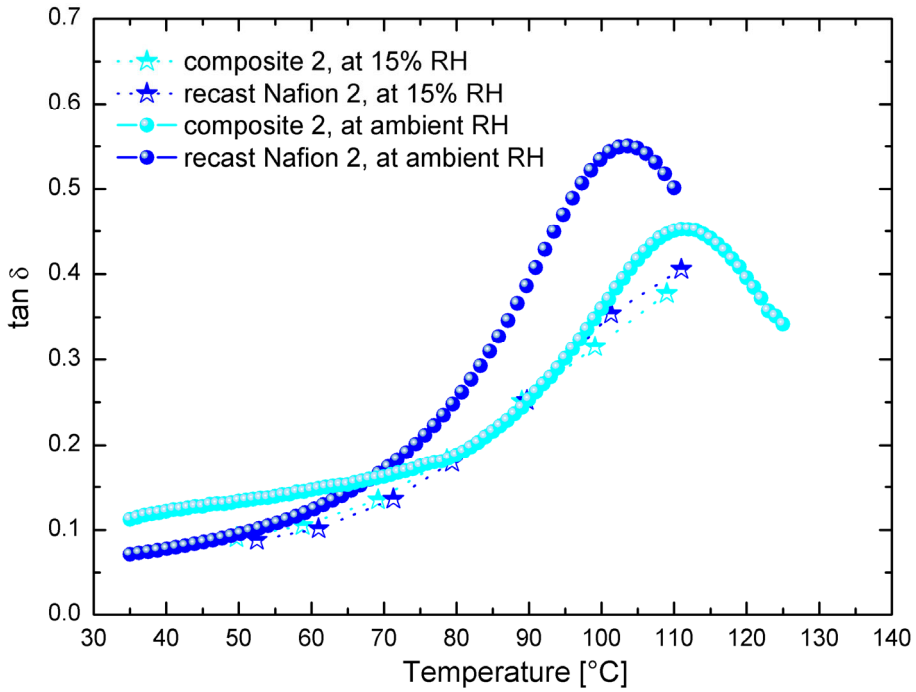

Figure 3.32: Tan δ as a function of temperature for the as-received Recast Nafion 2 and Composite 2 (Nafion+3 % w/w SiO_2) membranes. The data shown with the solid circles is taken at ambient RH. This corresponds to a decreasing relative humidity with increasing temperature.

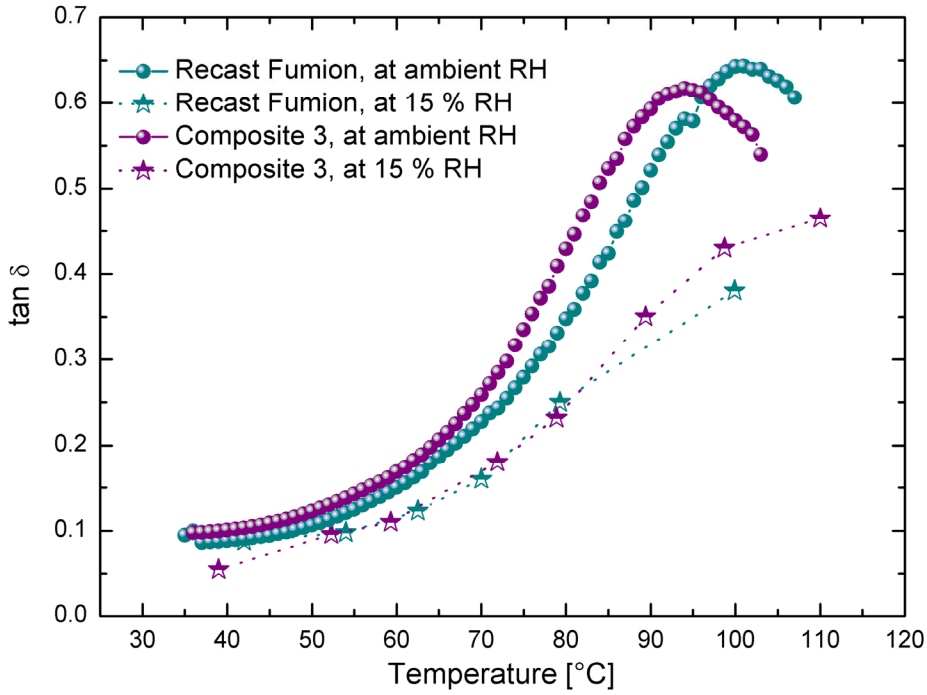

Figure 3.33: Tan δ as a function of temperature for the as-received Recast Fumion and Composite 3 (Fumion+3 % w/w $sZrO_2$) membranes. The data shown with the solid circles is taken at ambient RH. This corresponds to a decreasing relative humidity with increasing temperature.

Mechanical properties of the Nafion membranes are greatly affected by both temperature and hydration. To analyze the effect of inorganic oxide particles on dynamic mechanical properties of Nafion®, DMA measurements were performed in the temperature range from 40 to 120 °C at different RH levels (15, 30, 50 and 70%). As shown in Figure 3.34-3.37, elastic (storage) modulus E' decreases with increasing humidity and temperature. At low temperatures the effect of RH on storage modulus is quite remarkable. In this region, water acts like a softener and the stiffness of the membranes decreases with increasing relative humidity. The Composite 1 membrane exhibits higher storage moduli compared to the respective recast membrane over the whole temperature and humidity range (Figure 3.35). The storage moduli of the Composite 1 membrane decay more significantly with increasing water activity compared to the Recast Nafion 1 membrane. The decay of storage moduli with increasing temperature is less pronounced at high RHs compared to the low RHs. In other words, the measurements performed at high humidity levels show less temperature dependence of storage moduli. Therefore, the storage moduli values which are

obtained at different RHs approach each other with increasing temperature. Indeed, the storage moduli of the membranes seems to be independent of RH at a specific temperature which is about 90 °C for Composite 1 and Nafion® 117 and 80 °C for the Recast Nafion 1 membrane. The difference of 10 °C shows that the composite looses mechanical stiffness at higher temperatures compared to the respective bare membrane. Above these temperatures, storage moduli measured at 30% RH are observed to be slightly higher than the ones measured at 15% RH.

Recast Nafion 2 shows higher storage moduli compared to Composite 2 at temperatures between 30-80 °C (Figure 3.36). Since Composite 2 has only 3% w/w SiO_2, the stiffening effect of the oxide particles is not pronounced and can be compensated by the softening effect of water. At ~ 80 °C, storage moduli of the recast and composite membranes approach each other and above 80 °C, the storage moduli of Composite 2 exceed the moduli of Recast Nafion 2 (Figure 3.36).

A similar behavior is observed for the Composite 3 and the respective bare membrane (Figure 3.37). Above 80 °C and 15 and 30% RH, Composite 3 has slightly higher storage moduli and compared to the bare material without inorganic oxide particles.

The results of the heat treatment effect on the mechanical properties of the membranes are shown in Figure 3.38 and 3.39. Heat treatment has a positive effect on mechanical properties at low temperatures. However, with increasing temperature (decreasing RH) stiffness of the heat-treated membranes decreases steeper compared to the as-received membrane. Therefore, the difference between them gets smaller. The membranes loose their rigidity at around 90 °C. Heat treated Composite 1 and Nafion® 117 membranes have similar storage moduli which are slightly higher than the respective storage moduli of Recast Nafion 1.

In short, it is observed by DMA measurements that: (1) all of the composite membranes show about 10 °C higher T_g compared to the respective bare membranes; (2) T_g of all of the membranes increase by about 10 °C upon heat treatment; (3) at constant RH tan δ increases less steeply and makes a maximum at higher temperatures; (4) (i) storage moduli of the membranes decrease with increasing humidity and temperature; (ii) above a critical temperature (~ 80 °C) storage moduli keep decaying with temperature increase but start

increasing with humidity increase (the temperature dependence of storage moduli is less pronounced at high humidities); (5) Composite 1, which contains the highest amount of oxide particles (10% w/w) among all of the composites, shows higher storage moduli compared to the respective recast membrane over the whole temperature and humidity range; (6) storage moduli of the other composites exceed the values of the respective recast membranes only at high temperature and low humidities; (7) the effect of heat treatment on the mechanical properties of the membranes is more remarkable at low temperatures compared to the high temperatures.

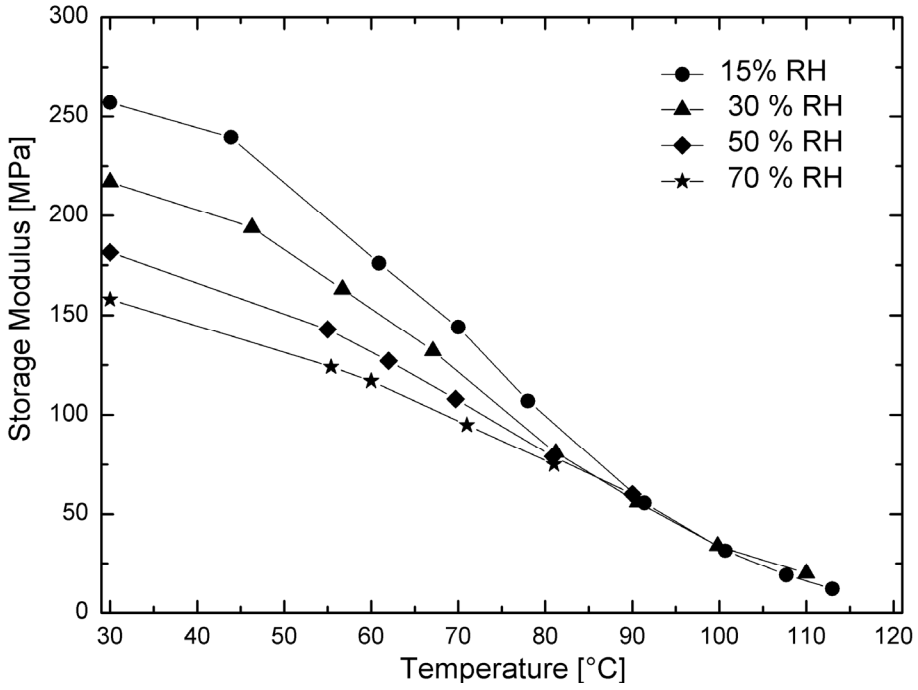

Figure 3.34: Storage moduli of Nafion® 117 versus temperature at different RHs.

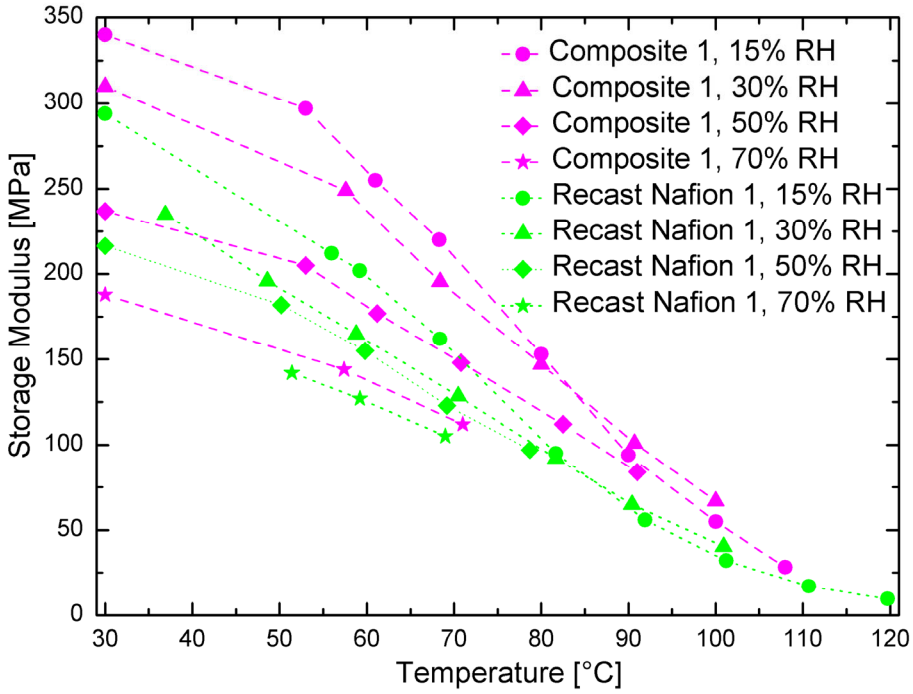

Figure 3.35: Storage moduli of Recast Nafion 1 and Composite 1 (Nafion+10 % w/w ZrO_2) versus temperature at different RHs.

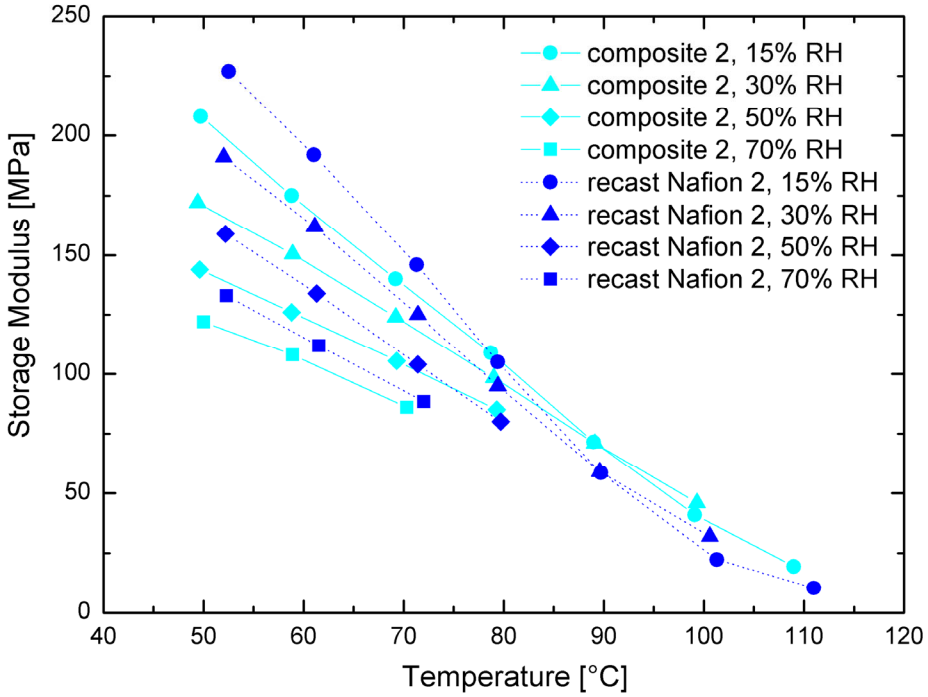

Figure 3.36: Storage moduli of Recast Nafion 2 and Composite 2 (Nafion+3 % w/w SiO_2) versus temperature at different RHs.

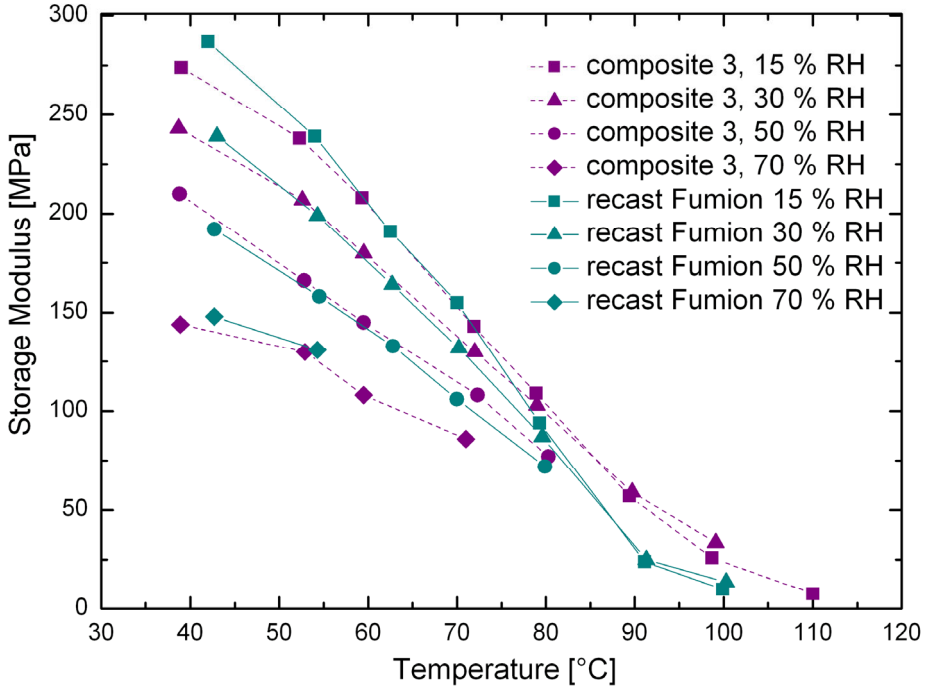

Figure 3.37: Storage moduli of Recast Fumion and Composite 3 (Fumion+3 % w/w $sZrO_2$) versus temperature at different RHs.

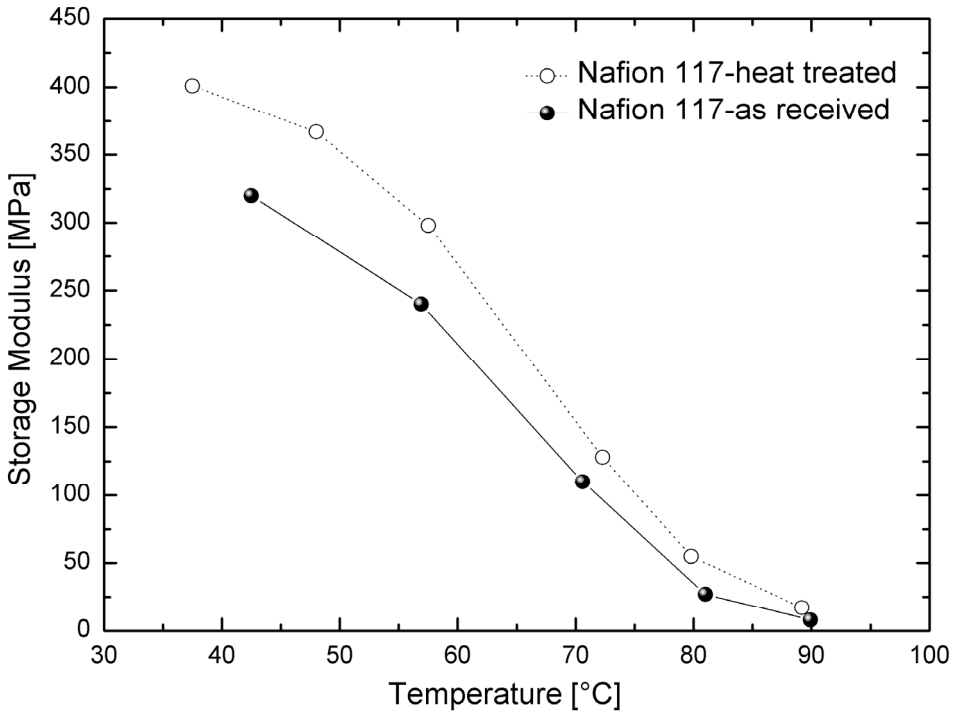

Figure 3.38: Storage moduli of as-received and heat-treated Nafion® 117 versus temperature. Measurements were performed at a constant water pressure of p_{H2O} = 23 mbar (note that this corresponds to a decreasing relative humidity with increasing temperature).

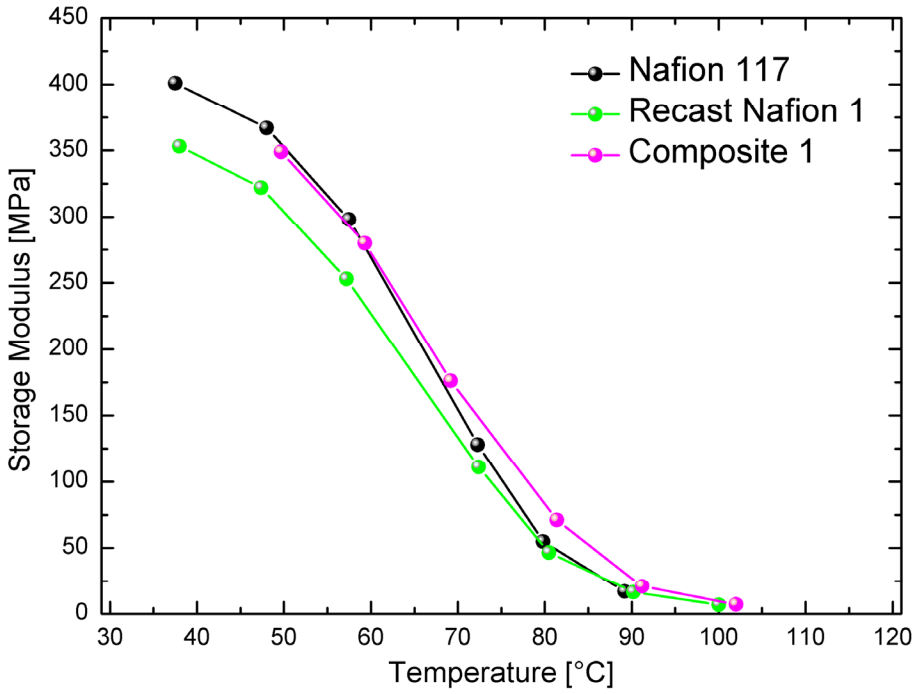

Figure 3.39: Storage moduli of heat-treated Nafion® 117, Recast Nafion 1 and Composite 1 (Nafion+10 % w/w ZrO_2) versus temperature. Measurements were performed at a constant water pressure of p_{H2O} = 23 mbar (note that this corresponds to a decreasing relative humidity with increasing temperature).

3.4.9 Solid-state Nuclear Magnetic Resonance (NMR)

^{19}F resonances of the membranes are assigned on the basis of the previous study of Chen and Schmidt-Rohr[181]. The CF_2 groups of the polymer backbone give rise to the strong peak at -122 ppm. The signals at -138 and -142 ppm are attributed to the CF signals of the main chain and side group, respectively. The ^{19}F resonance at -117 ppm reflects the SCF_2 groups. The OCF_2 and CF_3 groups appear at -80 ppm.

The ^{19}F spectra of the as-received and heat-treated membranes are shown in Figure 3.40 and 3.41. The band intensities decrease after heat treatment. However, at the same time, line broadening is observed. Line broadening of the bands (especially SCF_2 band) in the dry state is less pronounced for the composite compared to the respective recast Nafion and Nafion® 117 membranes (Figure 3.40 and 3.41).

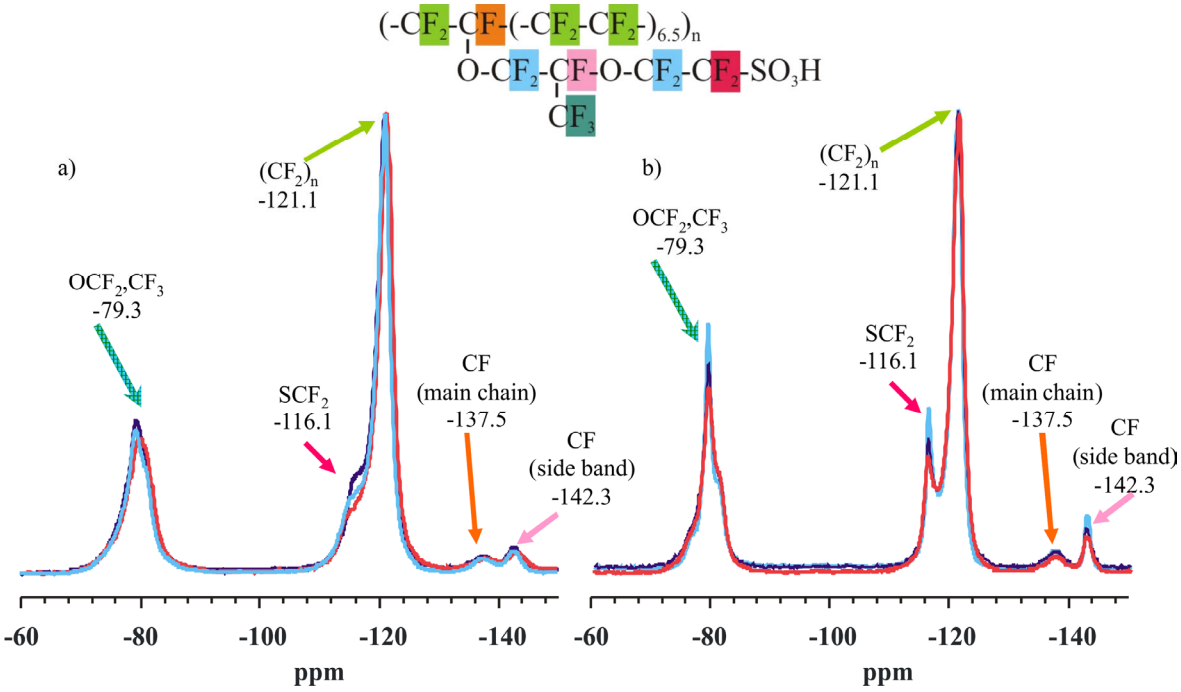

Figure 3.40: ^{19}F spectra of (a) heat-treated; (b) as-received membranes. Colors are assigned as following: Nafion® 117 (blue), Recast Nafion 1 (red) and Composite 1 (Nafion+10 % w/w ZrO_2) (violet).

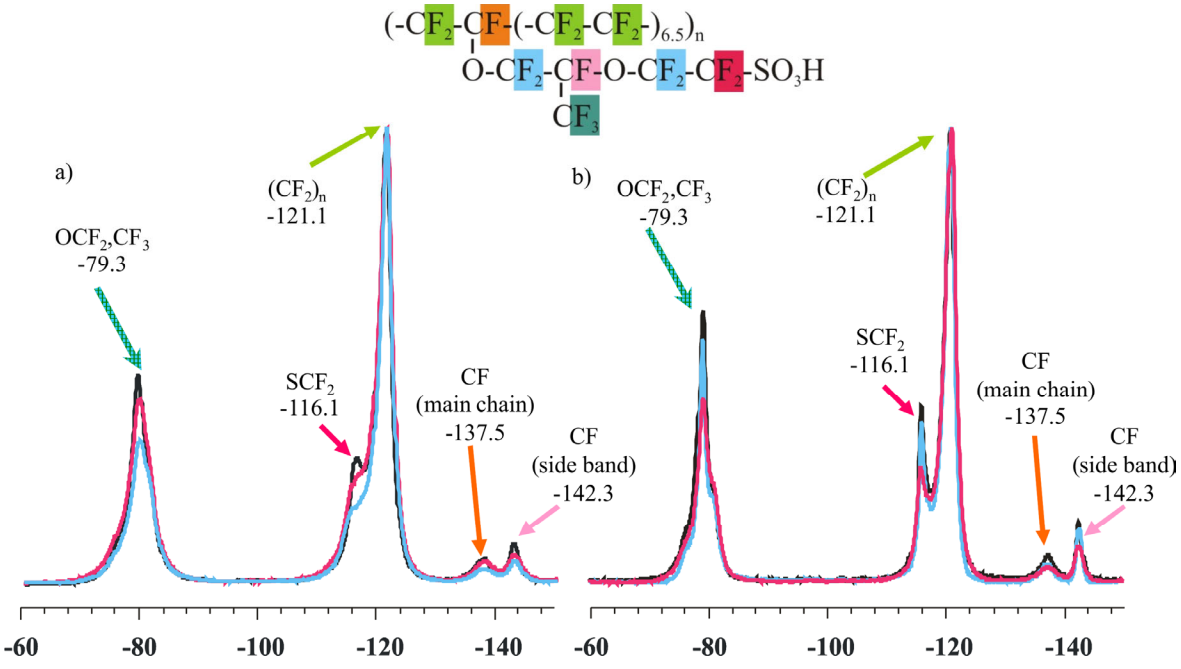

Figure 3.41: ^{19}F solid state NMR spectra of (a) heat-treated; (b) as-received membranes. Colors are assigned as following: Nafion® 117 (blue), Recast Fumion (red) and Composite 3 (Nafion+3 % w/w sZrO_2) (black).

3.5 Discussion

In the ATR-IR spectra bands appear at around 930 cm^{-1} and 1416 cm^{-1} upon heat treatment (Figures 3.23-3.25), which are attributed to the S-OH and S=O stretching modes of the undissociated -SO_3H groups, respectively[173, 174], indicate that the ionised sulfonate groups transform into the –SO_3H form (decreased dissociation). The band at 1057 cm^{-1} arising from symmetric stretching of the -SO_3^- ion shifts to slightly lower wavenumbers (1052 cm^{-1}) after heat treatment, indicating dehydration of the ion-rich regions. The broad band at 1718 cm^{-1} associated with the bending vibrations of hydrated oxonium ions[173] becomes sharper and shifts to lower wavenumbers probably due to dehydration.

Gramstadt et al. observed a doublet for trifluoromethanesulfonic acid anhydride ($(CF_3.SO_2)_2O$) at 1470 and 1459 cm^{-1}[182] and assigned them to the asymmetric SO_2 stretching vibrations. Therefore, the observed peaks at 1459 cm^{-1} and 1497 cm^{-1} upon thermal treatment can be attributed to the asymmetric SO_2 stretching vibrations of a sulfonic acid anhydride group (R-O_2S-O-SO_2-R). It is not possible to observe the symmetric stretching band of SO_2 which appears at 1131 cm^{-1} since this region is obscured by the intense band of CF_2 symmetric stretching. Asymmetric and symmetric bands of S-O-S appear at 810 and 730 cm^{-1}, respectively[183]. However, C-C and C-F stretching bands also appear at the same region which makes it difficult to assign the bands.

In literature it is reported that, after treating Nafion® 117 with hydrogen peroxide, a broad peak appears at around 1440 cm^{-1}. The peak is attributed to the formed S-O-S bond sequence[184, 185]. Recently, no degradation of the Nafion® membrane from exposure to $^{\cdot}OH$ radicals generated from hydrogen peroxide is detected[186]. Condensation products are also reported to occur after exposing the membranes to 80 °C, 80 and 0% RH for a long period of time in the absence of hydrogen peroxide[187]. In this work it is also observed that a broad band appears at around 1440 cm^{-1} upon hydrothermal treatment (the membranes are cycled between 110-180 °C at p_{H2O} = 1 atm or kept at 120 °C, 10% RH for 2 weeks). This indicates that the condensation reaction may also take place at high temperature and low humidifications.

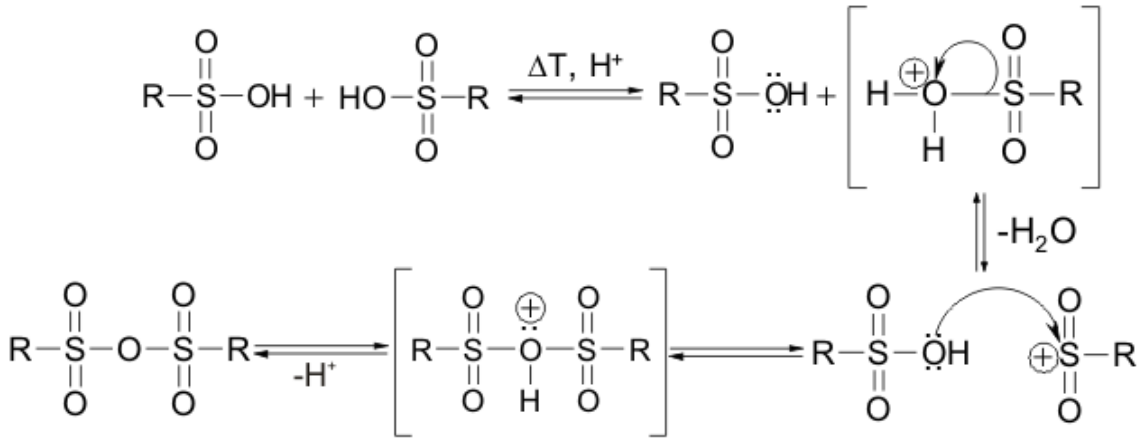

Figure 3.42: Schematic representation of a condensation reaction (anhydride formation).

Beside the process of a condensation reaction (anhydride formation), a small amount of sulfur may also form. Sulphurous acid (H_2SO_3) is a weak dibasic acid which is unknown in the isolated form. In water it can be stabilized due to a partial deprotonation. When it is heated at 150 °C in a sealed tube, H_2SO_4 forms and sulphur (S) deposits according to the following disproportionation:

$$3H_2SO_3 \xrightarrow{\Delta T} 2H_2SO_4 + H_2O + S$$

In a partial decomposition reaction of the polymer, via an intermediate SO_2 release, sulphurous acid may form:

$$R\text{-}CF_2\text{-}SO_3H \rightleftharpoons SO_2 + R\text{-}\ CF_2\text{-}OH$$

$$SO_2 + H_2O \rightleftharpoons H_2SO_3 \rightleftharpoons\ HSO_3^- + H^+$$

Due to the heat treatment that is performed in this work at 140 °C, an analogous reaction may take place. In the presence of H_2SO_4, a substituted product of $H_2S_3O_{10}$ (as present in oleum) may form.

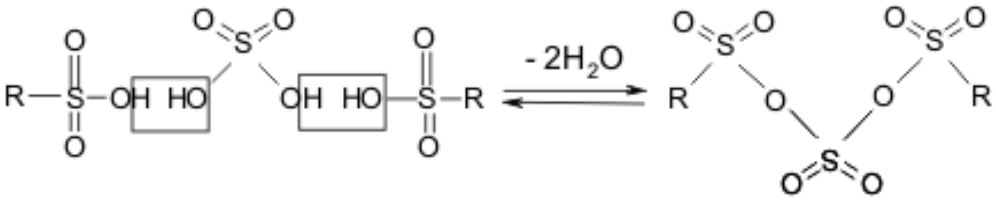

Figure 3.43: Schematic representation of a condensation reaction in the presence of H_2SO_4.

The peaks that appear in the ATR-IR spectra upon heat treatment (Figures 3.23-3.25) might be due to the formation of such condensation products. Furthermore, a slight intensity decay of the shoulder at ~667 cm^{-1} upon heat treatment indicates that the C-S bond might be partially broken. In the X-ray pattern of the heat treated Recast Nafion 1, there is a broad shoulder appearing at around $2\theta = 23^{\circ}$ (Figure 3.29) which can be due to the orthorhombic sulfur (JCPDS data no. 85-0799) that is formed upon heat treatment. Since this shoulder is not present in the X-ray profile of the heat treated composite membrane, sulfur formation probably does not take place for the composite upon heat treatment. The heat-treated bare recast membrane was also washed with deionized water, which was afterwards vaporized, in order to characterize the residue. Trace amounts of residue were investigated with EDX (Energy dispersive X-ray spectroscopy) and the results reveal that 15 wt% of the residue consists of sulfur and the rest contains carbon and oxygen (no fluorine is detected).

A probable explanation for the observed EW increase (IEC decrease) upon keeping the membranes in deionised water at RT for a period of time can be a slow reorganization of the microstructure that takes place in water at RT and leads to a partial inaccessibility of $-SO_3H$ groups for titration.

The thermal treatment is also observed to increase EW and decrease λ and ϕ values (Tables 3.2-3.5). The probable reasons for these observed changes are a condensation reaction and aging (sulphur formation) that take place in the membrane (explained above). The most pronounced changes in the membrane properties are found when the two processes are combined (time plus thermal treatments) (Tables 3.2-3.6). The slow reorganization process, which may take place at RT in water, might result in a favorable microstructure for a condensation reaction. Therefore, if the membranes are thermally treated, the extent

of the condensation reaction increases. Considering the analytical results obtained after time plus thermal treatments, the composite membranes show lower EWs (higher charge carrier concentrations) and higher water contents compared to the respective bare membranes. This result indicates that the probable reorganization process and condensation reaction or sulphur formation are suppressed to a certain extent in the presence of inorganic oxide particles.

It is indicated in Section 3.4.4 that thermal and hydrothermal treatments cause a decay of the proton conductivity and an increase of the activation enthalpy at a given λ (especially at low λ values). The proton conductivity decay can be attributed to two factors: (i) EW increase (charge carrier concentration decrease); (ii) mobility decrease (at low water contents). The lower proton conductivities of the heat-treated membranes compared to the ones of the as-received membranes at high water contents can be explained by the EW increase (charge carrier concentration decrease) upon heat treatment. However, at low water contents and low temperatures, the heat-treated membranes have much lower conductivities compared to the as-received membranes. At these conditions, the mobility of the charge carriers of the heat treated membranes is also observed to be suppressed (Figure 3.12 and 3.21). This can explain the lower conductivity values of the heat treated membranes at low water contents. The lower mobility of the heat-treated membranes at low water contents might be due to the change of microstructure of the membranes upon heat treatments. The higher activation enthalpies of the heat-treated membranes at a given water content (especially at low water contents) compared to the ones of the as-received membranes can be due to the less favorable microstructure for proton conduction.

The decay of the proton conductivity and the increase of the activation enthalpy due to the thermal and hydrothermal treatments are more pronounced for the Recast Nafion 1 compared to the respective composite membrane at a given λ (especially at low λ values) (Figure 3.13, 3.14). The heat-treated Composite 1 and Nafion® 117 have a similar, but the respective bare membrane has a lower proton conductivity and conductivity diffusion coefficient at a given water volume fraction (Figure 3.15, 3.16). A detailed investigation of the effect of hydrothermal treatments on the proton conductivity behavior shows an irreversible decay in conductivity (aging) which is less pronounced for the composite compared to the respective bare membrane (Figure 3.22). These results indicate that the

probable reorganization process or condensation reaction is more pronounced for the recast membrane without oxide particles.

As-received composite membranes have slightly higher conductivities at high water contents and clearly higher conductivities at low water contents compared to the as-received bare membranes (the temperature dependences of the proton conductivity of both of the as-received composite and recast membranes are comparable) (Figure 3.17 and 3.18). Since the membranes have comparable proton conductivities at a given water volume fraction (Figure 3.20), the higher proton conductivity of the composites at a given λ can be due to their slightly higher EWs.

At low temperatures and low water contents or upon thermal treatments, the dissociation of the sulfonic acid groups (which is directly related with the charge carrier concentration) decreases (see explanations of the ATR results above). Furthermore, local ordering increases (see Figure 3.26-3.28: with decreasing λ, the matrix peak of Nafion® 117 and Recast Nafion 1 become more distinct and shift to higher q values). In Figure 3.26 it is seen that both the heat-treated and humidified Nafion® 117 ($\lambda = 12$) and as-received and RT dried Nafion® 117 ($\lambda = 2$) show their matrix peak at the same position ($q \sim 0.05$ A^{-1}). As the heat-treated and humidified Nafion® 117 has a much higher water content ($\lambda = 12$) than the RT dried Nafion® 117 ($\lambda = 2$), the degree of local ordering between its crystallites is expected to be lower and therefore its matrix peak is expected to appear at lower q values. This indicates that the high temperature annealing increases the local ordering between crystallites to a higher extent compared to the room temperature drying procedure. High temperature annealing above T_g may lead to aggregation of the side chains and speed up the condensation reaction and/or aging (sulphur formation). This results in a decrease of hydrophilicity of the polymer and an increase of the EW and short range ordering. The possible change of microstructure upon heat treatment can be the reason for the decay in the transport properties at low water contents. In the case of the composite membrane, due to the presence of oxide particles, side chain aggregation might be restricted partially. This diminishes the extent of the condensation/aging reactions which are responsible for the microstructural changes. The thermally or hydrothermally treated composite membrane hardly displays a matrix peak (very low local ordering between its polymer crystallites). It

probably has a different microstructure compared to the respective recast Nafion and Nafion® 117 which is more likely "unaffected" by the treatments.

Compared to the respective recast Nafion and Nafion® 117, the composite membrane shows a steeper negative upturn in the scattered intensity at low q (Figure 3.27) which might result from the non-smooth interface between the inorganic phase and the organic matrix[188]. An enhanced small angle upturn would correspond to a shift of the long-range peak to greater q values which is probably due to the presence of highly correlated inorganic aggregates[189].

DMA results show that the incorporation of the oxide particles increases the glass transition temperature about 10 °C (3.30-3.33). This indicates that the composites have slightly higher thermal stability. If the measurements are performed at 15% RH, tan δ increases slower and goes through a maximum at higher temperatures (T_g increases). This shows that water probably strengthens the coulombic forces between sulfonic acid group clusters.

The storage moduli of the membranes decrease with increasing humidity and temperature. At low temperatures the effect of humidity on the storage modulus is quite remarkable. In this region, water acts as a softener and the stiffness of the membranes decreases. The storage moduli of the Composite 1 membrane decay more significantly with increasing water activity compared to the Recast Nafion 1 membrane (Figure 3.35). Due to the plasticizing effect of water, an increase in water uptake results in a decrease in elastic moduli. Therefore, the water content of the composite membrane is possibly higher compared to the bare membrane. Above a critical temperature (~ 80 °C), storage moduli keep decaying with temperature increase but start increasing with humidity increase (the temperature dependence of storage moduli is less pronounced at high humidities). At high temperatures (T > 80 °C), storage moduli measured at 30% RH are observed to be slightly higher than the ones measured at 15% RH (Figure 3.34-3.37). This means that water, which acts as a plasticizer at high humidities, acts as a stiffener at low humidities. It is assumed that water acts as a stabilizer by deprotonating the sulfonic acid groups and strengthening their ionic clusters via hydrogen bridge formation.

Composite 1, which contains the highest amount of oxide particles (10% w/w) among all composites, shows higher storage moduli compared to the respective recast membrane over the whole temperature and humidity range (Figure 3.35). However, the storage moduli of the other composites, which contain only 3% w/w oxide particles, exceed the values of the respective recast membranes only at high temperatures (T > 80 °C) and both humidities (30 and 15% RH) measured (Figure 3.36 and 3.37). This observation indicates that the mechanism, by which the admixture of oxide particles improves the storage moduli, differs at low and high temperatures. While at high temperatures, a comparatively low amount of oxide admixtures already shows a significant effect, at low temperatures the oxide concentration must exceed a critical value to result in any increase of the storage moduli at all. The reason for the composite membranes to have slightly higher storage moduli than the respective recast membranes at high temperatures (T > 80 °C) and low humidities (30 and 15% RH) is probably due to the ability of the composite membranes to keep higher amounts of water at high temperatures which has a positive effect on the membranes´ stiffness.

The line broadening of the bands (especially the SCF_2 band) in the dry state is probably due to the lower amount of water in the membranes compared to the wet state. The line broadening of the composite membrane compared to the ones of the respective recast Nafion and Nafion® 117 membranes (Figure 3.40 and 3.41) is less pronounced which indicates that the composite membranes keep higher amounts of water upon heat treatment.

3.6 Conclusion

In this part of the work, composite membranes, which are prepared by incorporation of small amounts of oxide particles (up to 10% w/w) into Nafion, bare recast Nafion and commercial Nafion® 117 are investigated in terms of proton conductivity, microstructure and mechanical properties. Several thermal and hydrothermal treatments are applied to the membranes in order to understand the reasons for the better fuel cell performance of the composite membranes at high temperature and low humidities (target fuel cell operation conditions).

According to the ATR-IR results, upon hydrothermal (high temperature and low humidity) treatments a condensation reaction and consequently an anhydride formation is suggested

to occur in the membranes. The thermal treatment above T_g may also lead to the same kind of products. In addition, sulphur formation (aging) is proposed to occur in such conditions. These reactions (condensation and sulphur formation) result in an increase of the EW (decrease of charge carrier concentration) and local ordering between polymer crystallites which are detected by acid-base titrimetry and SAXS measurements, respectively. The conductivity of the membranes is observed to decrease upon thermal and hydrothermal treatments. At high water contents, the decay of conductivity can be explained by the EW increase. However, at low water contents and low temperatures the conductivity decay is more (activation energy is higher) which can not be explained by the charge carrier concentration decrease. At these conditions, the mobility of the charge carriers is observed to be slightly suppressed which can explain the conductivity behavior. The lower mobility at low water contents can be due to the less favorable microstructure of the membranes for proton conduction. The proposed condensation reaction and/or sulphur formation (aging) lead to a decrease of hydrophilicity of the side chains. This negatively affects the nanophase separated morphology (hydration of ionic clusters decreases). The less amount of water in the membranes is shown to be unfavorable for the mechanical properties of the membranes at high temperatures as water acts as a stiffener in such conditions (DMA measurements).

The above explained effects of thermal and hydrothermal treatments on the membrane properties (EW, λ and ϕ), the proton conductivity, the activation enthalpy, the mobility and the microstructure of the membranes without oxide particles are more severe than they are for the composite membranes. A probable condensation reaction and/or aging and therefore changes in microstructure and transport properties of the material are suppressed in the presence of oxide particles. The composite membranes also keep higher amount of water at elevated conditions and they are mechanically slightly more stable compared to the respective bare membranes. Due to these reasons, composite membranes may show better performance at elevated fuel cell conditions (high temperature and low humidities).

4 Summary

In this work, the effects of incorporation of various types of oxide particles (e.g. ZrO_2, TiO_2, Al_2O_3) into proton conducting organic electrolytes is investigated. As a weak liquid model electrolyte, moderately proton conducting imidazole is chosen. As a highly proton conducting strong polymer electrolyte, and simultaneously practically very important electrolyte, a perfluorosulfonated ionomer (e.g. Nafion®) is selected for the second part of the work.

In the first part of this work, for the first time, the applicability of the concept of heterogeneous doping to a proton conducting weak liquid electrolyte is demonstrated. Imidazole is a protic, amphoteric solvent which forms hydrogen-bond networks similar to water. Apart from its transport coefficients which are similar to those of water, imidazole has the advantage of a much higher boiling point (257 °C) which makes it a good candidate to replace water as a proton carrier. Imidazole exhibits moderate proton conductivity due to low intrinsic charge carrier concentration. Therefore, a perceptible conductivity increase by heterogeneously doping imidazole is expected. Ac- impedance spectroscopy, pulsed-field gradient nuclear magnetic resonance (PFG-NMR) spectroscopy and zeta potential measurements were performed in order to investigate the composites.

Ac-impedance spectroscopy measurements of composites of imidazole with various types of nanometer sized oxide particles, which were performed as a function of temperature and oxide concentration show that the composites exhibit significantly enhanced ionic conductivities compared to the pure imidazole. The highest measured composite ionic conductivity is observed for the composite with heated $sZrO_2$, viz. $1.66 \times 10^{-2}\ \Omega^{-1}\ cm^{-1}$ at $\varphi = 0.25$ and 90 °C corresponding to an enhancement by a factor of ~10 compared to the pure ImiH at the same temperature. In comparison, the ImiH-TiO_2 composite conductivity is enhanced up to a factor of 4.2 (at $\varphi = 0.07$) and the ImiH-Al_2O_3 composite conductivity only up to a factor of 3.0 (at $\varphi = 0.03$) compared to the pure imidazole. The effective conductivities are observed to depend on the volume fraction of the added oxides as well as on the activity and density of the acidic sites on the surface of the oxides. As a typical percolation characteristic in such systems, conductivity increases with increasing oxide

volume fraction (φ), reaches a maximum (percolation threshold i.e. the volume fraction at which an attractive network is established through the composite) and then decreases with further increase in oxide concentration. The composites prepared with the oxides having the highest activity and density of the acidic sites on the surface show the most pronounced improvement in conductivity. PFG-NMR spectroscopy data are consistent with the measured conductivities. These results were quantitatively analyzed in light of the concept of heterogeneous doping that had been successfully used to quantitatively explain the ion conduction mechanism of weak solid electrolytes, salt containing polymer electrolytes and salt containing non-aqueous liquids. The proton conductivities calculated according to the heterogeneous doping concept are consistent with the experimentally observed conductivities. According to the concept, dispersion of fine oxide particles in the electrolyte leads to an interaction, which results in trapping of one ion species on the oxide surface. As a result, concentration of the compensating ions increases in the space charge region at the interface of oxide and conductor. The results of zeta potential measurements show that the surface charge of the inorganic oxides becomes strongly more negative on the addition of imidazole. This is consistent with the formation of a space-charge layer on the oxide surface as a consequence of an adsorptive interaction: trapping of imidazolate anions (Imi^-) on the oxide surface results in an increased concentration of imidazolium cations ($ImiH_2^+$) in the space charge region at the interface of oxide and conductor.

The second part of this work focuses on the investigation of the effects of inorganic oxide admixture on proton conductivity, microstructure and mechanical properties of a strong polymer electrolyte, namely Nafion®. Nafion® is strongly acidic and shows comparably high proton conductivity under fully hydrated conditions. Therefore, it has been commonly used as an electrolyte in polymer electrolyte membrane fuel cells (PEMFCs) and direct methanol fuel cells (DMFCs). However, at elevated temperatures Nafion® quickly looses its desirable ionic conductivity due to the membrane dehydration, thus limiting the fuel cell application to approximately T = 90 °C. Oxides have been widely used to improve the operation temperature of PEMFCs and DMFCs. Therefore, contrary to imidazole/oxide composites, Nafion®/oxide composites have already been recently investigated and many proposals have been made to explain the effects of oxides on the fuel cell performance. However, the proposed hypotheses are not fully supported by experimental observations. A

comprehensive study is necessary in order to have a better understanding of the improved fuel cell performance of the composites compared to the respective bare membranes at high temperature and low humidity fuel cell operation conditions. Therefore, in this work, various composite and respective bare membranes were investigated for which performance improvements had been proven in literature before. The commercial extruded Nafion® 117 was also analyzed for comparative purposes. Thermal and hydrothermal treatments were applied to the membranes in order to get an insight into the properties of the materials at target fuel cell operation conditions (high temperature and low humidity conditions). Various experimental techniques namely, ac-impedance spectroscopy, dynamic mechanical analysis (DMA), small-angle X-ray scattering (SAXS), solid state NMR and attenuated total reflection infrared (ATR-IR) spectroscopy were employed to characterize the samples.

According to the ATR-IR results, upon hydrothermal (high temperature and low humidity) treatments (e.g., 120 °C, 10% RH for 1 week) a condensation reaction and consequently an anhydride formation (R-O_2S-O-SO_2-R) is suggested to occur in the membranes. The thermal treatment above T_g (140 °C, 4h in a vacuum oven) may also lead to the same kind of products. In addition, sulphur formation (aging) is proposed to occur in such conditions which can be derived by X-ray powder diffractometry and energy dispersive microanalysis. These reactions (condensation and sulphur formation) result in an increase of the equivalent weight (decrease of charge carrier concentration) and local ordering between polymer crystallites (determined by the matrix peak) which were detected by acid-base titrimetry and SAXS measurements, respectively. The conductivity of the membranes is observed to decrease upon thermal and hydrothermal treatments. At high water contents, the decay of conductivity can be explained by the equivalent weight increase. However, at low water contents the conductivity decay is more pronounced (activation energy is much higher) which can not only be explained by the charge carrier concentration decrease. At these conditions, the mobility of the charge carriers is observed to be slightly suppressed which can explain the conductivity behavior. The lower mobility at low water contents can be due to the less favorable microstructure of the membranes for proton conduction. The proposed condensation reaction and/or sulphur formation (aging) lead to a decrease of hydrophilicity of the side chains. This negatively affects the nanophase separated

morphology since hydration of the ionic clusters decreases. Thereby, the water content in the membranes decreases. It is observed by DMA measurements that the lower amount of water in the membranes is unfavorable for the mechanical properties of the membranes at high temperatures as water acts as a stiffener in such conditions.

The above explained effects of thermal and hydrothermal treatments on the membrane properties (equivalent weight (EW), water content (λ) and water volume fraction (ϕ)), the proton conductivity, the activation enthalpy, the mobility and the microstructure of the membranes without oxide particles are more severe than they are for the composite membranes. According to the ac-impedance spectroscopy, acid-base titrimetry and SAXS measurements results a probable condensation reaction and/or aging and therefore changes in microstructure and transport properties of the material are suppressed in the presence of oxide particles. DMA measurements results show that the composite membranes also keep a higher amount of water at elevated conditions and they are thermally and mechanically slightly more stable compared to the respective bare membranes. The incorporation of the oxide particles also increases the glass transition temperature about 10 °C which indicates that the composites have slightly higher thermal stability. These results indicate that the incorporation of oxide particles improve the stability of the bare Nafion® membranes which may explain the better fuel cell performance of the composites at high temperatures and low humidities.

In conclusion, in this work it is shown that the oxide incorporation has a positive effect on both weak and strong proton conducting electrolytes: while in the former the proton conductivity is improved by charge carrier concentration increase in the space charge layer, in the latter one it is the structural, thermal and mechanical stability of the material that is beneficially affected at elevated conditions. This study may encourage further developments of electrolyte materials for alternative energy conversion devices.

5 References

[1] J. Maier, *Journal Of The Electrochemical Society* **1987**, *134*, 1524.

[2] M. Faraday, *Experimental Researches in Electricity* **1833**, 119.

[3] W. Jander, *Zeitschrift für Angewandte Chemie* **1929**, *42*, 462.

[4] C. C. Liang, *Journal Of The Electrochemical Society* **1973**, *120*, 1289.

[5] T. Jow, J. B. Wagner, *Journal Of The Electrochemical Society* **1979**, *126*, 1963.

[6] J. Maier, *Solid State Ionics* **1986**, *18-9*, 1141.

[7] K. Shahi, J. B. Wagner, *Journal Of The Electrochemical Society* **1981**, *128*, 6.

[8] J. Maier, *Materials Research Bulletin* **1985**, *20*, 383.

[9] C. Wagner, *Journal Of Physics And Chemistry Of Solids* **1972**, *33*, 1051.

[10] J. Maier, *Journal Of Physics And Chemistry Of Solids* **1985**, *46*, 309.

[11] J. Maier, *Berichte Der Bunsen-Gesellschaft-Physical Chemistry Chemical Physics* **1985**, *89*, 355.

[12] J. Maier, *Berichte Der Bunsen-Gesellschaft-Physical Chemistry Chemical Physics* **1989**, *93*, 1468.

[13] J. Maier, *Berichte Der Bunsen-Gesellschaft-Physical Chemistry Chemical Physics* **1989**, *93*, 1474.

[14] J. Maier, *Progress In Solid State Chemistry* **1995**, *23*, 171.

[15] J. Maier, *Physica Status Solidi B-Basic Research* **1984**, *123*, K89.

[16] J. Maier, *Journal Of The Electrochemical Society* **1985**, *132*, C364.

[17] J. Maier, *Berichte Der Bunsen-Gesellschaft-Physical Chemistry Chemical Physics* **1984**, *88*, 1057.

[18] J. Maier, *Physical Chemistry of Ionic Materials*, John Wiley & Sons, Ltd, **2005**.

[19] F. Croce, G. B. Appetecchi, L. Persi, B. Scrosati, *Nature* **1998**, *394*, 456.

[20] F. Croce, R. Curini, A. Martinelli, L. Persi, F. Ronci, B. Scrosati, R. Caminiti, *Journal Of Physical Chemistry B* **1999**, *103*, 10632.

[21] F. Croce, L. Settimi, B. Scrosati, *Electrochemistry Communications* **2006**, *8*, 364.

[22] B. Kumar, S. J. Rodrigues, L. G. Scanlon, *Journal Of The Electrochemical Society* **2001**, *148*, A1191.

[23] W. Wieczorek, Z. Florjanczyk, J. R. Stevens, *Electrochimica Acta* **1995**, *40*, 2251.

[24] J. Y. Xi, X. P. Qiu, S. X. Zheng, X. Z. Tang, *Polymer* **2005**, *46*, 5702.

[25] D. E. Fenton, J. M. Parker, P. V. Wright, *Polymer* **1973**, *14*, 589.

[26] J. E. Weston, B. C. H. Steele, *Solid State Ionics* **1982**, *7*, 75.

[27] B. Kumar, S. J. Rodrigues, *Journal Of The Electrochemical Society* **2001**, *148*, A1336.

[28] J. Przyluski, M. Siekierski, W. Wieczorek, *Electrochimica Acta* **1995**, *40*, 2101.

[29] J. H. Shin, S. Passerini, *Journal Of The Electrochemical Society* **2004**, *151*, A238.

[30] J. Adebahr, A. S. Best, N. Byrne, P. Jacobsson, D. R. MacFarlane, M. Forsyth, *Physical Chemistry Chemical Physics* **2003**, *5*, 720.

[31] G. B. Appetecchi, F. Croce, L. Persi, F. Ronci, B. Scrosati, *Electrochimica Acta* **2000**, *45*, 1481.

[32] A. S. Arico, P. Bruce, B. Scrosati, J. M. Tarascon, W. Van Schalkwijk, *Nature Materials* **2005**, *4*, 366.

[33] F. Croce, B. Scrosati, *Advanced Membrane Technology* **2003**, *984*, 194.

[34] W. Wieczorek, A. Zalewska, D. Raducha, Z. Florjanczyk, J. R. Stevens, *Journal Of Physical Chemistry B* **1998**, *102*, 352.

[35] A. J. Bhattacharyya, J. Maier, *Advanced Materials* **2004**, *16*, 811.

[36] A. J. Bhattacharyya, J. Maier, R. Bock, F. F. Lange, *Solid State Ionics* **2006**, *177*, 2565.

[37] A. J. Bhattacharyya, M. Dolle, J. Maier, *Electrochemical And Solid State Letters* **2004**, *7*, A432.

[38] A. Chandra, J. Maier, *Solid State Ionics* **2002**, *148*, 153.

[39] R. Srivastava, S. Chandra, *Progress In Crystal Growth And Characterization Of Materials* **2002**, *44*, 133.

[40] K. T. Adjemian, R. Dominey, L. Krishnan, H. Ota, P. Majsztrik, T. Zhang, J. Mann, B. Kirby, L. Gatto, M. Velo-Simpson, J. Leahy, S. Srinivasant, J. B. Benziger, A. B. Bocarsly, *Chemistry Of Materials* **2006**, *18*, 2238.

[41] K. T. Adjemian, S. J. Lee, S. Srinivasan, J. Benziger, A. B. Bocarsly, *Journal Of The Electrochemical Society* **2002**, *149*, A256.

[42] P. L. Antonucci, A. S. Arico, P. Creti, E. Ramunni, V. Antonucci, *Solid State Ionics* **1999**, *125*, 431.

[43] A. S. Arico, V. Baglio, A. Di Blasi, P. Creti, P. L. Antonucci, V. Antonucci, *Solid State Ionics* **2003**, *161*, 251.

[44] V. Baglio, A. S. Arico, A. Di Blasi, V. Antonucci, P. L. Antonucci, S. Licoccia, E. Traversa, F. S. Fiory, *Electrochimica Acta* **2005**, *50*, 1241.

[45] V. Baglio, A. Di Blasi, A. S. Arico, V. Antonucci, P. L. Antonucci, C. Trakanprapai, V. Esposito, S. Licoccia, E. Traversa, *Journal Of The Electrochemical Society* **2005**, *152*, A1373.

[46] B. Baradie, J. P. Dodelet, D. Guay, *Journal Of Electroanalytical Chemistry* **2000**, *489*, 101.

[47] E. Chalkova, M. V. Fedkin, D. J. Wesolowski, S. N. Lvov, *Journal Of The Electrochemical Society* **2005**, *152*, A1742.

[48] E. Chalkova, M. B. Pague, M. V. Fedkin, D. J. Wesolowski, S. N. Lvov, *Journal Of The Electrochemical Society* **2005**, *152*, A1035.

[49] Q. Deng, R. B. Moore, K. A. Mauritz, *Journal Of Applied Polymer Science* **1998**, *68*, 747.

[50] V. Di Noto, R. Gliubizzi, E. Negro, G. Pace, *Journal Of Physical Chemistry B* **2006**, *110*, 24972.

[51] V. Di Noto, R. Gliubizzi, E. Negro, M. Vittadello, G. Pace, *Electrochimica Acta* **2007**, *53*, 1618.

[52] N. H. Jalani, K. Dunn, R. Datta, *Electrochimica Acta* **2005**, *51*, 553.

[53] D. H. Jung, S. Y. Cho, D. H. Peck, D. R. Shin, J. S. Kim, *Journal Of Power Sources* **2002**, *106*, 173.

[54] M. A. Navarra, F. Croce, B. Scrosati, *Journal Of Materials Chemistry* **2007**, *17*, 3210.

[55] S. P. Nunes, B. Ruffmann, E. Rikowski, S. Vetter, K. Richau, *Journal Of Membrane Science* **2002**, *203*, PII S0376.

[56] A. Sacca, A. Carbone, E. Passalacqua, A. D'Epifanio, S. Licoccia, E. Traversa, E. Sala, F. Traini, R. Ornelas, *Journal Of Power Sources* **2005**, *152*, 16.

[57] A. Sacca, I. Gatto, A. Carbone, R. Pedicini, E. Passalacqua, *Journal Of Power Sources* **2006**, *163*, 47.

[58] Q. F. Li, R. H. He, J. O. Jensen, N. J. Bjerrum, *Chemistry Of Materials* **2003**, *15*, 4896.

[59] K. A. Mauritz, R. B. Moore, *Chemical Reviews* **2004**, *104*, 4535.

[60] T. S. Zhao, K. D. Kreuer, T. V. Nguyen, *Advances in Fuel Cells, Vol. 1*, Elsevier, Oxford, UK, **2007**.

[61] A. V. Anantaraman, C. L. Gardner, *Journal Of Electroanalytical Chemistry* **1996**, *414*, 115.

[62] Y. Sone, P. Ekdunge, D. Simonsson, *Journal Of The Electrochemical Society* **1996**, *143*, 1254.

[63] T. A. Zawodzinski, C. Derouin, S. Radzinski, R. J. Sherman, V. T. Smith, T. E. Springer, S. Gottesfeld, *Journal Of The Electrochemical Society* **1993**, *140*, 1041.

[64] K. T. Adjemian, S. Srinivasan, J. Benziger, A. B. Bocarsly, *Journal Of Power Sources* **2002**, *109*, 356.

[65] K. D. Kreuer, A. Fuchs, M. Ise, M. Spaeth, J. Maier, *Electrochimica Acta* **1998**, *43*, 1281.

[66] M. Schuster, W. H. Meyer, G. Wegner, H. G. Herz, M. Ise, M. Schuster, K. D. Kreuer, J. Maier, *Solid State Ionics* **2001**, *145*, 85.

[67] M. R. Grimmett, K. T. Potts, *Comprehensive Heterocyclic Chemistry, Vol. 5*, Pergamon Press, **1984**.

[68] R. J. Sundberg, R. B. Martin, *Chemical Reviews* **1974**, *74*, 471.

[69] J. Catalan, J. L. M. Abboud, J. Elguero, *Advances In Heterocyclic Chemistry* **1987**, *41*, 187.

[70] K. D. Kreuer, *Solid State Ionics: Science&Technology*, World Scientific Publishing Co., Singapore, **1998**.

[71] W. Munch, K. D. Kreuer, W. Silvestri, J. Maier, G. Seifert, *Solid State Ionics* **2001**, *145*, 437.

[72] N. Agmon, *Chemical Physics Letters* **1995**, *244*, 456.

[73] M. Tuckerman, K. Laasonen, M. Sprik, M. Parrinello, *Journal Of Chemical Physics* **1995**, *103*, 150.

[74] K. D. Kreuer, *Solid State Ionics* **2000**, *136*, 149.

[75] M. F. H. Schuster, W. H. Meyer, M. Schuster, K. D. Kreuer, *Chemistry Of Materials* **2004**, *16*, 329.

[76] G. R. Goward, M. F. H. Schuster, D. Sebastiani, I. Schnell, H. W. Spiess, *Journal Of Physical Chemistry B* **2002**, *106*, 9322.

[77] K. D. Kreuer, *Journal Of Membrane Science* **2001**, *185*, 29.

[78] M. F. H. Schuster, W. H. Meyer, *Annual review of materials research, Volume 33* **2003**, 233.

[79] K. D. Kreuer, *Solid State Ionics* **1997**, *97*, 1.

[80] B. C. H. Steele, A. Heinzel, *Nature* **2001**, *414*, 345.

[81] C. Yang, P. Costamagna, S. Srinivasan, J. Benziger, A. B. Bocarsly, *Journal Of Power Sources* **2001**, *103*, 1.

[82] S. Beyazyildirim, K. D. Kreuer, M. Schuster, A. J. Bhattacharyya, J. Maier, *Advanced Materials* **2008**, *20*, 1274.

[83] A. J. Bhattacharyya, J. Fleig, Y. G. Guo, J. Maier, *Advanced Materials* **2005**, *17*, 2630.

[84] J. Maier, *International Journal Of Materials Research* **2008**, *99*, 24.

[85] H. Yamada, A. J. Bhattacharyya, J. Maier, *Advanced Functional Materials* **2006**, *16*, 525.

[86] J. E. Bauerle, *Journal of Physical Chemical Solids* **1969**, *30*, 2657.

[87] W. S. Price, *Concepts In Magnetic Resonance* **1997**, *9*, 299.

[88] A. D. S. Telfah, Stuttgart University (Stuttgart), **2008**.

[89] Y. G. Guo, Y. S. Hu, J. Maier, *Chemical Communications* **2006**, 2783.

[90] T. Cosgrove, *Colloid Science Principles, Methods and Applications*, Blackwell Publishing, **2005**.

[91] R. J. Hunter, *Foundations of Colloid Science*, 2nd ed., Oxford University Press, New York, **2001**.

[92] R. H. Müller, *Zeta Potential und Partikelladung in der Laborpraxis*, Wissenschaftliche Verlagsgesellschaft mbH, Stuttgart, **1996**.

[93] T. Dippel, K. D. Kreuer, M. Hampele, A. Rabenau, M. Mehring, J. U. Schütz, H. C. Wolf, *25th Congress Ampére*, Springer, Berlin, **1990**.

[94] I. H. Joe, A. K. Vasudevan, G. Aruldhas, A. D. Damodaran, K. G. K. Warrier, *Journal Of Solid State Chemistry* **1997**, *131*, 181.

[95] X. B. Li, K. Nagaoka, R. Olindo, J. A. Lercher, *Journal Of Catalysis* **2006**, *238*, 39.

[96] T. Jin, T. Yamaguchi, K. Tanabe, *Journal Of Physical Chemistry* **1986**, *90*, 4794.

[97] H. K. Mishra, K. M. Parida, *Applied Catalysis A-General* **2002**, *224*, 179.

[98] K. Nakamoto, J. Fujita, S. Tanaka, M. Kobayashi, *Journal Of The American Chemical Society* **1957**, *79*, 4904.

[99] D. Spielbauer, G. A. H. Mekhemer, M. I. Zaki, H. Knozinger, *Catalysis Letters* **1996**, *40*, 71.

[100] H. Maekawa, R. Tanaka, T. Sato, Y. Fujimaki, T. Yamamura, *Solid State Ionics* **2004**, *175*, 281.

[101] H. Yamada, T. Yamato, I. Moriguchi, T. Kudo, *Solid State Ionics* **2004**, *175*, 195.

[102] K. D. Kreuer, S. J. Paddison, E. Spohr, M. Schuster, *Chemical Reviews* **2004**, *104*, 4637.

[103] W. R. Grove, *Philosophical Magazine and Journal of Science* **1839**, *14*, 127.

[104] A. E. Steck, *Proceedings Of The First International Symposium On New Materials For Fuel Cell Systems* **1995**, 74.

[105] J. St-Pierre, N. Y. Jia, *Journal Of New Materials For Electrochemical Systems* **2002**, *5*, 263.

[106] J. R. Yu, T. Matsuura, Y. Yoshikawa, M. N. Islam, M. Hori, *Physical Chemistry Chemical Physics* **2005**, *7*, 373.

[107] F. N. Buchi, S. Srinivasan, *Journal Of The Electrochemical Society* **1997**, *144*, 2767.

[108] E. Endoh, S. Terazono, H. Widjaja, Y. Takimoto, *Electrochemical And Solid State Letters* **2004**, *7*, A209.

[109] S. D. Knights, K. M. Colbow, J. St-Pierre, D. P. Wilkinson, *Journal Of Power Sources* **2004**, *127*, 127.

[110] A. Bosnjakovic, S. Schlick, *Journal Of Physical Chemistry B* **2004**, *108*, 4332.

[111] C. Chen, G. Levitin, D. W. Hess, T. F. Fuller, *Journal Of Power Sources* **2007**, *169*, 288.

[112] S. Kundu, L. C. Simon, M. W. Fowler, *Polymer Degradation And Stability* **2008**, *93*, 214.

[113] A. Panchenko, H. Dilger, E. Moller, T. Sixt, E. Roduner, *Journal Of Power Sources* **2004**, *127*, 325.

[114] L. Ghassemadeh, M. Marrony, R. Barrera, K. D. Kreuer, J. Maier, K. Muller, *Journal Of Power Sources* **2009**, *186*, 334.

[115] F. Bauer, S. Denneler, M. Willert-Porada, *Journal Of Polymer Science Part B-Polymer Physics* **2005**, *43*, 786.

[116] H. L. Yeager, A. Steck, *Analytical Chemistry* **1979**, *51*, 862.

[117] T. A. Zawodzinski, T. E. Springer, J. Davey, R. Jestel, C. Lopez, J. Valerio, S. Gottesfeld, *Journal Of The Electrochemical Society* **1993**, *140*, 1981.

[118] P. Schroeder, *Zeitschrift für Physikalische Chemie* **1903**, *45*, 75.

[119] V. Freger, *Journal Of Physical Chemistry B* **2009**, *113*, 24.

[120] L. M. Onishi, J. M. Prausnitz, J. Newman, *Journal Of Physical Chemistry B* **2007**, *111*, 10166.

[121] M. Bass, V. Freger, *Desalination* **2006**, *199*, 277.

[122] P. H. Choi, R. Datta, *Journal Of The Electrochemical Society* **2003**, *150*, E601.

[123] K. D. Kreuer, *Chemistry Of Materials* **1996**, *8*, 610.

[124] G. Alberti, M. Casciola, L. Massinelli, B. Bauer, *Journal Of Membrane Science* **2001**, *185*, 73.

[125] M. Casciola, G. Alberti, M. Sganappa, R. Narducci, *Journal Of Power Sources* **2006**, *162*, 141.

[126] T. D. Gierke, G. E. Munn, F. C. Wilson, *Journal Of Polymer Science Part B-Polymer Physics* **1981**, *19*, 1687.

[127] A. E. Steck, *New Materials for Fuel Cell Systems I. Proceedings of the First International Symposium on New Materials for Fuel Cell Systems|New Materials for Fuel Cell Systems I. Proceedings of the First International Symposium on New Materials for Fuel Cell Systems* **1995**, 74.

[128] H. L. Yeager, A. Eisenberg, *Acs Symposium Series* **1982**, *180*, 1.

[129] S. C. Yeo, A. Eisenberg, *Journal Of Applied Polymer Science* **1977**, *21*, 875.

[130] M. Fujimura, T. Hashimoto, H. Kawai, *Macromolecules* **1982**, *15*, 136.

[131] L. Rubatat, A. L. Rollet, G. Gebel, O. Diat, *Macromolecules* **2002**, *35*, 4050.

[132] H. G. Haubold, T. Vad, H. Jungbluth, P. Hiller, *Electrochimica Acta* **2001**, *46*, 1559.

[133] K. Schmidt-Rohr, Q. Chen, *Nature Materials* **2008**, *7*, 75.

[134] B. N. Grgur, G. Zhuang, N. M. Markovic, P. N. Ross, *Journal Of Physical Chemistry B* **1997**, *101*, 3910.

[135] K. Y. Chen, P. K. Shen, A. C. C. Tseung, *Journal Of The Electrochemical Society* **1995**, *142*, L185.

[136] H. A. Gasteiger, N. M. Markovic, P. N. Ross, *Journal Of Physical Chemistry* **1995**, *99*, 8290.

[137] H. A. Gasteiger, N. Markovic, P. N. Ross, E. J. Cairns, *Journal Of Physical Chemistry* **1994**, *98*, 617.

[138] G. Ye, C. A. Hayden, G. R. Goward, *Macromolecules* **2007**, *40*, 1529.

[139] F. Bauer, M. Willert-Porada, *Fuel Cells* **2006**, *6*, 261.

[140] M. Willert-Porada, F. Bauer, *Solid State Ionics, Diffusion & Reactions* **2006**, *vol.177, no.26-32*, 2391.

[141] C. Yang, S. Srinivasan, A. S. Arico, P. Creti, V. Baglio, V. Antonucci, *Electrochemical And Solid State Letters* **2001**, *4*, A31.

[142] B. Tazi, O. Savadogo, *Electrochimica Acta* **2000**, *45*, 4329.

[143] Z. G. Shao, H. F. Xu, M. Q. Li, I. M. Hsing, *Solid State Ionics* **2006**, *177*, 779.

[144] S. K. Young, K. A. Mauritz, *Journal Of Polymer Science Part B-Polymer Physics* **2002**, *40*, 2237.

[145] S. K. Young, W. L. Jarrett, K. A. Mauritz, *Polymer* **2002**, *43*, 2311.

[146] J. H. Chen, M. Asano, Y. Maekawa, M. Yoshida, *Journal Of Membrane Science* **2006**, *277*, 249.

[147] J. Ennari, S. Hietala, M. Paronen, F. Sundholm, N. Walsby, M. Karjalainen, R. Serimaa, T. Lehtinen, G. Sundholm, *Macromolecular Symposia* **1999**, *146*, 41.

[148] F. N. Buchi, B. Gupta, O. Haas, G. G. Scherer, *Journal Of The Electrochemical Society* **1995**, *142*, 3044.

[149] B. Bonnet, D. J. Jones, J. Roziere, L. Tchicaya, G. Alberti, M. Casciola, L. Massinelli, B. Bauer, A. Peraio, E. Ramunni, *Journal Of New Materials For Electrochemical Systems* **2000**, *3*, 87.

[150] N. N. Fathima, R. Aravindhan, D. Lawrence, U. Yugandhar, T. S. R. Moorthy, B. U. Nair, *Journal Of Scientific & Industrial Research* **2007**, *66*, 209.

[151] C. Arnold, R. A. Assink, *Journal Of The Electrochemical Society* **1986**, *133*, C123.

[152] C. Brousse, R. Chapurlat, J. P. Quentin, *Desalination* **1976**, *18*, 137.

[153] C. Genies, R. Mercier, B. Sillion, N. Cornet, G. Gebel, M. Pineri, *Polymer* **2001**, *42*, 359.

[154] N. Cornet, O. Diat, G. Gebel, F. Jousse, D. Marsacq, R. Mercier, M. Pineri, *Journal Of New Materials For Electrochemical Systems* **2000**, *3*, 33.

[155] J. Mader, L. Xiao, T. J. Schmidt, B. C. Benicewicz, *Fuel Cells Ii* **2008**, *216*, 63.

[156] J. T. Wang, R. F. Savinell, J. Wainright, M. Litt, H. Yu, *Electrochimica Acta* **1996**, *41*, 193.

[157] G. K. R. Senadeera, M. A. Careem, S. Skaarup, K. West, *Solid State Ionics* **1996**, *85*, 37.

[158] G. Zukowska, M. Rogowska, E. Weczkowska, W. Wieczorek, *Solid State Ionics* **1999**, *119*, 289.

[159] J. Kerres, A. Ullrich, F. Meier, T. Haring, *Solid State Ionics* **1999**, *125*, 243.

[160] C. Hasiotis, L. Qingfend, V. Deimede, J. K. Kallitsis, C. G. Kontoyannis, N. J. Bjerrum, *Journal Of The Electrochemical Society* **2001**, *148*, A513.

[161] K. A. Mauritz, I. D. Stefanithis, S. V. Davis, R. W. Scheetz, R. K. Pope, G. L. Wilkes, H. H. Huang, *Journal Of Applied Polymer Science* **1995**, *55*, 181.

[162] M. B. Satterfield, P. W. Majsztrik, H. Ota, J. B. Benziger, A. B. Bocarsly, *Journal Of Polymer Science Part B-Polymer Physics* **2006**, *44*, 2327.

[163] O. Glatter, O. Kratky, *Small- Angle X-Ray Scattering*, Academic Press., London, **1982**.

[164] R. J. Roe, *Methods of X-ray and Neutron Scattering in Polymer Science*, Oxford University Press, Oxford, **1999**.

[165] M. J. Duer, *Solid State NMR Spectroscopy: Principles and Applications*, Blackwell Publishing, **2002**.

[166] A. S. Arico, P. Creti, P. L. Antonucci, V. Antonucci, *Electrochemical And Solid State Letters* **1998**, *1*, 66.

[167] D. R. Morris, X. D. Sun, *Journal Of Applied Polymer Science* **1993**, *50*, 1445.

[168] T. A. Zawodzinski, M. Neeman, L. O. Sillerud, S. Gottesfeld, *Journal Of Physical Chemistry* **1991**, *95*, 6040.

[169] P. Choi, N. H. Jalani, T. M. Thampan, R. Datta, *Journal Of Polymer Science Part B-Polymer Physics* **2006**, *44*, 2183.

[170] K. D. Kreuer, M. Schuster, B. Obliers, O. Diat, U. Traub, A. Fuchs, U. Klock, S. J. Paddison, J. Maier, *Journal Of Power Sources* **2008**, *178*, 499.

[171] Z. X. Liang, W. M. Chen, J. G. Liu, S. L. Wang, Z. H. Zhou, W. Z. Li, G. Q. Sun, Q. Xin, *Journal Of Membrane Science* **2004**, *233*, 39.

[172] D. Chu, D. Gervasio, M. Razaq, E. B. Yeager, *Journal Of Applied Electrochemistry* **1990**, *20*, 157.

[173] R. Basnayake, G. R. Peterson, D. J. Casadonte, C. Korzeniewski, *Journal Of Physical Chemistry B* **2006**, *110*, 23938.

[174] L. Grosmaire, S. Castagnoni, P. Huguet, P. Sistat, M. Boucher, P. Bouchard, P. Bebin, S. Deabate, *Physical Chemistry Chemical Physics* **2008**, *10*, 1577.

[175] G. Gebel, O. Diat, *Fuel Cells* **2005**, *5*, 261.

[176] R. B. Moore, C. R. Martin, *Macromolecules* **1988**, *21*, 1334.

[177] M. Fujimura, T. Hashimoto, H. Kawai, *Macromolecules* **1981**, *14*, 1309.

[178] G. Gebel, P. Aldebert, M. Pineri, *Macromolecules* **1987**, *20*, 1425.

[179] K. Lee, A. Ishihara, S. Mitsushima, N. Kamiya, K. Ota, *Journal Of The Electrochemical Society* **2004**, *151*, A639.

[180] S. K. Young, K. A. Mauritz, *Journal Of Polymer Science Part B-Polymer Physics* **2001**, *39*, 1282.

[181] Q. Chen, K. Schmidt-Rohr, *Macromolecules* **2004**, *37*, 5995.

[182] T. Gramstad, R. N. Haszeldine, *Journal Of The Chemical Society* **1957**, 4069.

[183] K. V. Stopperka, *Zeitschrift für anorganische und allgemeine Chemie* **1966**, *345*, 264.

[184] W. M. Grava, T. Okada, Y. Kawano, *Electrochemistry* **2006**, *74*, 467.

[185] J. L. Qiao, M. Saito, K. Hayamizu, T. Okada, *Journal Of The Electrochemical Society* **2006**, *153*, A967.

[186] B. Vogel, E. Aleksandrova, S. Mitov, M. Krafft, A. Dreizler, J. Kerres, M. Hein, E. Roduner, *Journal Of The Electrochemical Society* **2008**, *155*, B570.

[187] F. M. Collette, C. Lorentz, G. G., T. F., *to be published* **2009**.

[188] B. P. Ladewig, R. B. Knott, A. J. Hill, J. D. Riches, J. W. White, D. J. Martin, J. C. D. da Costa, G. Q. Lu, *Chemistry Of Materials* **2007**, *19*, 2372.

[189] R. B. Moore, M. Gauthier, C. E. Williams, A. Eisenberg, *Macromolecules* **1992**, *25*, 5769.

Appendix

List of Figures

List of tables

Acknowledgements

I would like to express my sincerest thanks to the following people without whom this thesis would not be accomplished:

I would like to thank Prof. Dr. Joachim Maier for giving me the opportunity to work in his group at the Max Planck Institute for Solid State Research and benefit from the excellent research conditions.

I am grateful to Prof. Dr. Emil Roduner and Prof. Dr. Ir. Eric Jan Mittemeijer for being on my examination committee.

I thank Priv. Doz. Dr. Klaus Dieter Kreuer for being my advisor and giving me the opportunity to work independently.

I had neither starved nor been homeless during my PhD study. I am very grateful for that. I would like to thank the International Max Planck Research School for Advanced Materials (IMPRS-AM) for financial support and Dr. Hans-Georg Libuda for being helpful whenever I need.

I thank Dr. A. Saccá and Dr. A. S. Aricó for providing Nafion/oxide membranes. Many thanks to Annette Fuchs and Udo Klock for their kind help besides technical support, Gabi Götz for recording X-ray diffractograms, Lida Ghassemzadeh for solid state NMR measurements, Michael Schuster for PFG-NMR measurements and Giuseppe Portale for SAXS measurements. I also thank Sofia Weiglein for her help in administrative work.

I thank my officemate Dr. Giuliano Gregori for his help besides his kind friendship. I further thank all of my colleagues in the group of Prof. Maier whose accompany made my days in FKF more enjoyable and memorable. Especially thank to Olga Delmer, Anna Jarosik, Lei Wang, Carla Cavalca de Araujo, Katja Weichert, Mona Shirpour and Lida Ghassemzadeh. The "*Junggesellen-Abschied Party*" was unforgettable! I wish you all the best for the future and hope that our roads will cross again.

Also many thanks to the members of "Turkish Mafia", for their friendship. The dinners, barbeque parties and small meetings that we had between stressful working periods helped

me to re-gain my energy. I am especially grateful to Güliz and Hasan Çakmak for helping me to come to Stuttgart and for their genuine friendship.

I would like to thank my parents for allowing me to go and walk in my own way, for their endless support throughout my education, for their love, trust and prays. I would also like to thank my brothers, sisters and their families for their support, love and everything they have done for me. *Canim ailem, eğitimim boyunca bana güvenip destek verdiğiniz, sevginiz ve dualarınızla her zaman yanımda olduğunuz için sonsuz teşekkürler.*

I also want to thank my parents-in-law for their support. The things that you have done for me in this hard period of my life will always be appreciated. *Ich möchte auch meinen Schwiegereltern herzlich für ihre Unterstützung danken. Ich schätze es sehr, was Ihr in dieser schwierigen Zeit für mich getan habt.*

My special *thank you* goes to my beloved husband for his endless support, encouragement, trust and love. Thank you for always being there for me.